

QUANTITATIVE NEAR-FIELD MICROWAVE
HOLOGRAPHY

QUANTITATIVE NEAR-FIELD MICROWAVE HOLOGRAPHY

By:

JEFFREY R. THOMPSON, B. ENG.

A Thesis

Submitted to the School of Graduate Studies

in Partial Fulfillment of the Requirements

of the Degree

Masters of Applied Science

McMaster University

© Jeffrey R. Thompson, August 2015

MASTERS OF APPLIED SCIENCE (2015)
(Electrical and Computer Engineering)

McMASTER UNIVERSITY
Hamilton, Ontario

TITLE: Quantitative Near-Field Holography

AUTHOR: Jeffrey R. Thompson

B.Eng.

Department of Electrical and Computer Engineering

(Dalhousie University, Halifax, Nova Scotia)

SUPERVISOR: N.K. Nikolova, Professor

Ph.D. (University of Electro-Communications)

P.Eng. (Ontario)

Canada Research Chair (in High Frequency
Electromagnetics)

Fellow of the Institute of Electrical and Electronic Engineers

Fellow of the Canadian Academy of Engineering

NUMBER OF PAGES: XCVI, 96

ABSTRACT

This thesis presents two quantitative holographic reconstruction techniques for the imaging of dielectric targets. The first method is a quasi-real-time holographic reconstruction technique, which is capable of imposing physically based constraints on the real and imaginary parts of the permittivity. The other method is a real-time holographic reconstruction technique that is faster than the constrained method but cannot accommodate constraints on the reconstructed permittivity in its current form. The goal of this thesis is to introduce both methods and recommend which is best.

Microwave holography has been used by our research group to reconstruct images of a target's shape and location from microwave scattering parameters. This thesis will demonstrate that holography can be extended to quantify the permittivity distribution in a region of interest.

The problems presented in this thesis are generic and are meant to show that near-field quantitative holography is a valid approach for applications such as tissue imaging, baggage inspection, concealed weapon detection, *etc.*

The holographic inversion is carried out in the spectral domain (Fourier space), which allows for the use of Fourier transform properties to expedite the algorithm. This differs from sensitivity-based imaging (another inversion method developed by Tu *et al.* (2015)) where the inversion is performed in real space and is unable to take advantage of the techniques proposed in this thesis to improve the speed of reconstruction.

Mutual coupling is not taken into consideration in the forward model of scattering used here; however, this technique is meant to be viewed as a foundation for a more sophisticated reconstruction algorithm, like the iterative Born method, which can overcome such limitations. Iterative reconstruction methods require an accurate initial guess, which can be provided by the quantitative technique presented in this thesis.

Moreover, this technique, implementing fast and efficient linearized inversion, can serve as a module, which is called repetitively by the iterative algorithm. Such a module will take the current estimate of the total field distribution inside the imaged volume as an input and will return an estimate of complex permittivity distribution.

ACKNOWLEDGEMENTS

I would like to begin by saying that I am grateful to have had the expertise and support of Dr. Natalia K. Nikolova throughout my studies. She has been a great model for how a good engineer approaches problems. It has been an honour being her student.

I would also like to take this opportunity to thank the people who have been such a great help here at McMaster University. I would like to first thank Justin McCombe whose guidance was invaluable both with the simulation and algorithm development of the initial work on quantitative imaging. Without that help, this thesis would not have come to reality.

I would also like to express my gratitude to Sheng Tu. His insight and expert mathematical skills helped during the algorithm development stage.

I would also like to thank the members of the research group, Alex Beaverstone, Denys Shumakov and Daniel Tajik who helped me with my studies and my research. I wish them luck in developing microwave holography into a realizable technique.

Finally, I would like to thank my family both here in Ontario and in Nova Scotia for their support. Without them, I would not have made it through this.

Table of Contents

ABSTRACT.....	iv
ACKNOWLEDGEMENTS	vi
Table of Contents	vii
List of Figures	x
List of Tables	xiv
List of Abbreviations	xv
Chapter 1 Introduction	1
1.1 Background	1
1.2 Motivation	2
1.3 Contributions.....	5
1.4 Outline of the Thesis	5
References	7
Chapter 2 Background on Microwave Holography	10
2.1 Introduction	10
2.2 Planar Raster Scanning Acquisition Setup.....	11
2.3 Forward Model in Terms of Scattered Electric Fields	12
2.4 Prior Developments in Qualitative Holography.....	14
2.4.1 The Scalar Model of Holography	14
2.4.2 Depth and Lateral Resolution	15
2.4.3 Spatial and Frequency Sampling for 2D and 3D Holography	17
2.4.4 Estimates of Green's Function.....	18
2.4.5 Solving the Least-Square Holography Problems in 2D	20
2.4.6 Building the Least-Square Problem in 3D	21
2.5 Expressing Electric Fields in Terms of Scattering Parameters [1].....	24
2.5.1 Deriving the E-field Scattering Model.....	24

2.5.2	Expressing Vector Responses as Scalars	27
2.5.3	Sampling with Small Dipole Antennas	29
2.5.4	Scalar Responses in the Form of Scattering Parameters	30
2.6	Point-Spread Functions	34
2.7	An Extension of Born's Approximation	35
2.8	Discretizing the Region of Interest into Voxels	36
2.9	Conclusions	39
	References	39
Chapter 3 Quantitative Global Spectral Inversion		43
3.1	Introduction	43
3.2	Relating the Point-Spread Function to the Desired Response.....	44
3.3	Qualitative Maps for the Calibration Object	48
3.3.1	Generating the Qualitative Maps of the Calibration Object by a Coordinate Translation	48
3.3.2	Generating the Qualitative Maps of the Calibration Object by a Fourier Shift	50
3.4	Developing a Linear System of Equations for Quantitative Imaging	51
3.5	Applying Constraints to the System of Equations	52
3.6	Results	57
3.7	Conclusions	60
	References	61
Chapter 4 Quantitative Imaging Using Pointwise Spectral Inversion		63
4.1	Introduction	63
4.2	Using Pseudoinverse to Solve the Least-Squares Problem	64
4.2.1	Reformulating Matrices	64
4.2.2	Fourier Space Constraints	65
4.2.3	Quantitative Results with the Gamma Factor Set to Unity	65
4.2.4	Quantitative Results with the Quasi-Analytic Gamma Factor	66
4.3	Results	68
4.4	Conclusions	70

References	71
Chapter 5 Comparison of the Constrained Global Spectral Inversion and Pointwise Spectral Inversion Methods	73
5.1 Introduction	73
5.2 Results	74
5.2.1 F-shaped Target with Permittivity $9-j0$ and a Calibration Object of Permittivity $9-j0$	74
5.2.2 Small Scatterer with Permittivity $9-j0$ and a Calibration Object with Permittivity $9-j0$	78
5.2.3 F-shaped Target with Permittivity $9-j0$ and a Calibration Object with Permittivity $1.1-j0$	83
5.2.4 F-shaped Target with Permittivity $1.2-j0$ and a Calibration Object with Permittivity $9-j0$	86
5.3 Conclusions	90
References	91
Chapter 6 Conclusions and Future Work	93
6.1 Concluding Thoughts	93
6.2 Future Work	94
References	95
Bibliography	97

List of Figures

Figure 2.1 Simulation setup for planar raster scanning[7].	12
Figure 2.2 An illustration of the angles of reception and transmission in planar scanning.	16
Figure 2.3 The j -th antenna in Tx mode.	31
Figure 2.4 The j -th antenna in Rx mode.	32
Figure 2.5 Illustration of the position vectors of the voxel of interest, the receiving (Rx) antenna, and the transmitting (Tx) antenna.	37
Figure 3.1 Imaged area with scatterer in the centre of the ROI and the larger CO scanned area.	49
Figure 3.2 Offset imaged area where the CO data for a small-scatterer located at (x_p, y_p) is extracted as a subset of the CO measurement.	49
Figure 3.3 The CO scanning aperture for the Fourier shift method.	50
Figure 3.4 Algorithm flowchart of the constrained LS method.	56
Figure 3.5 The qualitative results of the F-shaped dielectric target.	57
Figure 3.6 Plotting image reconstruction with direct inversion of $\mathbf{A}\boldsymbol{\tau} = \mathbf{b}$: (a) the real part of the permittivity distribution, (b) the imaginary part of the permittivity distribution.	58
Figure 3.7 These are the quantitative results from the CGSI method: (a) the real part of the permittivity distribution, (b) the imaginary part of the permittivity distribution.	59
Figure 4.1 Algorithm flowchart of the pointwise spectral inversion (PSI) method.	67

- Figure 4.2 Results of the PSI method with $\Gamma_{\text{OUT}}(\mathbf{r})/\Gamma_{\text{CO}} \approx 1$: (a) the real part of the permittivity distribution, (b) the imaginary part of the permittivity distribution. 68
- Figure 4.3 Results of the PSI method with $\Gamma_{\text{OUT}}(\mathbf{r})/\Gamma_{\text{CO}} \neq 1$: (a) the real part of the permittivity distribution. (b) the imaginary part of the permittivity distribution. 69
- Figure 5.1 The PSI method for an F-shaped target with permittivity $9-j0$ and a CO of permittivity $9-j0$ with $\Gamma_{\text{OUT}}(\mathbf{r})/\Gamma_{\text{CO}} \approx 1$: (a) the real part of the permittivity distribution, (b) the imaginary part of the permittivity distribution. 74
- Figure 5.2 The PSI method for an F-shaped target with permittivity $9-j0$ and a CO of permittivity $9-j0$ with $\Gamma_{\text{OUT}}(\mathbf{r})/\Gamma_{\text{CO}} \neq 1$: (a) the real part of the permittivity distribution, (b) the imaginary part of the permittivity distribution. 75
- Figure 5.3 Qualitative holographic technique of the F-shaped target of permittivity $9-j0$ and CO of permittivity $9-j0$. 76
- Figure 5.4 The image reconstruction of the F-shape of permittivity $9-j0$ with a CO of permittivity $9-j0$ using the CGSI method: (a) the real part of the permittivity distribution, (b) the imaginary part of the permittivity distribution. 77
- Figure 5.5 The image reconstruction of a small scatterer of permittivity $9-j0$ with a CO of relative permittivity $9-j0$ using the PSI method where $\Gamma_{\text{OUT}}(\mathbf{r})/\Gamma_{\text{CO}} \approx 1$: (a) the real part of the permittivity distribution, (b) the imaginary part of the permittivity distribution. 79
- Figure 5.6 The image reconstruction using the PSI method for a small scatterer with permittivity of $9-j0$ and a CO with permittivity of $9-j0$ where $\Gamma_{\text{OUT}}(\mathbf{r})/\Gamma_{\text{CO}} \neq 1$: (a) the

real part of the permittivity distribution, (b) the imaginary part of the permittivity distribution.	80
Figure 5.7 Qualitative images of a small scatterer with permittivity $9-j0$ and a CO of permittivity $9-j0$.	81
Figure 5.8 The image reconstruction of a small scatterer of permittivity $9-j0$ using a CO with permittivity of $9-j0$ using the CGSI method: (a) the real part of the permittivity distribution, (b) the imaginary part of the permittivity distribution.	82
Figure 5.9 The image reconstruction of an F-shape with permittivity $9-j0$ and a CO of permittivity $1.1-j0$ using the PSI method where $\Gamma_{\text{OUT}}(\mathbf{r}) / \Gamma_{\text{CO}} \approx 1$: (a) the real part of the permittivity distribution, (b) the imaginary part of the permittivity distribution.	83
Figure 5.10 The image reconstruction of an F-shape with permittivity $9-j0$ and a CO of permittivity $1.1-j0$ using the PSI method where $\Gamma_{\text{OUT}}(\mathbf{r}) / \Gamma_{\text{CO}} \neq 1$: (a) The real part of the permittivity distribution. (b) The imaginary part of the permittivity distribution.	84
Figure 5.11 Qualitative results of F-shaped target with permittivity $9-j0$ and CO with permittivity $1.1-j0$.	84
Figure 5.12 The image reconstruction of the F-shape with a permittivity of $9-j0$ and a CO of permittivity of $1.1-j0$ using the CGSI method: (a) the real part of the permittivity distribution, (b) the imaginary part of the permittivity distribution.	85
Figure 5.13 The image reconstruction of an F-shaped target with permittivity $1.2-j0$ and CO with permittivity $9-j0$.with the PSI method where $\Gamma_{\text{OUT}}(\mathbf{r}) / \Gamma_{\text{CO}} \approx 1$: (a) The real part of the permittivity distribution, (b) The imaginary part of the permittivity distribution.	87

Figure 5.14 The image reconstruction of an F-shaped target with permittivity $1.1-j0$ and CO with permittivity $9-j0$.with the PSI method where $\Gamma_{\text{OUT}}(\mathbf{r}) / \Gamma_{\text{CO}} \neq 1$: (a) the real part of the permittivity distribution, (b) the imaginary part of the permittivity distribution. 88

Figure 5.15 Qualitative results of the F-shaped target with permittivity $1.2-j0$ and CO with permittivity $9-j0$. 89

Figure 5.16 Quantitative holography with the CGSI method permittivity $1.1-j0$ and CO with permittivity $1.1-j0$: (a) the real part of the permittivity distribution, (b) the imaginary part of the permittivity distribution. 89

List of Tables

Table 3.1 LS solving time for <i>lsqlin</i> MATLAB command [1].	54
Table 3.2 A comparison between the unconstrained $\mathbf{A}\boldsymbol{\tau} = \mathbf{b}$ and the constrained $\mathbf{C}\mathbf{x} = \mathbf{d}$.	59
Table 4.1 Comparison of the PSI and CGSI methods' runtimes and rRMSE.	69
Table 5.1 Comparison of the PSI methods and the CGSI method in the example with CO of permittivity $9-j0$ and F-shaped target of permittivity $9-j0$.	78
Table 5.2 Comparison of the PSI methods and the CGSI method in the example with CO of permittivity $9-j0$ and a small scatterer of permittivity $9-j0$.	82
Table 5.3 Comparison of the PSI methods and the CGSI method in the example with CO of permittivity $1.1-j0$ and an F-shaped target of permittivity $9-j0$.	86
Table 5.4 Comparison of the PSI methods and the CGSI method in the example with CO of permittivity $9-j0$ and an F-shaped target of permittivity $1.2-j0$.	90

List of Abbreviations

2D	Two Dimensional
3D	Three Dimensional
CO	Calibration Object
CGSI	Constrained Global Spectral Inversion
CWD	Concealed Weapon Detection
FT	Fourier Transform
GF	Gamma Factor
LS	Least Squares
LN	Localized Nonlinear
MRI	Magnetic Resonance Imaging
OBJ	Object
OUT	Object Under Test
PSF	Point-Spread Function
PSI	Pointwise Spectral Inversion
QA	Quasi-Analytic
RF	Radio-frequency
RO	Reference Object
ROI	Region of Interest
rRMSE	Relative Root-Mean Squared Error
Rx	Receiving
Tx	Transmitting
UGSI	Unconstrained Global Spectral Inversion

Chapter 1

Introduction

1.1 Background

Microwave imaging has a history of detecting targets with some of the most prominent examples being aircraft detection and underground sensing [1]–[3]. While there are many far-field applications that are capable of detecting the electrical properties of objects in the microwave bandwidth, like meteorology [4] and radiometry [5], there has been comparatively little work done on near-field imaging. One possible reason is that the near-field region has an unpredictable radiation pattern.

Recently, sensitivity-based imaging has been used to generate quantitative images of dielectric objects [6], [7]. However, other techniques exist that can provide near-field imaging results as well. One such technique is near-field *holography* proposed in [8] and [9].

Holography originated in the late 1940s as an image reconstruction technique discovered in the field of optics by Gabor and his colleagues [10]. The term *holography* has Greek origins with the word *holos* meaning “whole” and the word *graphos* meaning “writing” or “carving”. This is a commonly used technique to image objects, like aquatic microorganisms [11], [12]. However, it was not until the early 1970s that Farhat *et al.*

[13], [14] were capable of developing a holographic approach using microwaves. The relatively long wavelengths of microwave and millimetre waves allow for penetration inside dielectric bodies where visible light cannot reach [9]. This is attributed to the fact that the skin depth, which is inversely proportional to frequency, is larger for microwaves. The technique proposed by Farhat uses the amplitude and phase information of microwave signals and then solves a linearized inverse-scattering problem in the spectral domain (Fourier space) [8], [9], [13]–[15]. Not long after Farhat *et al.* published their work, Jacobi *et al.* were able to use microwaves to image canine kidneys immersed in water [16].

1.2 Motivation

Although microwave holography has been used in a variety of applications, the techniques in [3], [8], [9], [13], [14] and [16] deal with a holographic approach in a *qualitative* manner. However, many applications require a *quantitative* imaging technique. The difference between qualitative and quantitative imaging can be explained as follows.

Qualitative holography reconstructs images by displaying the shape of the object in the form of a two-dimensional (2D) or a three-dimensional (3D) image. The shape of the target is an indication of the locations where its constitutive parameters are different from those of the background. However, the actual values of these parameters as a function of space remain unknown. This is an acceptable technique for applications such as aircraft detection [1], [2], concealed weapon detection (CWD) [17]–[19] and any other

application that is concerned with determining the location and the shape of a target [8]–[10], [13], [14], [17]–[19]. However, its disadvantage is that it does not provide information about the electrical properties (*i.e.* the permittivity and conductivity) of the target. In the case of cancer screening, for example, the presence of contrast is insufficient to establish the presence of an abnormality. This is due to the fact that body parts contain fat, muscle, cartilage, and other tissues, which all have distinct electrical properties that contrast alone is unable to distinguish. The values of the real and imaginary parts of the complex permittivity in the imaged volume are desired for tissue imaging. In addition, iterative imaging methods require a quantitative estimate of the permittivity distribution inside the inspected object. Thus, a new approach to the solution of the microwave holography problem needs to be developed – a *quantitative* approach.

The primary difference between the *qualitative* and the *quantitative* reconstruction techniques is that a *quantitative* technique is capable of localizing and displaying the electrical properties of the objects as a function of position. The electrical property of interest is the permittivity, although conductivity could be analyzed as well as it is related simply to the imaginary part of the complex permittivity. This is the author’s contribution to near-field microwave imaging through microwave holography.

Microwave imaging technology is driven by the need for improved efficacy, lower cost, and increased user access. One of the motives for developing microwave imaging methods for tissue imaging, for example, is that it would be a cheaper and more widely available method of performing medical imaging compared to magnetic resonance imaging (MRI) or X-rays. This is due to the fact that MRI requires large spaces to house

the equipment and is also expensive to manufacture and to service. Typical MRI machines cost millions of dollars, whereas a microwave imaging system could cost tens of thousands of dollars. Moreover, it does not require large or shielded premises. In fact, it could be used in the offices of family physicians.

Microwave holography, along with other microwave imaging methods, has the advantage of using low radio-frequency (RF) power levels on the order of a typical cellular phone. As such, the patients and physicians need not be worried about burns – a concern that is all too common in the MRI community.

Microwave reconstruction techniques can use acquisition surfaces of various shapes. Typical shapes are planar, cylindrical and spherical. For example, the array of antennas in [20] is formed into a hemisphere so that it conforms to the shape of a human breast. For many women, mammography can be painful and this method has the capability of providing a safer, less painful method of examination.

As with any new technology, it is crucial to investigate under what circumstances it would be beneficial and under what circumstances it would fail. An entire chapter of this thesis is dedicated to the verification of the conditions under which accurate results can be obtained. This technology is limited by the fact that microwaves can only travel a short distance through human tissue before their signal becomes negligible. Unfortunately, many vital organs such as the kidneys, heart and lungs are not accessible through microwaves since they are too deep within the body. The other limitation of this technique is that it is unable to take into account the nonlinearities of the scattering

process, which is a consequence of using a direct inversion method. This can be overcome by techniques like the Born iterative method [21], however this requires an initial quantitative estimate. The results shown in this thesis are to be viewed as candidates for the initial values, which are to be supplied to the iterative solvers.

1.3 Contributions

The author has contributed to microwave imaging in the following ways:

- a) Developed and compared two methods to solve the near-field quantitative holographic problem that can reconstruct images in quasi-real time and in real time. Both methods solve linear systems of equations with a least-squares (LS) approach; however, one of these methods is significantly faster. Applying physically based constraints to the LS solution is also investigated.
- b) Developed a more efficient method of translating the calibration data throughout the region of interest (ROI) by applying a Fourier transform (FT) property.

Parts of this work have been published in [15].

1.4 Outline of the Thesis

This thesis intends to give a general study of the applicability of microwave holography and to extend this imaging method into a quantitative method. Thus, the problems presented in this work are generic. The technique proposed in this thesis is a combination of findings from subsurface imaging techniques using quasi-static fields and methods developed in qualitative holography [8], [9], [19], [22].

Chapter 2 provides the background of microwave holography. The chapter focuses on the most recent developments in near-field microwave holography and discusses technical aspects such as the scattering model and the practical realization of the imaging system.

Chapter 3 discusses the first method proposed by the author to the quantitative microwave holography problem. This chapter explains the derivation of an unconstrained global spectral inversion technique (UGSI) and a constrained global spectral inversion (CGSI) technique used to generate the quantitative images. It also discusses the implementation of the algorithm.

Chapter 4 discusses the second method proposed by the author to the quantitative microwave holography problem, namely, the pointwise spectral inversion (PSI) technique. This method may or may not include the localized nonlinear (LN) approximation to generate the images. The chapter also explains how the algorithm is implemented in the software. It provides examples and discusses the strengths and weaknesses of this unconstrained method as opposed to the one (CGSI) that uses constraints.

Chapter 5 provides examples with objects of various permittivity distributions. The goal of this chapter is to investigate which of the two methods performs better in terms of image fidelity.

Chapter 6 provides conclusions and discusses the inherent limitations of the proposed quantitative holography method. The chapter also discusses future work that could overcome the method's intrinsic limitations.

References

- [1] G.E. Smith, K. Woodbridge, C.J. Baker, and H. Griffiths, "Multistatic micro-Doppler radar signatures of personnel targets," *IET Signal Proc.*, vol. 4, no. 4, pp. 224-233, Jun. 2010.
- [2] J.M. Thomas, C.J. Baker, and H.D. Griffiths, "HF passive bistatic radar potential and applications for remote sensing," *New Trends for Environmental Monitoring for Passive Syst.*, 2008, pp. 1-5, Oct. 2008.
- [3] N. Osumi and K. Ueno, "Microwave holographic imaging of underground objects," *IEEE Trans. Antenna Propag.*, vol. 33, no. 2, pp. 152-159, Feb. 1985.
- [4] W.F. Hirschfeld, "The invention of radar meteorology," *Bulletin Amer. Meteorological Soc.*, vol. 67, no. 1, pp. 33-37, Jan. 1986.
- [5] M. Peichl, H. Suss, S. Dill, M. Greiner, and M. Jirousek, "Imaging technologies and applications of microwave radiometry," *Conf. Proc. 1st European Radar Conf.*, Wessling, Germany, 2004, pp. 269-273.
- [6] S. Tu, "Fast quantitative microwave imaging based on calibration measurements," Ph.D. Dissertation, Dept. Elect. and Comp. Eng., McMaster Univ., 2015.
- [7] S. Tu, J.J. McCombe, D.S. Shumakov, and N.K. Nikolova, "Fast quantitative microwave imaging with resolvent kernel extracted from measurements," *Inverse Problems*, vol. 31, no. 4, p. 045007 (33 pp.), April 2015.
- [8] R.K. Amineh, J. McCombe, A. Khalatpour, and N.K. Nikolova, "Microwave holography using point-spread functions measured with calibration objects," *IEEE Trans. Instrum. Meas.*, vol. 64, no. 2, pp. 403-417, Feb. 2015.

- [9] R.K. Amineh, M. Ravan, A. Khalatpour, and N.K. Nikolova, "Three-dimensional near field microwave holography using reflected and transmitted signals," *IEEE Trans. Antennas Propag.*, vol. 59, no. 12, pp. 4777-4789, Dec. 2011.
- [10] D. Gabor, "A new microscope principle," *Nature*, vol. 161, no. 4098, pp. 777-778, May 1948.
- [11] M. Jericho, H.J. Kreuzer, M. Kanka, and R. Riesenber, "Quantitative phase and refractive index measurements with point-source digital in-line holographic microscopy," *Appl. Optics*, vol. 51, no. 10, pp. 1503-1515, Mar. 2012.
- [12] S.K. Jericho, P. Klages, J. Nadeau, E.M. Dumas, M.H. Jericho, and H.J. Kreuzer, "In-line digital holographic microscopy for terrestrial and exobiological research," *Planetary and Space Sci.*, vol. 58, no. 4, pp. 701-705, Mar. 2010.
- [13] N.H. Farhat and W.R. Guard, "Millimeter wave holographic imaging of concealed weapons," *Proc. IEEE*, vol. 59, no. 9, pp. 1383-1384, Sept. 1971.
- [14] G. Tricoles and N.H. Farhat, "Microwave holography: Applications and techniques," *Proc. IEEE*, vol. 65, no. 1, pp. 108-121, Jan. 1977.
- [15] J.R. Thompson, J.J. McCombe, S. Tu, and N.K. Nikolova, "Quantitative imaging of dielectric objects based on holographic reconstruction," *Radar Conf. (RadarCon), 2015 IEEE*, pp. 0679-0683, 10-15 May 2015.
- [16] J.H. Jacobi, L.E. Larsen, and C.T. Hast, "Water-immersed microwave antennas and their application to microwave interrogation of biological targets," *IEEE Trans. Microwave Theory Tech.*, vol. MTT-27, no. 1, pp. 70-78, Jan. 1979.

- [17] D. Sheen, D.L. McMakin, and T. Hall, "Near-field three-dimensional radar imaging techniques and applications," *Appl. Optics*, vol. 49, no. 19, pp. E83-E93, July 2010.
- [18] D.M. Sheen, D.L. McMakin, and T.E. Hall, "Three-dimensional millimeter-wave imaging for concealed weapon detection," *IEEE Trans. Microwave Theory Tech.*, vol. 49, no. 9, pp. 1581-1592, Sept. 2001.
- [19] J.J. McCombe "Noise reduction in microwave imaging and detection," M.A.Sc. Thesis, Dept. Elect. and Comp. Eng., McMaster Univ., 2014.
- [20] M. Klemm, D. Gibbins, J. Leendertz, T. Horseman, A.W. Preece, R. Benjamin, and I.J. Craddock, "Development and testing of a 60-element UWB conformal array for breast cancer imaging," in *Proc. 5th European Conference on Antennas and Propagation (EuCAP)*, Rome, Italy, April 2011, pp. 3077-3079.
- [21] F. Li, Q.H. Liu, and L. Song, "Three-dimensional reconstruction of objects buried in layered media using Born and distorted Born iterative methods," *IEEE Geosci. Remote Sensing Lett.*, vol. 1, no. 2, April 2004.
- [22] T.M. Habashy, R.W. Groom, and B.R. Spies. "Beyond the Born and Rytov approximations: a nonlinear approach to electromagnetic scattering," *J. Geophys. Res.*, vol. 98, pp. 1759-1775, Feb. 1993.

Chapter 2

Background on Microwave Holography

2.1 Introduction

This chapter provides some background information on near-field microwave holography with an emphasis on the methods developed by our team. The goal of qualitative holographic reconstruction described here is to determine the shape and location of an object under test (OUT), where the OUT is an unknown object that is embedded in a known background medium.

The chapter begins by describing how the scattering model, which is based on the electric field vector, is used in the image reconstruction process. We then derive the relation between the scattered electric field and the measured scattering parameters (S -parameters) [1]. This novel derivation is critical in formulating a mathematically rigorous forward scattering model in terms of S -parameters.

We then summarize the work done by Sheen *et al.* [2] on concealed weapon detection (CWD) and discuss their contribution in the framework of our S -parameter forward model. This work provides the basic concept of far-field microwave holography, which is necessary to understand our team's developments in near-field holography. Initially, our team developed a near-field two-dimensional (2D) holographic reconstruction technique

at a single frequency [3]. This has been extended to three dimensions (3D) by including a range of frequencies [4].

In both the 2D and 3D cases, Green's function of the background medium plays a vital role in the reconstruction process. Initially, our team used a spherical wave propagation model to represent Green's function [3]. Later, the approach was generalized to the near-field region where the spherical-wave approximation is inadequate. This was achieved by acquiring the near-field incident fields of the antennas used for scanning via method-of-moment simulations [5]. However, the fidelity of the simulations has been found to be low due to large modelling errors. The point-spread function (PSF) is then introduced as a measureable quantity characterizing the acquisition system and its background Green's function [6].

2.2 Planar Raster Scanning Acquisition Setup

Our work uses *a priori* knowledge of: (i) the incident-field distributions, (ii) the permittivity of the small scatterer and (iii) the permittivity of the background medium. To characterize the acquisition system, two types of measurements are performed: measurements of the reference object (RO) and measurements of the calibration object (CO). The RO is an object with no scatterers, which contains the background medium and the whole acquisition setup, including the antennas. The CO is identical to the RO with the exception of a small scatterer, which is embedded in the centre of the RO [7][8].

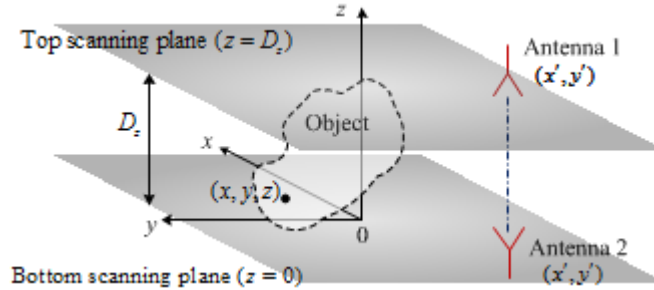


Figure 2.1 Simulation setup for planar raster scanning [8].

Figure 2.1 illustrates the setup for a planar raster scanning data acquisition system, which is the system used for all examples in this thesis. Planar scanning is a data acquisition technique similar to synthetic aperture radar techniques since the antennas are scanned over a top and a bottom plane. The antennas are positioned such that they are aligned along their boresight.

2.3 Forward Model in Terms of Scattered Electric Fields

Every reconstruction algorithm assumes a certain model for its forward solution. The original holographic reconstruction algorithm is based on a scalar approximation of the electromagnetic scattering model. This is why it is imperative to review briefly the scattering model for the \mathbf{E} -field vector and describe the approximations made when it is reduced to a scalar model.

The total electric field can be expressed as the superposition of the incident and scattered fields [9]:

$$\mathbf{E}_{\text{OBJ},k}^{\text{tot}}(\mathbf{r}_j) = \mathbf{E}_{\text{OBJ},k}^{\text{inc}}(\mathbf{r}_j) + \mathbf{E}_{\text{OBJ},k}^{\text{sc}}(\mathbf{r}_j), \quad (2.1)$$

where k and j represent the indices of the transmitting (Tx) and receiving (Rx) antennas, respectively, and $\text{OBJ} \equiv \text{OUT}, \text{CO}, \text{RO}$. The coordinates of the Rx antenna are defined as $\mathbf{r}_j = (x_j, y_j, 0)$ and the coordinates of the Tx antenna are $\mathbf{r}_k = (x_k, y_k, D_z)$. Note that since the antennas are aligned along their boresight, $x_k = x_j = x'$ and $y_k = y_j = y'$. Thus, we define the scanning aperture coordinates to be $\mathbf{r}' = (x', y', \bar{z})$, with $\bar{z} = 0, D_z$.

Helmholtz' equation allows us to express the scattered field as [9]

$$\mathbf{E}_{\text{OBJ},k}^{\text{sc}}(\mathbf{r}_j) = \iiint_V \left[k_{\text{OBJ}}^2(\mathbf{r}) - k_{\text{RO}}^2(\mathbf{r}) \right] \bar{\mathbf{G}}_b(\mathbf{r}_j, \mathbf{r}) \mathbf{E}_{\text{OBJ},k}^{\text{tot}}(\mathbf{r}) d\mathbf{r}, \quad (2.2)$$

where $\bar{\mathbf{G}}_b(\mathbf{r}_j, \mathbf{r})$ is Green's function of the background medium. The goal of qualitative holography is to reconstruct the contrast function $f(\mathbf{r}) = k_{\text{OBJ}}^2(\mathbf{r}) - k_{\text{RO}}^2(\mathbf{r}) = k_0^2 \Delta \varepsilon_{\text{OBJ}}(\mathbf{r})$, where k_0 is the wavenumber in free-space, $k_{\text{OBJ}}(\mathbf{r}) = \omega \sqrt{\mu_{\text{OBJ}}(\mathbf{r}) \varepsilon_{\text{OBJ}}(\mathbf{r})}$ is the wavenumber of OBJ and $\Delta \varepsilon_{\text{OBJ}}(\mathbf{r}) = \varepsilon_{\text{OBJ},r}(\mathbf{r}) - \varepsilon_{\text{RO},r}(\mathbf{r})$ is the relative permittivity contrast of OBJ.

Previously, the 2D and 3D qualitative holographic techniques used the linear Born approximation to replace the total internal field with the incident field [9]:

$$\mathbf{E}_{\text{OBJ},k}^{\text{tot}}(\mathbf{r}) \approx \mathbf{E}_{\text{OBJ},k}^{\text{inc}}(\mathbf{r}). \quad (2.3)$$

Since by definition the RO does not contain scatterers, it can be stated that

$\mathbf{E}_{\text{OBJ},k}^{\text{inc}}(\mathbf{r}) \approx \mathbf{E}_{\text{RO},k}(\mathbf{r})$. Thus, under the linear Born approximation, (2.2) is written as [9]

$$\mathbf{E}_{\text{OBJ},k}^{\text{sc}}(\mathbf{r}_j) \approx \iiint_V k_0^2 \Delta \varepsilon_{\text{OBJ}}(\mathbf{r}) \bar{\mathbf{G}}_b(\mathbf{r}_j, \mathbf{r}) \mathbf{E}_{\text{RO},k}(\mathbf{r}) d\mathbf{r}. \quad (2.4)$$

The above equation is the well-known **E**-field linearized scattering model.

2.4 Prior Developments in Qualitative Holography

2.4.1 The Scalar Model of Holography

The work done by Sheen *et al.* [2] applies (2.4) with far-zone measurements. In addition, the expression (2.4) is only analyzed for one scalar component [2]:

$$E_{\text{OBJ},k}^{\text{sc}}(\mathbf{r}_j) \approx \iiint_V k_0^2 \Delta \varepsilon_{\text{OBJ}}(\mathbf{r}) G_b(\mathbf{r}_j, \mathbf{r}) E_{\text{RO},k}(\mathbf{r}) d\mathbf{r}. \quad (2.5)$$

This implies that Green's function is a scalar thereby ignoring polarization effects (*e.g.* cross-polarization scattering). The work in [2] uses a background of air. Thus, Green's function of the scalar Helmholtz' equation in open-space can be written as [9]

$$\frac{e^{-jk_b|\mathbf{r}-\mathbf{r}_j|}}{|\mathbf{r}-\mathbf{r}_j|}, \quad (2.6)$$

where $j = \sqrt{-1}$. Since the work in [2] considers only far-field data, the incident field in (2.5) is approximated as $\sim e^{-jk_b|\mathbf{r}-\mathbf{r}_i|}$ while Green's function is written as $e^{-jk_b|\mathbf{r}-\mathbf{r}_j|}$. In these approximate far-field expressions, the $1/|\mathbf{r}-\mathbf{r}_j|$ factor has been neglected. Since the work done in [2] uses a monostatic arrangement, only reflection coefficients are measured. Thus, the Rx and Tx coordinates are the same, *i.e.* $\mathbf{r}_j = \mathbf{r}_k$. Therefore, the image reconstruction algorithm in [2] is based on

$$E_{\text{OBJ},k}^{\text{sc}}(\mathbf{r}_j) \approx \iiint_V k_0^2 \Delta \varepsilon_{\text{OBJ}}(\mathbf{r}) e^{-j2k_b \sqrt{(x-x_j)^2 + (y-y_j)^2 + (z-\bar{z})^2}} d\mathbf{r}, \quad (2.7)$$

where the goal of the algorithm is to reconstruct the reflectivity function $f(\mathbf{r}) = k_0^2 \Delta \varepsilon_{\text{OBJ}}(\mathbf{r})$. It is now clear that this forward model is valid only for the case of far-zone scattering and is not capable of representing cross-polarization scattering.

In addition, the work in [2] performs FTs in 3D space and assumes that $k_z = \sqrt{k_b^2 - k_x^2 - k_y^2}$, where $k_b, k_x, k_y, k_z \in \mathbb{R}$. This implies far-field propagation in a lossless medium. Also, the spatial frequencies, k_x and k_y , cannot exceed $2k$. This limits the resolution along the x and y axes since some higher frequency components (e.g., evanescent field), which provide image sharpness, are discarded. These approximations are not suitable for our work since the objects we are interested in are lossy and $k_b^2 \neq k_x^2 + k_y^2 + k_z^2$ in the near-field region. The 3D FT used in [3] is avoided in the reconstruction technique proposed by our team. This procedure is discussed in detail later.

2.4.2 Depth and Lateral Resolution

In the proposed techniques in [3], [4], [6], [9] and [10] the upper limits on k_x and k_y are not limited by k_z . This allows for better cross-range resolution, which can be defined as [3]

$$\delta_w = \frac{\pi}{k_{w,\max}} = \frac{\pi}{k_b (\sin(\theta_t/2) + \sin(\theta_r/2))} = \frac{\lambda_b}{2(\sin(\theta_t/2) + \sin(\theta_r/2))}, \quad (2.8)$$

where $k_{w,\max}$ ($w \equiv x, y$) is dependent on the transmission and receiving paths of the wave and λ_b is the wavelength in the background medium [3]. The angles θ_r (angle of reception) and θ_t (angle of transmission) defined in [3] are illustrated in Figure 2.2.

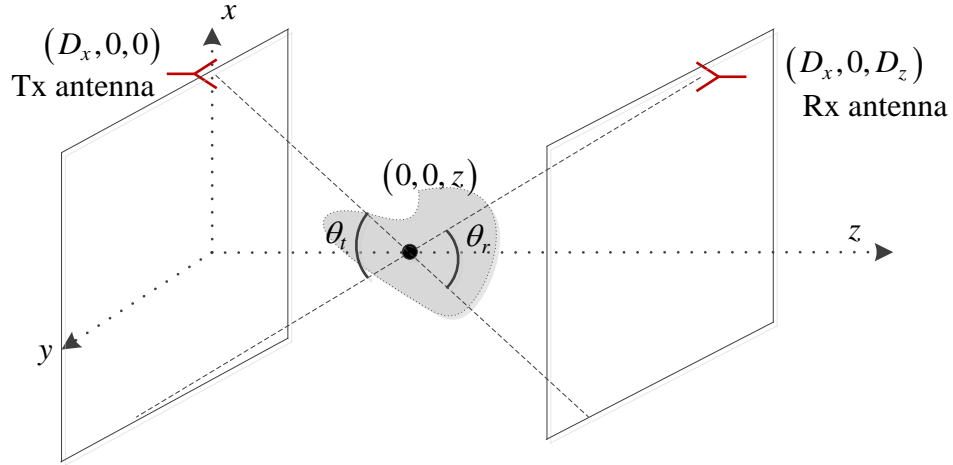


Figure 2.2 An illustration of the angles of reception and transmission in planar scanning.

The depth resolution stated in [2] and [4] is

$$\delta_z = \frac{c}{2B}, \quad (2.9)$$

with c being the wave velocity in the background medium and B is the frequency bandwidth. This resolution estimate is valid only in the far-zone and only for reflection-based measurements. In principle, there is no depth resolution in a transmission measurement when using a single receiving antenna.

2.4.3 Spatial and Frequency Sampling for 2D and 3D Holography

The FT is used on the acquired data along the x' and y' coordinates, respectively. The variables k_x and k_y are the Fourier variables for x' and y' , respectively. The sampling size (defined in [2] and [4]) along the x' and y' coordinates are chosen such that

$$\Delta x < \frac{\lambda_{\min}}{4}. \quad (2.10)$$

As per Nyquist's theorem, the maximum values of k_x and k_y are chosen such that [6]

$$\beta^{\max} = \frac{\pi}{\Delta\varphi}, \quad \beta \triangleq k_x, k_y, \quad \varphi \triangleq x, y. \quad (2.11)$$

In addition, since the coordinate pair $(x', y') \in \mathbb{R}$, symmetry in the negative spatial frequencies must be satisfied. Therefore, the domain of spatial frequencies are $-k_x^{\max} \leq k_x \leq k_x^{\max}$ and $-k_y^{\max} \leq k_y \leq k_y^{\max}$.

The required frequency sampling is done in the same manner as the sampling step size along the x' and y' coordinates [2]. The phase shift resulting from a change in wavenumber Δk for reflection measurements is $2\Delta k R_{\max}$, where R_{\max} is the maximum target range. In order that these quantities not exceed π , the frequency sampling step size (defined in [2] and [4]) for reflection measurements needs to be

$$\Delta f < \frac{c}{4R_{\max}}, \quad (2.12)$$

where Δf is the frequency sampling step size. Likewise, the phase shift resulting in a change in wavenumber Δk for transmission measurements is $\Delta k(R_1 + R_2)$, where R_1 is the distance from the Tx to the scattering point and R_2 is the distance from the scattering point to the Rx. In order these quantities to not exceed π , the frequency sampling step size for transmission measurements needs to be [4]

$$\Delta f < \frac{c}{2(R_1 + R_2)}. \quad (2.13)$$

For all examples presented in this thesis, the frequency sampling step size is 1 GHz.

2.4.4 Estimates of Green's Function

We make the assumption that we know the incident field $\mathbf{E}^{\text{inc}}(0, 0, 0; x, y, z; \omega_m)$ at every m -th angular frequency and at every point in the ROI (x, y, z) when the transmitting antenna is at $(0, 0, 0)$ [6]:

$$\begin{aligned} \mathbf{E}_0^{\text{inc}}(x, y, z, \omega_m) &\equiv \mathbf{E}^{\text{inc}}(0, 0, 0; x, y, z; \omega_m), \\ \bar{\mathbf{G}}_{b0}(x, y, z, \omega_m) &\equiv \bar{\mathbf{G}}_b(x, y, z; 0, 0, D_z; \omega_m), \end{aligned} \quad (2.14)$$

where the incident field has the form $\mathbf{E}^{\text{inc}}(\mathbf{r}_p, \mathbf{r}_Q; \omega_m)$ with \mathbf{r}_p being the observation point and \mathbf{r}_Q is the scattering point. For a homogeneous or layered medium, the incident field and Green's function satisfy the translation property [3], [4], [6]–[8], [10], [11], [12]

$$\begin{aligned} \mathbf{E}^{\text{inc}}(x', y', 0; x, y, z; \omega_m) &= \mathbf{E}_0^{\text{inc}}(x' - x, y' - y, z, \omega_m), \\ \bar{\mathbf{G}}_b(x', y', 0; x, y, z; \omega_m) &= \bar{\mathbf{G}}_{b0}(x' - x, y' - y, z, \omega_m). \end{aligned} \quad (2.15)$$

This property allows us to express the scattered field integral of (2.2) as a convolution, which is capable of taking advantage of some useful FT properties.

The 2D image reconstruction method presented in [3] involves having two antennas along their boresight and assumes that the incident wave (s^{inc}) is known inside the scanned object when the Tx antenna is at the origin:

$$s_0^{\text{inc}}(x, y, z) \equiv s^{\text{inc}}(x, y, z; 0, 0, 0), \quad (2.16)$$

with (x, y, z) being the observation point and $(0, 0, 0)$ being the origin. The wave is assumed to be spherical and it describes Green's function, which has the same form as (2.6) with $\mathbf{r}_j = \mathbf{r}'$. Therefore, the scattered wave observed at one of the acquisition planes is expressed in [3] as

$$\begin{aligned} s(x', y') &= \iint_{x y} f(x, y, z) \frac{s_0^{\text{inc}}(x' - x, y' - y, z) e^{-jk_b \sqrt{(x' - x)^2 + (y' - y)^2 + (D_z - z)^2}}}{\sqrt{(x' - x)^2 + (y' - y)^2 + (D_z - z)^2}} dx dy \\ &= \iint_{x y} f(x, y, z) g(x' - x, y' - y, z) dx dy, \end{aligned} \quad (2.17)$$

where the quantities of (2.17) are defined as [3]

$$s_0(x, y, z) = s_0^{\text{inc}}(-x, -y, z), \quad (2.18)$$

and [3]

$$g_0(x, y, z) = \frac{s_0(x, y, z) e^{-jk_b \sqrt{x^2 + y^2 + (D_z - z)^2}}}{\sqrt{x^2 + y^2 + (D_z - z)^2}}. \quad (2.19)$$

Notice that this forward model is also scalar as in [2] but now it approximates Green's function as a spherical wave where the amplitude factor $1/|\mathbf{r}'-\mathbf{r}|$ is not ignored.

This allows us to express (2.17) in Fourier space as being a product [3]

$$\tilde{S}(k_x, k_y) = \tilde{F}(k_x, k_y, z) \tilde{G}_0(k_x, k_y, z), \quad (2.20)$$

where the tilde above the variables indicates that the FT has been applied.

From (2.20), a formal inversion expression is obtained for the contrast function as [3]

$$f(x, y, z) = \mathcal{F}_{2D}^{-1} \left\{ \frac{\tilde{S}(k_x, k_y)}{\tilde{G}_0(k_x, k_y, z)} \right\}, \quad (2.21)$$

where \mathcal{F}_{2D}^{-1} denotes the 2D inverse FT. The reconstructed image is obtained by taking the magnitude of (2.21), *i.e.* $|f(x, y, z)|$ [3]. Note that (2.21) is only a formal expression. It is to be viewed as the maximum likelihood solution and is not applicable in cases where $\tilde{G}_0(k_x, k_y, z)$ is zero. A practical approach is presented next.

2.4.5 Solving the Least-Square Holography Problems in 2D

Since we have multiple signals, (2.21) cannot be directly applied. It can be advantageous to use as much data as possible to reconstruct the image. However, this is dependent on the quality of the new data and whether the new data is sufficiently different. If these conditions are not met, the matrix can become rank deficient.

The number of signals N_s is a product of two quantities $N_s = N_{Tx}N_{Rx}$, where N_{Tx} is the number of transmitting ports and N_{Rx} is the number of receiving ports. The following system of equations, solved at each (k_x, k_y) pair, is obtained in the case of a two-port system [3]:

$$\begin{bmatrix} \tilde{S}_{11}(k_x, k_y) \\ \tilde{S}_{12}(k_x, k_y) \\ \tilde{S}_{21}(k_x, k_y) \\ \tilde{S}_{22}(k_x, k_y) \end{bmatrix} = \tilde{F}(k_x, k_y, z) \begin{bmatrix} \tilde{G}_0^{11}(k_x, k_y, z) \\ \tilde{G}_0^{12}(k_x, k_y, z) \\ \tilde{G}_0^{21}(k_x, k_y, z) \\ \tilde{G}_0^{22}(k_x, k_y, z) \end{bmatrix}. \quad (2.22)$$

This is an overdetermined system since there are four equations and one unknown [3]. Therefore, the pseudoinverse command in MATLAB (*pinv*) is applied at each (k_x, k_y) pair [13].

2.4.6 Building the Least-Square Problem in 3D

The scalar model in (2.17) can be generalized for the 3D case with the addition of data at multiple frequencies, *i.e.*, using wideband measurements, [4], [6], [10], [11]:

$$\Delta S_{\text{OUT},q}(x', y', \bar{z}, \omega_m) = \iiint_{\mathcal{V}} f(x, y, z) g_0^q(x' - x, y' - y, z, \omega_m) dx dy dz, \quad (2.23)$$

where $m = 1, \dots, N_\omega$, $q = 1, \dots, N_s$ and $\bar{z} = 0, D$. Like the 2D case, the scattering function $g_0(x, y, z)$ satisfies translational invariance and allows us to express (2.23) as a product in Fourier space [4], [6], [10], [11],

$$\Delta \tilde{S}_{\text{OUT},q}(k_x, k_y, \bar{z}, \omega_m) = \int_z \tilde{F}(k_x, k_y, z) \tilde{G}_0^q(k_x, k_y, z, \omega_m) dz, \quad (2.24)$$

which can be discretized as [4], [6], [10], [11]

$$\Delta\tilde{S}_{\text{OUT},q}(k_x, k_y, \bar{z}, \omega_m) \approx \sum_{n=1}^{N_z} \tilde{F}(k_x, k_y, z_n) \tilde{G}_0^q(k_x, k_y, \omega_m; z_n) \Delta z. \quad (2.25)$$

Hereafter, Δz is omitted since the qualitative approach normalizes the result at the end of the algorithm. Therefore, we can express (2.25) in the form of a matrix as [4], [6], [10], [11]

$$\begin{bmatrix} \Delta\tilde{S}_{\text{OUT},1}(\boldsymbol{\kappa}, \bar{z}, \omega_m) \\ \vdots \\ \Delta\tilde{S}_{\text{OUT},N_s}(\boldsymbol{\kappa}, \bar{z}, \omega_m) \end{bmatrix} = \begin{bmatrix} \tilde{G}_0^1(\boldsymbol{\kappa}, \omega_m, z_1) & \cdots & \tilde{G}_0^1(\boldsymbol{\kappa}, \omega_m, z_{N_z}) \\ \vdots & \ddots & \vdots \\ \tilde{G}_0^{N_s}(\boldsymbol{\kappa}, \omega_m, z_1) & \cdots & \tilde{G}_0^{N_s}(\boldsymbol{\kappa}, \omega_m, z_{N_z}) \end{bmatrix} \begin{bmatrix} \tilde{F}_{\text{OUT}}(\boldsymbol{\kappa}, z_1) \\ \vdots \\ \tilde{F}_{\text{OUT}}(\boldsymbol{\kappa}, z_{N_z}) \end{bmatrix}, \quad (2.26)$$

where the Fourier pair is defined as $\boldsymbol{\kappa} = (k_x, k_y)$. The system (2.26) can be written at each angular frequency ω_m ($m=1, \dots, N_\omega$). However, we would like to solve (2.26) for all angular frequencies simultaneously. Therefore, we need to construct vectors of data and contrast values that comprise all angular frequencies.

Let us denote a column in the system matrix of (2.26) as [4], [6], [10], [11]

$$\tilde{\mathbf{G}}(\boldsymbol{\kappa}, \omega_m, z_n) = \begin{bmatrix} \tilde{G}_0^1(\boldsymbol{\kappa}, \omega_m, z_n) \\ \vdots \\ \tilde{G}_0^{N_s}(\boldsymbol{\kappa}, \omega_m, z_n) \end{bmatrix}. \quad (2.27)$$

In order to achieve good depth resolution in our image reconstruction, we define a system matrix that combines all of the angular frequencies together [4], [6], [10], [11]:

$$\underline{\tilde{\mathbf{K}}}(\boldsymbol{\kappa}) = \begin{bmatrix} \tilde{\mathbf{G}}(\boldsymbol{\kappa}, \omega_1; z_1) & \cdots & \tilde{\mathbf{G}}(\boldsymbol{\kappa}, \omega_1; z_{N_z}) \\ \vdots & & \vdots \\ \tilde{\mathbf{G}}(\boldsymbol{\kappa}, \omega_{N_\omega}; z_1) & \cdots & \tilde{\mathbf{G}}(\boldsymbol{\kappa}, \omega_{N_\omega}; z_{N_z}) \end{bmatrix}, \quad m = 1, \dots, N_\omega. \quad (2.28)$$

Next, let us denote the column vector of N_s responses at a particular angular frequency as [4], [6], [10], [11]:

$$\Delta \tilde{\mathbf{S}}_{\text{OUT}}(\boldsymbol{\kappa}, \omega_m) = \begin{bmatrix} \Delta \tilde{\mathbf{S}}_{\text{OUT},1}(\boldsymbol{\kappa}, \bar{z}, \omega_m) \\ \vdots \\ \Delta \tilde{\mathbf{S}}_{\text{OUT},N_s}(\boldsymbol{\kappa}, \bar{z}, \omega_m) \end{bmatrix}, \quad m = 1, \dots, N_\omega. \quad (2.29)$$

We combine the responses (2.29) for all angular frequencies into a single vector as [4], [6], [10], [11]:

$$\underline{\tilde{\mathbf{S}}}_{\text{OUT}}(\boldsymbol{\kappa}) = \begin{bmatrix} \Delta \tilde{\mathbf{S}}_{\text{OUT}}^T(\boldsymbol{\kappa}, \omega_1) \\ \vdots \\ \Delta \tilde{\mathbf{S}}_{\text{OUT}}^T(\boldsymbol{\kappa}, \omega_{N_\omega}) \end{bmatrix}. \quad (2.30)$$

As a result, we obtain a system of equations at each $\boldsymbol{\kappa}$ pair that combines all angular frequencies [4], [6], [10], [11]:

$$\underline{\tilde{\mathbf{K}}}(\boldsymbol{\kappa}) \underline{\tilde{\mathbf{F}}}_{\text{OUT}}(\boldsymbol{\kappa}) = \underline{\tilde{\mathbf{S}}}_{\text{OUT}}(\boldsymbol{\kappa}). \quad (2.31)$$

Since this relationship is overdetermined, we use the MATLAB command *pinv* to acquire the qualitative maps (i.e., the image of the contrast function) of the OUT, $\underline{\tilde{\mathbf{F}}}_{\text{OUT}}(\boldsymbol{\kappa})$.

2.5 Expressing Electric Fields in Terms of Scattering Parameters [1]

All scalar models of scattering considered so far assume that one field component is sampled at a point. In practice, we measure the S -parameters of the network formed by the OUT and the antennas in the acquisition setup. The S -parameters are not equal, nor are they proportional to one field component at the centre of the Rx antenna.

We must reduce (2.4) to a scalar form corresponding to the S -parameters in order to have an accurate model of our experiments and simulations. The following derivation casts the integral-equation model directly in terms of the S -parameters and the incident field generated by the Tx antenna and that generated by the Rx antenna, where the latter operates in a Tx mode. To our knowledge, this derivation is novel and is not available elsewhere. At the same time, it is critical to understand the forward scattering model of near-field holography.

2.5.1 Deriving the E-field Scattering Model

The vector Helmholtz equation for an electric field in a nonmagnetic isotropic medium can be written as

$$\nabla \times \nabla \times \mathbf{E} - k_0^2 \varepsilon_r \mathbf{E} = -j\omega\mu_0 \mathbf{J}, \quad (2.32)$$

where ε_r is the complex relative permittivity [9].

Green's function of the vector Helmholtz equation is a tensor that solves

$$\nabla \times \nabla \times \bar{\mathbf{G}}_b(\mathbf{r}', \mathbf{r}) - k_0^2 \epsilon_r \bar{\mathbf{G}}_b(\mathbf{r}', \mathbf{r}) = -\bar{\mathbf{I}} \delta(\mathbf{r}' - \mathbf{r}), \quad (2.33)$$

where $\bar{\mathbf{I}}$ is the identity tensor and $\delta(\bullet)$ is Dirac's delta function. Thus,

$$\bar{\mathbf{I}} \delta(\bullet) = \begin{bmatrix} \delta(\bullet) & 0 & 0 \\ 0 & \delta(\bullet) & 0 \\ 0 & 0 & \delta(\bullet) \end{bmatrix}. \quad (2.34)$$

The relation in (2.33) can be decomposed into components such that

$$\begin{aligned} \nabla \times \nabla \times \mathbf{G}_x(\mathbf{r}', \mathbf{r}) - k_0^2 \epsilon_r \mathbf{G}_x(\mathbf{r}', \mathbf{r}) &= -\delta(\mathbf{r}' - \mathbf{r}) \hat{\mathbf{x}}, \\ \nabla \times \nabla \times \mathbf{G}_y(\mathbf{r}', \mathbf{r}) - k_0^2 \epsilon_r \mathbf{G}_y(\mathbf{r}', \mathbf{r}) &= -\delta(\mathbf{r}' - \mathbf{r}) \hat{\mathbf{y}}, \\ \nabla \times \nabla \times \mathbf{G}_z(\mathbf{r}', \mathbf{r}) - k_0^2 \epsilon_r \mathbf{G}_z(\mathbf{r}', \mathbf{r}) &= -\delta(\mathbf{r}' - \mathbf{r}) \hat{\mathbf{z}}, \end{aligned} \quad (2.35)$$

where $\mathbf{G}_\rho = [G_{x\rho} \ G_{y\rho} \ G_{z\rho}]^T$ ($\rho \equiv x, y, z$) is the field due to a δ -source of ρ polarization.

As shown by Chew [9], if the current source function $\mathbf{J}(\mathbf{r}')$ is known, the field it generates can be expressed as

$$\mathbf{E}(\mathbf{r}', \omega_m) = -j\omega_m \mu_0 \iiint_{V_S} \bar{\mathbf{G}}_b(\mathbf{r}', \mathbf{r}) \mathbf{J}(\mathbf{r}) d\mathbf{r}, \quad (2.36)$$

where V_S is the volume of interest and the differential contribution to $\mathbf{E}(\mathbf{r}')$ can be expressed in the form of a tensor

$$\begin{bmatrix} \delta E_x \\ \delta E_y \\ \delta E_z \end{bmatrix}_{(\mathbf{r}')} = j\omega_m \mu_0 \begin{bmatrix} G_{xx} & G_{xy} & G_{xz} \\ G_{yx} & G_{yy} & G_{yz} \\ G_{zx} & G_{zy} & G_{zz} \end{bmatrix}_{(\mathbf{r}', \mathbf{r})} \begin{bmatrix} J_x \\ J_y \\ J_z \end{bmatrix}_{(\mathbf{r})} dV. \quad (2.37)$$

For the imaging examples in this thesis, we assume a uniform background medium, which has no sources inside the imaged volume, *i.e.* $\mathbf{J}(\mathbf{r}) = 0$. As follows from (2.32), the incident field satisfies the homogenous vector Helmholtz equation

$$\nabla \times \nabla \times \mathbf{E}^{\text{inc}} - k_0^2 \varepsilon_r \mathbf{E}^{\text{inc}} = 0. \quad (2.38)$$

However, when a scatterer is present in the ROI, the permittivity differs from the background medium. The total field in the ROI satisfies

$$\nabla \times \nabla \times \mathbf{E}^{\text{tot}} - k_0^2 (\varepsilon_r + \Delta \varepsilon_{\text{OBJ}}) \mathbf{E}^{\text{tot}} = 0. \quad (2.39)$$

By substituting (2.1) into (2.39) we get

$$\nabla \times \nabla \times (\mathbf{E}^{\text{inc}} + \mathbf{E}^{\text{sc}}) - k_0^2 \varepsilon_r (\mathbf{E}^{\text{inc}} + \mathbf{E}^{\text{sc}}) - k_0^2 \Delta \varepsilon_{\text{OUT}} \mathbf{E}^{\text{tot}} = 0. \quad (2.40)$$

We then arrange (2.40) such that we separate the incident, scattered and total fields:

$$\left(\nabla \times \nabla \times \mathbf{E}^{\text{inc}} - k_0^2 \varepsilon_r \mathbf{E}^{\text{inc}} \right) + \left(\nabla \times \nabla \times \mathbf{E}^{\text{sc}} - k_0^2 \varepsilon_r \mathbf{E}^{\text{sc}} \right) = k_0^2 \Delta \varepsilon_{\text{OBJ}} \mathbf{E}^{\text{tot}}. \quad (2.41)$$

We recognize that (2.38) can be used to simplify (2.41) such that

$$\nabla \times \nabla \times \mathbf{E}^{\text{sc}} - k_0^2 \varepsilon_r \mathbf{E}^{\text{sc}} = k_0^2 \Delta \varepsilon_{\text{OUT}} \mathbf{E}^{\text{tot}}. \quad (2.42)$$

We then compare the right-hand side of (2.42) with (2.32) to relate the total field to an equivalent current distribution, \mathbf{J}_e

$$\begin{aligned} -j\omega\mu_0 \mathbf{J}_e &= k_0^2 \Delta \varepsilon_{\text{OUT}} \mathbf{E}^{\text{tot}}, \\ \mathbf{J}_e &= \frac{jk_0^2}{\omega\mu_0} \Delta \varepsilon_{\text{OUT}} \mathbf{E}^{\text{tot}}. \end{aligned} \quad (2.43)$$

Substituting (2.43) into (2.36) gives

$$\mathbf{E}^{\text{sc}}(\mathbf{r}', \omega_m) = \iiint_{V_S} k_0^2 \Delta \varepsilon_{\text{OUT}}(\mathbf{r}) \bar{\mathbf{G}}_b(\mathbf{r}', \mathbf{r}) \mathbf{E}^{\text{tot}}(\mathbf{r}) d\mathbf{r}. \quad (2.44)$$

The significance of expressing the scattered field in terms of the total field rather than the current distribution will be shown in the subsequent sections.

2.5.2 Expressing Vector Responses as Scalars

Let us assume that the j -th sensor is transmitting and its current distribution can be expressed as

$$\mathbf{J}_j(\mathbf{r}') = m_j \mathbf{M}_j(\mathbf{r}'), \quad (2.45)$$

where m_j is the strength of the excitation and $\mathbf{M}_j(\mathbf{r}')$ is the source vector distribution.

We then consider the source's domain to be ∂_j , where $\mathbf{M}_j(\mathbf{r}') \neq 0$ only if $\mathbf{r}' \in \partial_j$. Then, as per (2.36), the field generated by the j -th Tx port can be expressed as

$$\mathbf{E}_j^{\text{inc}}(\mathbf{r}', \omega_m) = -j\omega_m \mu_0 m_j \int_{\partial_j} \bar{\mathbf{G}}_b(\mathbf{r}', \mathbf{r}) \mathbf{M}_j(\mathbf{r}) d\mathbf{r}. \quad (2.46)$$

Let us now assume the same j -th sensor is in Rx mode when the k -th sensor transmits. As indicated in (2.37) and (2.44), the differential contribution to the scattered field at the location of the sensor is

$$\delta \mathbf{E}_{jk}^{\text{sc}}(\mathbf{r}', \omega_m) = k_0^2 \Delta \varepsilon_{\text{OUT}}(\mathbf{r}) \bar{\mathbf{G}}_b(\mathbf{r}', \mathbf{r}) \mathbf{E}_k^{\text{tot}}(\mathbf{r}) d\mathbf{r}. \quad (2.47)$$

Based on how S -parameters are defined in [14], we now make the assumption that the scalar response of the j -th sensor can be expressed as

$$R_{jk} = \kappa_j \int_{\hat{\partial}_j} \mathbf{M}_j^T(\mathbf{r}') \mathbf{E}_k^{\text{sc}}(\mathbf{r}') d\mathbf{r}'. \quad (2.48)$$

By applying (2.48) to (2.47), we obtain the differential contribution δR_{jk} to the j -th sensor response

$$\delta R_{jk} = \kappa_j \int_{\hat{\partial}_j} \mathbf{M}_j^T(\mathbf{r}') \delta \mathbf{E}_k^{\text{sc}}(\mathbf{r}') d\mathbf{r}' = -\kappa_j k_0^2 \Delta \varepsilon_{\text{OUT}}(\mathbf{r}) d\mathbf{r} \left[\int_{\hat{\partial}_j} \mathbf{M}_j^T(\mathbf{r}') \bar{\mathbf{G}}_b(\mathbf{r}', \mathbf{r}) d\mathbf{r}' \right] \mathbf{E}_k^{\text{tot}}(\mathbf{r}). \quad (2.49)$$

Using reciprocity, *i.e.* $\bar{\mathbf{G}}_b^T(\mathbf{r}, \mathbf{r}') = \bar{\mathbf{G}}_b(\mathbf{r}', \mathbf{r})$ and $[\bar{\mathbf{G}}_b^T(\mathbf{r}, \mathbf{r}') \mathbf{M}_j(\mathbf{r}')]^T = \mathbf{M}_j^T(\mathbf{r}') \bar{\mathbf{G}}_b(\mathbf{r}', \mathbf{r})$, we can express (2.49) as:

$$\delta R_{jk} = -\kappa_j k_0^2 \Delta \varepsilon_{\text{OUT}}(\mathbf{r}) d\mathbf{r} \left(\int_{\hat{\partial}_j} [\bar{\mathbf{G}}_b(\mathbf{r}, \mathbf{r}') \mathbf{M}_j(\mathbf{r}')]^T d\mathbf{r}' \right) \mathbf{E}_k^{\text{tot}}(\mathbf{r}). \quad (2.50)$$

We can rearrange (2.46) so that we obtain:

$$\int_{\hat{\partial}_j} \bar{\mathbf{G}}_b(\mathbf{r}, \mathbf{r}') \mathbf{M}_j(\mathbf{r}') d\mathbf{r}' = \frac{-\mathbf{E}^{\text{inc}}(\mathbf{r})}{j\omega_m \mu_0 m_j}. \quad (2.51)$$

The results in (2.50) and (2.51) allow us to express the scalar responses in term of the electric fields:

$$\delta R_{jk} = \frac{\kappa_j k_0^2 \Delta \varepsilon_{\text{OUT}}(\mathbf{r}) d\mathbf{r}}{j\omega_m \mu_0 m_j} \mathbf{E}_j^{\text{inc}}(\mathbf{r}) \cdot \mathbf{E}_k^{\text{tot}}(\mathbf{r}), \quad (2.52)$$

where $\mathbf{E}_j^{\text{inc}}$ is the field produced by the source function $\mathbf{J}(\mathbf{r}')$ of the j -th sensor. If we integrate over the entire ROI we obtain:

$$R_{jk} = -\kappa_j \frac{j\omega_m \epsilon_0}{m_j} \iiint_{V_s} \Delta \mathcal{E}_{\text{OUT}}(\mathbf{r}) \mathbf{E}_j^{\text{inc}}(\mathbf{r}) \cdot \mathbf{E}_k^{\text{tot}}(\mathbf{r}) d\mathbf{r}. \quad (2.53)$$

We now have a rigorous expression that relates the electric field to the measured scalar response. Also, if we know the scalar response, we are able to acquire the electric field product $\mathbf{E}_j^{\text{inc}}(\mathbf{r}) \cdot \mathbf{E}_k^{\text{tot}}(\mathbf{r})$. Note that with this expression, there is no need for approximate models for Green's function.

2.5.3 Sampling with Small Dipole Antennas

Let the j -th source's current distribution in Tx mode be

$$\mathbf{J}_j(\mathbf{r}') = J_j \Delta \Omega_j \delta^3(\mathbf{r}_j - \mathbf{r}') \hat{\mathbf{p}}_j, \quad (2.54)$$

where $m_j = J_j \Delta \Omega_j$, $\mathbf{M}(\mathbf{r}') = \delta^3(\mathbf{r}_j - \mathbf{r}') \hat{\mathbf{p}}_j$ and $\delta^3(\mathbf{r}_j - \mathbf{r}')$ is the 3D Dirac delta function, $\hat{\mathbf{p}}_j$ is the polarization unit vector, J_j is the current distribution and $\Delta \Omega_j$ is the source volume.

The same sensor in Rx mode has a scalar response expressed as

$$R_{jk} = \iiint_{V_s} \delta^3(\mathbf{r}_j - \mathbf{r}) \hat{\mathbf{p}}_j \cdot \mathbf{E}_k^{\text{sc}}(\mathbf{r}) d\mathbf{r} = \hat{\mathbf{p}}_j \cdot \mathbf{E}_k^{\text{sc}}(\mathbf{r}_j), \quad (2.55)$$

which implies that the scalar response can be directly related to the electric field

$$\hat{\mathbf{p}}_j \cdot \mathbf{E}_k^{\text{sc}}(\mathbf{r}_j) = \frac{-k_0^2}{j\omega_m \mu_0 J_j \Delta \Omega_j} \iiint_{V_s} \Delta \mathcal{E}_{\text{OUT}}(\mathbf{r}) \mathbf{E}_j^{\text{inc}}(\mathbf{r}) \cdot \mathbf{E}_k^{\text{tot}}(\mathbf{r}) d\mathbf{r}. \quad (2.56)$$

It is worth noting that the above equation leads to the sensitivity expression for the transmission coefficient [15]

$$T_{jk} = \mathbf{E}_k^{\text{inc}} \cdot \hat{\mathbf{p}}_j, \quad (2.57)$$

with respect to the permittivity of a voxel. As proven in [15], if the scattered field \mathbf{E}_k^{sc} is viewed as a variation of $\mathbf{E}_k^{\text{inc}}$ when the permittivity of a single voxel is perturbed by $\Delta\varepsilon_{\text{OUT}}(\mathbf{r})$, we obtain

$$\frac{dT_{jk}}{d\varepsilon} = \lim_{\Delta\varepsilon_{\text{OUT}} \rightarrow 0} \frac{R_{jk}}{\Delta\varepsilon_{\text{OUT},p}} = \frac{-k_0^2 \Delta\Omega_p}{j\omega_m \mu_0 J_j \Delta\Omega_j} \mathbf{E}_j^{\text{inc}}(\mathbf{r}) \cdot \mathbf{E}_k^{\text{inc}}(\mathbf{r}). \quad (2.58)$$

This result would be obtained from (2.56) as well, if the scattered field is due to a small scatterer of volume $\Delta\Omega_p$ at a voxel p with contrast $\Delta\varepsilon_{\text{OUT},p}$, where both $\Delta\Omega_p \rightarrow 0$ and $\Delta\varepsilon_{\text{OUT},p} \rightarrow 0$, which allows us to use the linear Born approximation to substitute $\mathbf{E}_k^{\text{tot}}(\mathbf{r}) \approx \mathbf{E}_k^{\text{inc}}(\mathbf{r})$.

2.5.4 Scalar Responses in the Form of Scattering Parameters

By definition, the S -parameters are [16]

$$S_{jk} = \frac{b_j}{a_k}, \quad (2.59)$$

where b_j is the outgoing root-power wave at the j -th port and a_k is the incoming root-power wave at the k -th port. The root-power waves (or power waves) relate to the field at a port through the modal vectors (as defined in [16])

$$b_j = \iint_{S_j} (\mathbf{E}_j \times \mathbf{h}_j) \cdot \hat{\mathbf{k}}_j dS = \iint_{S_j} (\mathbf{e}_j \times \mathbf{H}_j) \cdot \hat{\mathbf{k}}_j dS, \quad (2.60)$$

$$a_k = \iint_{S_k} (\mathbf{E}_k \times \mathbf{h}_k) \cdot \hat{\mathbf{k}}_k dS = \iint_{S_k} (\mathbf{e}_k \times \mathbf{H}_k) \cdot \hat{\mathbf{k}}_k dS, \quad (2.61)$$

where \mathbf{e}_ξ and \mathbf{h}_ξ ($\xi = j, k$) are the ξ -th port modal vectors while $\hat{\mathbf{k}}_\xi$ is its unit vector indicating the direction of propagation. (inward for a_k and outward for b_j).

In order to apply (2.53) to the case of S -parameters, we need to find the source strength m_j and its physical meaning. Let the j -th port excite the sensor j , which operates as a transmitter.

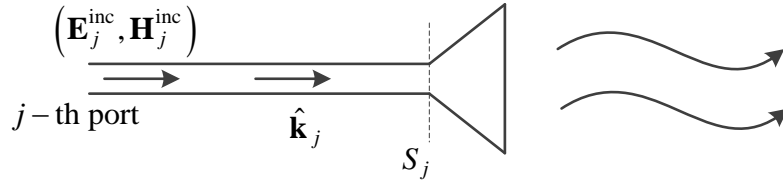


Figure 2.3 The j -th antenna in Tx mode.

The transmission line guides the wave $(\mathbf{E}_j^{\text{inc}}, \mathbf{H}_j^{\text{inc}})$ to the antenna. Applying the equivalence principle [17], the incident wave can be replaced at the port cross-section S_j by equivalent electric surface currents:

$$\mathbf{J}_j = 2\hat{\mathbf{k}}_j \times \mathbf{H}_j^{\text{inc}} = m_j \mathbf{M}_j. \quad (2.62)$$

Here, Love's equivalence principle and image theory are employed at the surface S_j where a magnetic wall is placed [17].

The incident power wave at the j -th port is [16]

$$a_j = \iint_{S_j} (\mathbf{e}_j \times \mathbf{H}_j^{\text{inc}}) \cdot \hat{\mathbf{k}}_j dS = \iint_{S_j} \mathbf{e}_j \cdot (\mathbf{H}_j^{\text{inc}} \times \hat{\mathbf{k}}_j) dS. \quad (2.63)$$

For a given mode, let $\mathbf{H}_j^{\text{inc}} = H\mathbf{h}_j$ such that (2.63) can be expressed as [16]

$$a_j = H \iint_{S_j} (\mathbf{e}_j \times \mathbf{h}_j) \cdot \hat{\mathbf{k}}_j dS = H. \quad (2.64)$$

since the orthonormal property of modal vectors \mathbf{e}_j and \mathbf{h}_j is employed [16]

$$\iint_{S_j} (\mathbf{e}_j \times \mathbf{h}_j) \cdot \hat{\mathbf{k}}_j dS = 1. \quad (2.65)$$

Therefore,

$$\mathbf{H}_j^{\text{inc}} = a_j \mathbf{h}_j. \quad (2.66)$$

This relation is substituted in (2.62):

$$2(\hat{\mathbf{k}}_j \times \mathbf{H}_j^{\text{inc}}) = 2(\hat{\mathbf{k}}_j \times a_j \mathbf{h}_j) = 2a_j (\hat{\mathbf{k}}_j \times \mathbf{h}_j) = m_j \mathbf{M}_j. \quad (2.67)$$

We now consider the same sensor shown in Figure 2.3 in a receiving arrangement; see Figure 2.4.

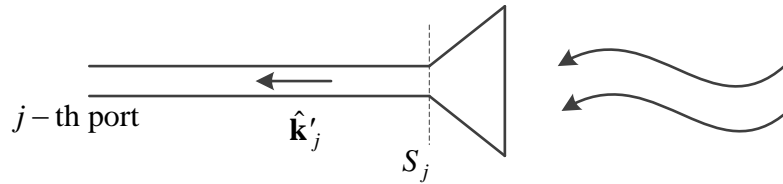


Figure 2.4 The j -th antenna in Rx mode.

The outgoing power wave is defined as [16]

$$b_j = \iint_{S_i} \hat{\mathbf{k}}'_j \cdot (\mathbf{E}_j \times \mathbf{h}_j) dS = \iint_{S_i} \mathbf{E}_j \cdot (\mathbf{h}_j \times (-\hat{\mathbf{k}}'_j)) dS, \quad (2.68)$$

where $\hat{\mathbf{k}}'_j = -\hat{\mathbf{k}}_j$. Therefore,

$$b_j = \iint_{S_i} \mathbf{E}_j \cdot \mathbf{M}_j dS, \quad (2.69)$$

where

$$\mathbf{M}_j = \hat{\mathbf{k}}_j \times \mathbf{h}_j. \quad (2.70)$$

From (2.67) and (2.70), it follows that

$$m_j = 2a_j. \quad (2.71)$$

From (2.53), (2.59) and (2.71) we can express the S -parameters due to the scattered field as

$$S_{jk}^{\text{sc}} = \frac{b_j}{a_k} = \frac{j\omega_m \epsilon_0}{2a_j a_k} \iiint_{V_S} \Delta \epsilon_{\text{OUT}}(\mathbf{r}) \mathbf{E}_j^{\text{inc}}(\mathbf{r}) \cdot \mathbf{E}_k^{\text{tot}}(\mathbf{r}) d\mathbf{r}. \quad (2.72)$$

This relationship is the forward model of scattering in terms of S -parameters. In experiments and simulations this is critical since these are the quantities that can be measured.

2.6 Point-Spread Functions

The work in [6] shows that the field product $\mathbf{E}_j^{\text{inc}}(\mathbf{r}) \cdot \mathbf{E}_k^{\text{tot}}(\mathbf{r})$ can be determined by measuring the system PSF from a known small scatterer (CO). This allows us to express (2.72) as [6]

$$\Delta S_{\text{CO},jk}^{(\mathbf{r})}(\mathbf{r}_j, \omega_m) \approx \frac{j\omega_m \epsilon_0}{2a_j a_k} \Delta \epsilon_{\text{CO}}(\mathbf{r}) \left[\mathbf{E}_j^{\text{inc}}(\mathbf{r}) \cdot \mathbf{E}_k^{\text{tot}}(\mathbf{r}) \right] \Delta \Omega_{\text{CO},p}. \quad (2.73)$$

We can rearrange (2.73) to obtain the product of the incident and total fields [6]

$$\left[\mathbf{E}_j^{\text{inc}}(\mathbf{r}) \cdot \mathbf{E}_k^{\text{tot}}(\mathbf{r}) \right] \approx \frac{\Delta S_{\text{CO},jk}^{(\mathbf{r})}(\mathbf{r}_j, \omega_m)}{C}, \quad (2.74)$$

where

$$C = \frac{j\omega_m \epsilon_0}{2a_j a_k} \Delta \epsilon_{\text{CO}}(\mathbf{r}) \Delta \Omega_{\text{CO},p}. \quad (2.75)$$

This relation is important since it allows us to extract the incident field and Green's function product directly without making an approximate model or using a computationally expensive simulation. The equation (2.74) can be substituted into (2.72) for the case when the OUT is being scanned [6]:

$$\begin{aligned} \Delta S_{\text{OUT},jk}(\mathbf{r}_j, \omega_m) &= \frac{j\omega_m \epsilon_0}{2a_j a_k} \iiint_V \Delta \epsilon_{\text{OUT}}(\mathbf{r}) \frac{\Delta S_{\text{CO},jk}^{(\mathbf{r})}(\mathbf{r}_j, \omega_m)}{C} d\mathbf{r}, \\ &= \frac{1}{\Delta \Omega_{\text{CO},p}} \iiint_V \frac{\Delta \epsilon_{\text{OUT}}(\mathbf{r})}{\Delta \epsilon_{\text{CO}}(\mathbf{r})} \Delta S_{\text{CO},jk}^{(\mathbf{r})}(\mathbf{r}_j, \omega_m) d\mathbf{r}. \end{aligned} \quad (2.76)$$

Since the S -parameters associated with the PSF are translationally invariant in a homogenous and layered medium, (2.76) can be expressed as [6]

$$\Delta S_{\text{OUT},jk}(\mathbf{r}_j, \omega_m) = \frac{1}{\Delta \Omega_{\text{CO},p}} \iiint_V \frac{\Delta \varepsilon_{\text{OUT}}(\mathbf{r})}{\Delta \varepsilon_{\text{CO}}(\mathbf{r})} \Delta S_{\text{CO},jk}^{(\mathbf{r})}(\mathbf{r}_j - \mathbf{r}, \omega_m) d\mathbf{r}. \quad (2.77)$$

This result is critical since it relates the S -parameters of CO and OUT to the contrast function.

2.7 An Extension of Born's Approximation

It is crucial that our method does not rely on the linear Born approximation since this approximation has significant limitations on the size and contrast of the targets. To overcome these limitations, Habashy *et al.* [18] provided a method to overcome partially these constraints. According to [18], if the region that we are observing is small in comparison to the wavelength of the incident wave, the total internal electric field of OBJ can be related to the RO (where $\mathbf{E}^{\text{inc}}(\mathbf{r}) = \mathbf{E}_{\text{RO}}(\mathbf{r})$) field by a tensor

$$\mathbf{E}_{\text{OBJ}}^{\text{tot}}(\mathbf{r}) \approx \bar{\Gamma}_{\text{OBJ}} \cdot \mathbf{E}_{\text{RO}}(\mathbf{r}), \quad (2.78)$$

which agrees with the localized nonlinear (LN) and the quasi-analytic (QA) approximations [19]-[21]. The tensor, $\bar{\Gamma}_{\text{OBJ}}$, is based on the permittivity contrast and size of the small target [18]. If the DC limit proposed in [18] is satisfied, $\bar{\Gamma}_{\text{OBJ}} \rightarrow \Gamma_{\text{OBJ}} \bar{\mathbf{I}}$, where the scalar value, Γ_{OBJ} , is based on the permittivity of the RO and OBJ:

$$\Gamma_{\text{OBJ}}(\mathbf{r}) \approx \frac{3\varepsilon_{\text{RO}}}{\varepsilon_{\text{OBJ}}(\mathbf{r}) + 2\varepsilon_{\text{RO}}}. \quad (2.79)$$

We can, therefore, express the result in (2.72) for the case when $\text{OBJ} \equiv \text{OUT}$ in terms of the findings in [1] and [18] as

$$\Delta S_{\text{OUT},jk} = \frac{j\omega_m \varepsilon_0}{2a_j a_k} \iiint_{V_S} \Delta \varepsilon_{\text{OUT}}(\mathbf{r}) \mathbf{E}_{\text{RO},j}(\mathbf{r}) \cdot \Gamma_{\text{OUT}}(\mathbf{r}) \mathbf{E}_{\text{RO},k}(\mathbf{r}) d\mathbf{r}. \quad (2.80)$$

This approximation also applies for the case of a small scatterer [1], [6], in which case

$$\Delta S_{\text{CO},jk}^{(\mathbf{r})}(\mathbf{r}_j, \omega_m) \approx \frac{j\omega_m \varepsilon_0}{2a_j a_k} \Delta \varepsilon_{\text{CO}}(\mathbf{r}) \left[\mathbf{E}_{\text{RO},j}(\mathbf{r}) \cdot \Gamma_{\text{CO}} \mathbf{E}_{\text{RO},k}(\mathbf{r}) \right] \Delta \Omega_{\text{CO},p}. \quad (2.81)$$

This allows us to express (2.77) in terms of the LN and QA approximations as [1], [6], [7], [18]–[21]:

$$\Delta S_{\text{OUT},jk}(\mathbf{r}_j, \omega_m) = \frac{1}{\Delta \Omega_{\text{CO},p}} \iiint_V \frac{\Delta \varepsilon_{\text{OUT}}(\mathbf{r})}{\Delta \varepsilon_{\text{CO}}(\mathbf{r})} \frac{\Gamma_{\text{OUT}}(\mathbf{r})}{\Gamma_{\text{CO}}} \Delta S_{\text{CO},jk}^{(\mathbf{r})}(\mathbf{r}_j - \mathbf{r}, \omega_m) d\mathbf{r}. \quad (2.82)$$

The significance of this relation and the impact of the ratio $\Gamma_{\text{OUT}}/\Gamma_{\text{CO}}$ is investigated in the subsequent chapters.

2.8 Discretizing the Region of Interest into Voxels

In order to analyze the system voxel-by-voxel and ensure that the voxels are small enough to satisfy the DC limit in [18], we need to define a new coordinate system. The vector \mathbf{r}_p shown in Figure 2.5 represents the coordinate of the voxel of interest ($p = 1, \dots, N_v$ and $N_v = N_x N_y N_z$). The permittivity contrast of the CO at voxel p can be defined as [7], [12]

$$\Delta\epsilon_{\text{CO}}(\mathbf{r}) = \begin{cases} \delta\epsilon_{\text{CO},p} \neq 0, & \mathbf{r} = \mathbf{r}_p \\ 0, & \mathbf{r} \neq \mathbf{r}_p. \end{cases} \quad (2.83)$$

Since the permittivity contrast is the same at every p -th voxel in the ROI, we refer to $\delta\epsilon_{\text{CO},p}$ as $\delta\epsilon_{\text{CO}}$ [7], [12].

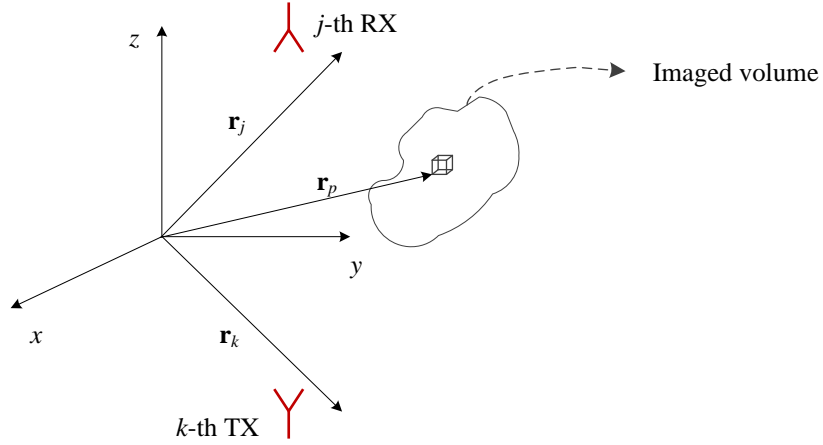


Figure 2.5 Illustration of the position vectors of the voxel of interest, the receiving (Rx) antenna, and the transmitting (Tx) antenna.

Likewise, the above relationship allows us to express the calibrated S -parameters for the OUT as [7], [12]

$$\Delta S_{\text{OUT},jk}(\mathbf{r}_j) \approx \iiint_V \frac{\Delta S_{\text{CO},p,jk}(\mathbf{r}_j)}{\Delta \Omega_{\text{CO},p} \delta\epsilon_{\text{CO}}} \frac{\Gamma_{\text{OUT}}(\mathbf{r})}{\Gamma_{\text{CO}}} \Delta \epsilon_{\text{OUT}}(\mathbf{r}) d\mathbf{r}, \quad (2.84)$$

where $\Delta S_{\text{CO},p,jk}(\mathbf{r}_j) = \Delta S_{\text{CO},jk}^{(\mathbf{r}_p)}(\mathbf{r}_j)$ is the S -parameter due to the scattered field at voxel p .

Since $\Delta S_{\text{CO},p,jk}(\mathbf{r}_j)$ is directly proportional to the product of Green's function and the incident field, it is also translationally invariant [8]. As such, (2.84) then becomes [7], [12]

$$\begin{aligned}\Delta S_{\text{OUT},jk}(\mathbf{r}_j) &\approx \frac{1}{\Delta x \Delta y \Delta z} \iiint_V \frac{\Delta S_{\text{CO},p,jk}(\mathbf{r}_j - \mathbf{r})}{\delta \varepsilon_{\text{CO}}} \frac{\Gamma_{\text{OUT}}(\mathbf{r})}{\Gamma_{\text{CO}}} \Delta \varepsilon_{\text{OUT}}(\mathbf{r}) d\mathbf{r}, \\ \Delta S_{\text{OUT},q}(\mathbf{r}_j) &\approx \frac{1}{\Delta x \Delta y \Delta z} \iiint_V f_{\text{OUT}}(\mathbf{r}) K_q(\mathbf{r}_j - \mathbf{r}; \omega_m) dx dy dz,\end{aligned}\quad (2.85)$$

where $f_{\text{OUT}}(\mathbf{r}) = (\Gamma_{\text{OUT}}(\mathbf{r}) \Delta \varepsilon_{\text{OUT}}(\mathbf{r})) / (\delta \varepsilon_{\text{CO}} \Gamma_{\text{CO}})$ is the permittivity function that is to be reconstructed and $K_q(\mathbf{r}_j - \mathbf{r}; \omega_m) = \Delta S_{\text{CO},p,q}(\mathbf{r}_j - \mathbf{r}; \omega_m)$ is the translationally invariant kernel [3], [4], [6]–[8], [10]–[12]. Since the formation of the system of equations is similar to what was presented in chapter 2.4.6 we reintroduce subscript q as the index number of the S -parameter ($q = 1, \dots, N_s$).

The integration in (2.85) over z is replaced by a summation since the algorithm is performed over N_z layers with $N_z \in \mathbb{Z}$ [4], [6]–[8], [10]–[12]:

$$\begin{aligned}\Delta S_{\text{OUT},q}(\mathbf{r}', \omega_m) \\ \approx \frac{1}{\Delta x \Delta y \Delta z} \sum_{n=1}^{N_z} \Delta z_n \int_x \int_y f_{\text{OUT}}(x, y, z_n) K_q(x' - x, y' - y, \bar{z} - z_n; \omega_m) dx dy.\end{aligned}\quad (2.86)$$

The integral equation (2.86) can be viewed as a convolution [4], [6], [8], [10], [11]:

$$\Delta \tilde{S}_{\text{OUT},q}(k_x, k_y, \bar{z}, \omega_m) \approx \sum_{n=1}^{N_z} \tilde{F}_{\text{OUT}}(k_x, k_y, z_n) \tilde{K}_q(k_x, k_y, \bar{z} - z_n, \omega_m). \quad (2.87)$$

The constants in the integral are ignored since qualitative imaging normalizes the result. This relationship can be formed into a system of equations similar to (2.31). The difference here is the kernel \tilde{K}_q is derived experimentally using a CO shift.

2.9 Conclusions

The evolution of the near-field microwave holography method developed by our team has roots in the far-field method proposed first in [2]. Improvements on this model to make it applicable to the near-field region began in [3] by making assumptions for Green's function. The findings in [6] improve the model by eliminating the need for the crude assumptions made in [3], [4], [10] and [11] and the computational cost associated with simulating the antennas [22]. This is achieved by an experimental derivation of the system PSF.

The work presented in this chapter serves as a foundation for the quantitative holographic reconstruction method, which is the main contribution of this thesis.

References

- [1] N.K. Nikolova, private communication.
- [2] D.M. Sheen, D.L McMackin, and T.E. Hall, "Three-dimensional millimeter-wave imaging for concealed weapon detection," *IEEE Trans. Microwav. Theory Tech.*, vol. 49, no. 9, pp. 1581-1592, Sept. 2001.

- [3] M. Ravan, R.K. Amineh, and N.K. Nikolova, "Two-dimensional near-field microwave holography," *Inverse Problems*, vol. 26, no. 5, 0555011 (21 pp.), May 2010.
- [4] R.K. Amineh, M. Ravan, A. Khalatpour, and N.K. Nikolova, "Three-dimensional near-field microwave holography using reflected and transmitted signals," *IEEE Trans. Antennas Propag.*, vol. 59, no. 12, pp. 4777-4789, Dec. 2012.
- [5] FEKO suite 6.2, EM Software & System, Inc. USA, <http://www.feko.com>.
- [6] R.K. Amineh, J.J. McCombe, A. Khalatpour, and N.K. Nikolova, "Microwave holography using point-spread functions measured with calibration objects," *IEEE Trans. on Instrum. Meas.*, vol. 64, no. 2, pp. 403-417, Feb. 2015.
- [7] S. Tu, "Fast quantitative microwave imaging based on calibration measurements," Ph.D. Dissertation, Dept. Elect. and Comp. Eng., McMaster Univ., 2015.
- [8] J.R. Thompson, J.J. McCombe, S. Tu, and N.K. Nikolova, "Quantitative imaging of dielectric objects based on holographic reconstruction," *Radar Conf. (RadarCon), 2015 IEEE*, pp. 0679-0683, 10–15 May 2015.
- [9] W. Chew 1995 *Waves and Fields in Inhomogeneous Media* Piscataway, NJ: IEEE Press.
- [10] R.K. Amineh, A. Khalatpour, H. Xu, Y. Baskharoun, and N.K. Nikolova, "Three-dimensional near-field microwave holography for tissue imaging," *Int. J. Biomed. Imag.*, vol. 2012, Art. 291494 (11 pp.) , Dec. 2012.

- [11]R.K. Amineh, M. Ravan, J. McCombe, and N.K. Nikolova. “Three-dimensional microwave holographic imaging employing forward-scattered waves only,” *Int. J. Antennas Propag.*, vol. 2013, Article ID 897287 (15 pp.), Feb. 2013.
- [12]S. Tu, J.J. McCombe, D.S. Shumakov, and N.K. Nikolova, “Fast quantitative microwave imaging with resolvent kernel extracted from measurements,” *Inverse Problems*, vol. 31, no. 4, 045007 (33 pp.), April 2015.
- [13]The Mathworks, MATLAB, Natick, MA, USA, 2012, <http://www.themathworks.com>
- [14]M.S. Salazar-Palma, T.K. Sarkar, L. Garica-Castillo, T. Roy, and A. Djordjevic, *Iterative and Self-Adaptive Finite-Elements in Electromagnetic Modeling*, Norwood, MA: Artech House, Inc. 1998.
- [15]L. Liu, A. Trehan, and N.K. Nikolova, “Near-field detection at microwave frequencies based on self-adjoint sensitivity analysis,” *Inverse Problems*, vol. 26, 105001, 2010.
- [16]D. Pozar, *Microwave Engineering*, John Wiley & Sons, Inc., 2005.
- [17]C. Balanis, *Advanced Engineering Electromagnetics*, 2nd ed., Hoboken, NJ: John Wiley and Sons, 2012.
- [18]T.M. Habashy, R.W. Groom, and B.R. Spies, “Beyond the Born and Rytov approximations: a nonlinear approach to electromagnetic scattering,” *J. Geophys. Res.*, vol. 98, no. B2, pp. 1759-1775, Feb. 1993.
- [19]M.S. Zhdanov and S Fang, “Quasi-linear approximation in 3D EM modelling,” *Geophysics*, vol. 61, no. 5, pp. 646-665, Jun. 1996.

- [20] M.S. Zhdanov and S Fang, "3D EM quasi-linear EM inversion," *Radio Sci.*, vol. 31, no. 4, pp. 741-754, Jul. 1996.
- [21] M.S. Zhdanov and S Fang, "3D EM electromagnetic inversion based on quasi-analytical approximation," *Inverse Problems*, vol. 16, no. 5, pp. 1297-1322, Oct. 2000.
- [22] R.K. Amineh, A. Khalatpour, H. Xu, Y. Baskharoun, and N.K. Nikolova, "Three-dimensional near-field microwave holography for tissue imaging," *Int. J. Biomed. Imag.*, vol. 2012, Art. 291494 (11 pp.), Dec. 2012.

Chapter 3

Quantitative Global Spectral Inversion

3.1 Introduction

This chapter builds on the previously derived concepts and demonstrates the implementation of the Fourier transform (FT) and the least-squares (LS) method in the solution of the inverse problem and is the first method proposed by the author to reconstruct the permittivity distribution of dielectric targets in the near-field region using a microwave holography technique. The method presented in this chapter solves the inverse problem through a linear system of equations and allows for imposing physically-based constraints. The importance of imposing such constraints is investigated.

Assumptions are made to simplify the nonlinearities of the problem into a linear system of equations with linear constraints. This is an important feature since there are a plethora of LS solvers to choose from. The software used in this chapter requires both the constraints and the system of equations to be linear. Some systems of equation solvers are capable of handling non-linear constraints; however, this tends to decelerate the runtime of the code, which makes the technique no longer quasi-real-time.

The image reconstruction example presented in this chapter, which has been published in [1], consists of an object under test (OUT) with relative permittivity $1.2-j0$, where

$j = \sqrt{-1}$. The calibration object (CO) used in this example is a small dielectric cube with relative permittivity $1.1-j0$ that is embedded in a background medium, with relative permittivity $1-j0$.

As previously mentioned, the goal of the algorithm is to acquire the permittivity distribution, *i.e.* the real and imaginary parts of the permittivity as a function of position. All permittivities referred to hereafter are complex relative permittivities defined as

$$\varepsilon_{\text{OBJ}}(\mathbf{r}) = \varepsilon'_{\text{OBJ}}(\mathbf{r}) + j\varepsilon''_{\text{OBJ}}(\mathbf{r}), \quad (3.1)$$

where $\text{OBJ} \equiv \text{CO}, \text{OUT}, \text{RO}$. When reconstructing $\varepsilon_{\text{OBJ}}(\mathbf{r})$, we must keep in mind that its real part must be greater than or equal to one and the imaginary part must be less than or equal to zero.

3.2 Relating the Point-Spread Function to the Desired Response

As explained in [2], if multiple scattering is ignored, the scattering response can be viewed as a weighted combination of the scattering contributions of known point scatterers integrated over some region of interest (ROI), $V \in \mathbb{R}^3$

$$\Delta S_{\text{OUT},q}(\mathbf{r}', \omega_m) \approx \iiint_V \frac{\tau(\mathbf{r})}{\delta v} \Delta S_{\text{CO},q}^{(\mathbf{r})}(\mathbf{r}', \omega_m) d\mathbf{r}, \quad (3.2)$$

where $\mathbf{r} = (x, y, z)$ is the position of the voxel, $\mathbf{r}' = (x', y', \bar{z})$ are the coordinates of the scanning aperture, q is the index of the scattering parameters ($q = 1, \dots, N_s$), δv is the

volume of the small scatterer, ω_m is the angular frequency ($m = 1, \dots, N_\omega$), $\Delta S_{\text{CO},q}^{(\mathbf{r})}(\mathbf{r}', \omega_m)$ is the scattering response of the CO when the small scatterer is at voxel \mathbf{r} and $\tau(\mathbf{r})$ is the distribution weighting factor [2]

$$\tau(\mathbf{r}) = \frac{\Delta \varepsilon_{\text{OUT}}(\mathbf{r})}{\delta \varepsilon_{\text{CO}}} \frac{\Gamma_{\text{OUT}}(\mathbf{r})}{\Gamma_{\text{CO}}}. \quad (3.3)$$

Here [2],

$$\Gamma_{\text{OBJ}}(\mathbf{r}) = \frac{3\varepsilon_{\text{RO}}}{\varepsilon_{\text{OBJ}}(\mathbf{r}) + 2\varepsilon_{\text{RO}}}, \quad (3.4)$$

and

$$\frac{\Gamma_{\text{OUT}}(\mathbf{r})}{\Gamma_{\text{CO}}} \approx \frac{\varepsilon_{\text{CO}} + 2\varepsilon_{\text{RO}}}{\varepsilon_{\text{OUT}}(\mathbf{r}) + 2\varepsilon_{\text{RO}}}, \quad (3.5)$$

where ε_{CO} is the permittivity of the small scatterer in the CO, ε_{RO} is the permittivity of the background medium and $\varepsilon_{\text{OUT}}(\mathbf{r})$ is the permittivity distribution of the OUT. We refer to the ratio (3.5) throughout this thesis as the gamma factor (GF).

It is worth mentioning that when the CO and the OUT have permittivities that are close to one another, $\varepsilon_{\text{OUT}}(\mathbf{r}) \approx \varepsilon_{\text{CO}}$, then the GF is approximately one, $\Gamma_{\text{OUT}}(\mathbf{r}) / \Gamma_{\text{CO}} \approx 1$. This approximation allows us to linearize the forward model and the associated constraints.

In the implemented reconstruction algorithm, the integral equation (3.2) yields a summation [1], [2]

$$\Delta S_{\text{OUT},q}(\mathbf{r}', \omega_m) = \sum_{p=1}^{N_v} \tau(\mathbf{r}_p) \Delta S_{\text{CO},q}^{(\mathbf{r}_p)}(\mathbf{r}', \omega_m) = \sum_{p=1}^{N_v} \tau_p \Delta S_{\text{CO},q,p}(\mathbf{r}', \omega_m), \quad (3.6)$$

where \mathbf{r}_p ($p=1, \dots, N_v$) is the position of the voxel. We apply the FT to the x' and y' coordinates, respectively, to obtain the linear relationship in Fourier space [1], which forms the basis for the global spectral inversion (GSI) method [1]

$$\Delta\tilde{\mathcal{S}}_{\text{OUT},q}(k_x, k_y, \bar{z}, \omega_m) = \sum_{p=1}^{N_v} \tau_p \Delta\tilde{\mathcal{S}}_{\text{CO},q,p}(k_x, k_y, \bar{z}, \omega_m), \quad (3.7)$$

where the Fourier variable pair is $\boldsymbol{\kappa} = (k_x, k_y)$, k_x is the FT of x' and k_y is the FT of y' . Like the permittivity distribution, we assume that the distribution weighting factor is frequency independent. This allows the relation (3.7) to be expressed in matrix form as [1]

$$\begin{bmatrix} \Delta\tilde{\mathcal{S}}_{\text{OUT},1}(\boldsymbol{\kappa}, \omega_m) \\ \vdots \\ \Delta\tilde{\mathcal{S}}_{\text{OUT},N_s}(\boldsymbol{\kappa}, \omega_m) \end{bmatrix} = \begin{bmatrix} \Delta\tilde{\mathcal{S}}_{\text{CO},1,1}(\boldsymbol{\kappa}, \omega_m) & \cdots & \Delta\tilde{\mathcal{S}}_{\text{CO},1,N_v}(\boldsymbol{\kappa}, \omega_m) \\ \vdots & \ddots & \vdots \\ \Delta\tilde{\mathcal{S}}_{\text{CO},N_s,1}(\boldsymbol{\kappa}, \omega_m) & \cdots & \Delta\tilde{\mathcal{S}}_{\text{CO},N_s,N_v}(\boldsymbol{\kappa}, \omega_m) \end{bmatrix} \begin{bmatrix} \tau_1 \\ \vdots \\ \tau_{N_v} \end{bmatrix}. \quad (3.8)$$

Next, we build a system of equations that includes the data from all angular frequencies. This is done in a manner similar to the procedure used to obtain the system (2.31).

Let us denote a column in the system matrix of (3.8) as [1]

$$\Delta\tilde{\mathcal{S}}_{\text{CO},p}(\boldsymbol{\kappa}, \omega_m) = \left[\Delta\tilde{\mathcal{S}}_{\text{CO},1,p}(\boldsymbol{\kappa}, \omega_m) \quad \cdots \quad \Delta\tilde{\mathcal{S}}_{\text{CO},N_s,p}(\boldsymbol{\kappa}, \omega_m) \right]^T. \quad (3.9)$$

We then create a system matrix which is composed of the column vectors at every angular frequency [1]:

$$\underline{\tilde{\mathcal{S}}}_{\text{CO},p}(\boldsymbol{\kappa}) = \left[\Delta\tilde{\mathcal{S}}_{\text{CO},p}^T(\boldsymbol{\kappa}, \omega_1) \quad \cdots \quad \Delta\tilde{\mathcal{S}}_{\text{CO},p}^T(\boldsymbol{\kappa}, \omega_{N_\omega}) \right]^T. \quad (3.10)$$

The relation (3.10) can be used to express (3.8) as a linear combination [1]

$$\tilde{\underline{\mathbf{S}}}_{\text{OUT}}(\boldsymbol{\kappa}) = \sum_{p=1}^{N_v} \tau_p \tilde{\underline{\mathbf{S}}}_{\text{CO},p}(\boldsymbol{\kappa}), \quad (3.11)$$

where $\tilde{\underline{\mathbf{S}}}_{\text{OUT}}(\boldsymbol{\kappa}) = [\Delta\tilde{\underline{\mathbf{S}}}_{\text{OUT}}^T(\boldsymbol{\kappa}, \omega_1) \cdots \Delta\tilde{\underline{\mathbf{S}}}_{\text{OUT}}^T(\boldsymbol{\kappa}, \omega_{N_\omega})]^T$ is the vector of acquired responses at all N_ω angular frequencies and the elements of that vector are defined as $\Delta\tilde{\underline{\mathbf{S}}}_{\text{OUT}}(\boldsymbol{\kappa}, \omega_m) = [\Delta\tilde{\underline{\mathbf{S}}}_{\text{OUT},1}(\boldsymbol{\kappa}, \omega_m) \cdots \Delta\tilde{\underline{\mathbf{S}}}_{\text{OUT},N_s}(\boldsymbol{\kappa}, \omega_m)]^T$.

We can express (3.11) similar to (2.31) as a linear system of equations, which is to be solved for the permittivity function [1]:

$$\tilde{\underline{\mathbf{K}}}(\boldsymbol{\kappa}) \tilde{\underline{\mathbf{F}}}_{\text{CO},p}(\boldsymbol{\kappa}) = \tilde{\underline{\mathbf{S}}}_{\text{CO},p}(\boldsymbol{\kappa}). \quad (3.12)$$

Note that the matrix $\tilde{\underline{\mathbf{K}}}(\boldsymbol{\kappa})$ is the same as the one in (2.31). $\tilde{\underline{\mathbf{F}}}_{\text{CO},p}(\boldsymbol{\kappa})$ can be viewed as the qualitative map of the CO when the small scatterer is located at voxel p [1].

We can express (3.11) in terms of the qualitative maps by letting $\tilde{\underline{\mathbf{S}}}_{\text{OUT}}(\boldsymbol{\kappa}) = \tilde{\underline{\mathbf{K}}}(\boldsymbol{\kappa}) \tilde{\underline{\mathbf{F}}}_{\text{OUT}}(\boldsymbol{\kappa})$ [1],

$$\tilde{\underline{\mathbf{K}}}(\boldsymbol{\kappa}) \tilde{\underline{\mathbf{F}}}_{\text{OUT}}(\boldsymbol{\kappa}) = \sum_{p=1}^{N_v} \tau_p \tilde{\underline{\mathbf{S}}}_{\text{CO},p}(\boldsymbol{\kappa}). \quad (3.13)$$

By multiplying both sides of the equality in (3.13) by $\tilde{\underline{\mathbf{K}}}^+(\boldsymbol{\kappa})$ (where the + sign is the pseudoinverse operator), we can express (3.13) in terms of the qualitative maps [1],

$$\tilde{\underline{\mathbf{F}}}_{\text{OUT}}(\boldsymbol{\kappa}) = \sum_{p=1}^{N_v} \tau_p \tilde{\underline{\mathbf{F}}}_{\text{CO},p}(\boldsymbol{\kappa}). \quad (3.14)$$

We have thus arrived at a linear relationship between the qualitative maps of the OUT and the CO by allowing for a solution for the OUT. Also, this result is advantageous from a troubleshooting standpoint since we can generate the qualitative maps of the CO and OUT to ensure that the acquired data is of good quality.

3.3 Qualitative Maps for the Calibration Object

3.3.1 Generating the Qualitative Maps of the Calibration Object by a Coordinate Translation

It is important to note that our quantitative holographic reconstruction method requires the CO responses, $\tilde{\mathbf{S}}_{\text{CO},p}(\boldsymbol{\kappa})$, to be measured at every voxel of interest in the ROI. This can be done in real space by coordinate translation of the CO data measured when the small scatterer is at the centre of each reconstruction plane [1]–[5]

$$\Delta S_{\text{CO}}^{(x_p, y_p, z_n)}(x', y', \bar{z}; \omega_m) = \Delta S_{\text{CO}}^{(0,0, z_n)}(x' - x_p, y' - y_p, \bar{z}; \omega_m). \quad (3.15)$$

Figure 3.1 shows the scanning aperture for the CO measurements using coordinate translation. In order to perform coordinate translation, we require a scanning aperture of twice the length and width of the ROI for each layer [1], [2]. Coordinate translation is applicable only if the medium is homogeneous or layered [2]–[5].

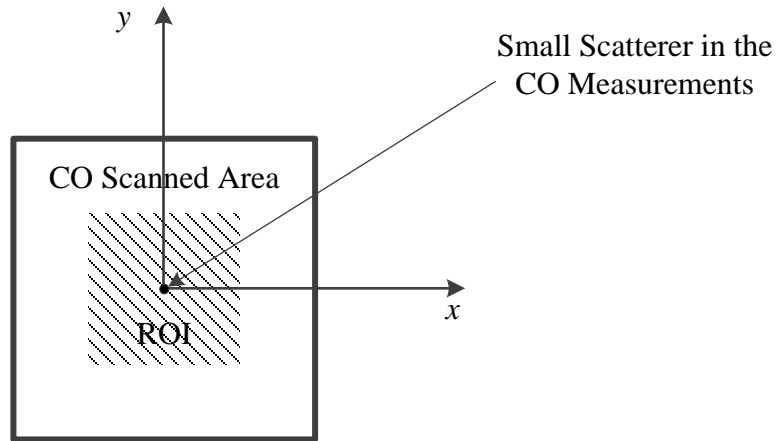


Figure 3.1 Imaged area with scatterer in the centre of the ROI and the larger CO scanned area.

To acquire the CO responses at any p -th voxel of interest, we create data sets, which extract $\frac{1}{4}$ of the scanned area. For example, if we are to acquire the CO response when the small-scatterer is at a presumed location (x_p, y_p) , we can create a new data set, which is outlined as the dashed box in Figure 3.2.

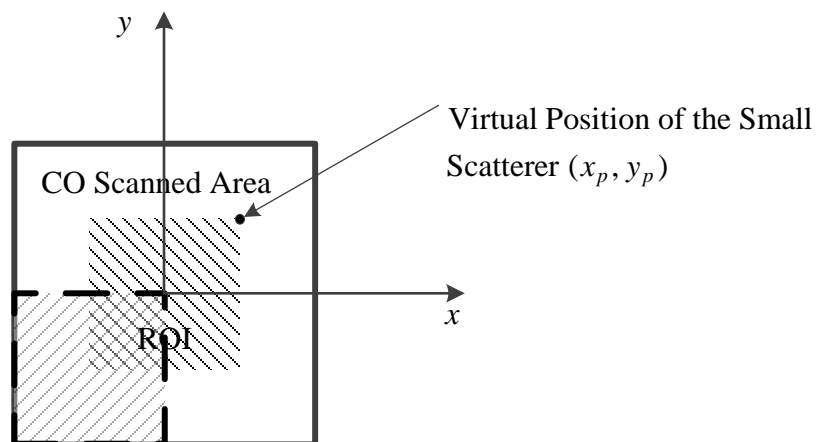


Figure 3.2 Offset imaged area where the CO data for a small-scatterer located at (x_p, y_p) is extracted as a subset of the CO measurement.

Although this method is able to produce good results, it can be cumbersome for applications where the number of voxels is large.

3.3.2 Generating the Qualitative Maps of the Calibration Object by a Fourier Shift

To determine the CO response at each location of interest (x, y, z_n) , we can instead perform a FT on the CO when it is at the centre of each $z_n \equiv \text{const.}$ layer and then use a phase shift in Fourier space [6] to perform the same task as in (3.15)

$$\begin{aligned} S(x, y, z_n) &\xrightarrow{\mathcal{F}} \tilde{S}(k_x, k_y, z_n), \\ S(x - x_p, y - y_p, z_n) &\xrightarrow{\mathcal{F}} \tilde{S}(k_x, k_y, z_n) e^{-jk_x x_p} e^{-jk_y y_p}. \end{aligned} \quad (3.16)$$

The main advantage of the translation in Fourier space is that there is no need to scan a larger area. Larger imaged areas in real space translates into better spatial-frequency resolution since $\Delta u = 1/x_m$ and $\Delta v = 1/y_m$, where x_m and y_m are defined in Figure 3.3.

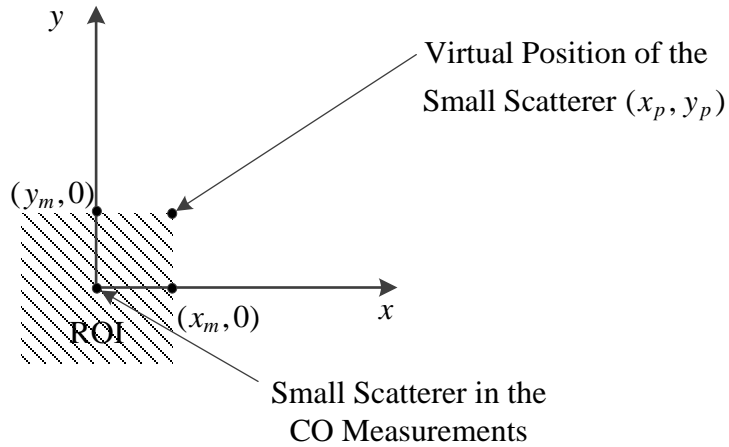


Figure 3.3 The CO scanning aperture for the Fourier shift method.

3.4 Developing a Linear System of Equations for Quantitative Imaging

Once $\tilde{\mathbf{S}}_{\text{CO},p}(\boldsymbol{\kappa})$ has been acquired, we solve (3.12) for $\tilde{\mathbf{F}}_{\text{CO},p}(\boldsymbol{\kappa})$ by applying the pseudoinverse to $\tilde{\mathbf{K}}(\boldsymbol{\kappa})$ at each $\boldsymbol{\kappa}$ pair [1],

$$\tilde{\mathbf{F}}_{\text{CO},p}(\boldsymbol{\kappa}) = \tilde{\mathbf{K}}^+(\boldsymbol{\kappa}) \tilde{\mathbf{S}}_{\text{CO},p}(\boldsymbol{\kappa}). \quad (3.17)$$

Likewise, we acquire the qualitative maps for the OUT by applying the pseudoinverse to $\tilde{\mathbf{K}}(\boldsymbol{\kappa})$ in (2.31) [3]–[5]

$$\tilde{\mathbf{F}}_{\text{OUT}}(\boldsymbol{\kappa}) = \tilde{\mathbf{K}}^+(\boldsymbol{\kappa}) \tilde{\mathbf{S}}_{\text{OUT}}(\boldsymbol{\kappa}). \quad (3.18)$$

Once the qualitative results have been computed, the linear combination in (3.14) can be expressed in terms of a linear system of equations [1]

$$\begin{bmatrix} \tilde{\mathbf{F}}_{\text{CO},1}(\boldsymbol{\kappa}; z_1) & \cdots & \tilde{\mathbf{F}}_{\text{CO},N_v}(\boldsymbol{\kappa}; z_1) \\ \vdots & \ddots & \vdots \\ \tilde{\mathbf{F}}_{\text{CO},1}(\boldsymbol{\kappa}; z_{N_z}) & \cdots & \tilde{\mathbf{F}}_{\text{CO},N_v}(\boldsymbol{\kappa}; z_{N_z}) \end{bmatrix} \begin{bmatrix} \tau_1 \\ \vdots \\ \tau_{N_v} \end{bmatrix} = \begin{bmatrix} \tilde{\mathbf{F}}_{\text{OUT}}(\boldsymbol{\kappa}; z_1) \\ \vdots \\ \tilde{\mathbf{F}}_{\text{OUT}}(\boldsymbol{\kappa}; z_{N_z}) \end{bmatrix}, \quad (3.19)$$

$$\mathbf{A}\boldsymbol{\tau} = \mathbf{b}, \quad (3.20)$$

where

$$\mathbf{A} = \begin{bmatrix} \tilde{\mathbf{F}}_{\text{CO},1}(\boldsymbol{\kappa}; z_1) & \cdots & \tilde{\mathbf{F}}_{\text{CO},N_v}(\boldsymbol{\kappa}; z_1) \\ \vdots & \ddots & \vdots \\ \tilde{\mathbf{F}}_{\text{CO},1}(\boldsymbol{\kappa}; z_{N_z}) & \cdots & \tilde{\mathbf{F}}_{\text{CO},N_v}(\boldsymbol{\kappa}; z_{N_z}) \end{bmatrix} \quad (3.21)$$

$$\boldsymbol{\tau} = [\tau_1 \quad \cdots \quad \tau_{N_v}]^T, \quad (3.22)$$

and

$$\mathbf{b} = \left[\tilde{\mathbf{F}}_{\text{OUT}}(\boldsymbol{\kappa}; z_1) \quad \cdots \quad \tilde{\mathbf{F}}_{\text{OUT}}(\boldsymbol{\kappa}; z_{N_z}) \right]^T. \quad (3.23)$$

It is demonstrated later that (3.20) can be used to reconstruct the quantitative images.

3.5 Applying Constraints to the System of Equations

We can constrain (3.20) such that the real part of the permittivity is always greater than or equal to one and the imaginary part of the permittivity is less than or equal to zero. To implement these constraints, we modify the problem such that the permittivity distribution in the OUT is the unknown vector [1], [2]

$$\mathbf{A}\boldsymbol{\varepsilon}_{\text{OUT}} = \hat{\mathbf{b}} = \mathbf{A}\boldsymbol{\varepsilon}_{\text{RO}} + \delta\varepsilon_{\text{CO}}\mathbf{b}. \quad (3.24)$$

where $\boldsymbol{\varepsilon}_{\text{OUT}} = \delta\varepsilon_{\text{CO}}\boldsymbol{\tau} + \boldsymbol{\varepsilon}_{\text{RO}}$, $\boldsymbol{\varepsilon}_{\text{RO}} = \varepsilon_{\text{RO}}\mathbf{1}_{N_v \times 1}$, $\mathbf{1}_{N_v \times 1}$ is an $N_v \times 1$ column vector of ones, the unknown vector is defined as $\boldsymbol{\varepsilon}_{\text{OUT}} = \boldsymbol{\varepsilon}'_{\text{OUT}} + j\boldsymbol{\varepsilon}''_{\text{OUT}}$, $\boldsymbol{\varepsilon}'_{\text{OUT}} = [\varepsilon'_{\text{OUT},1} \quad \cdots \quad \varepsilon'_{\text{OUT},N_v}]^T$, $\boldsymbol{\varepsilon}''_{\text{OUT}} = [\varepsilon''_{\text{OUT},1} \quad \cdots \quad \varepsilon''_{\text{OUT},N_v}]^T$ and $\boldsymbol{\tau} = (\boldsymbol{\varepsilon}_{\text{OUT}} - \boldsymbol{\varepsilon}_{\text{RO}}) / \delta\varepsilon_{\text{CO}}$.

The LS problem in (3.24) can be solved by implementing bound constraints [1], [2]

$$\begin{cases} \text{Re}\{\boldsymbol{\varepsilon}_{\text{OUT}}\} \geq 1, \\ \text{Im}\{\boldsymbol{\varepsilon}_{\text{OUT}}\} \leq 0. \end{cases} \quad (3.25)$$

Since \mathbf{A} , \mathbf{b} , $\delta\varepsilon_{\text{CO}}$, $\boldsymbol{\varepsilon}_{\text{OUT}} \in \mathbb{C}$, (3.24) needs to be decomposed into its real and imaginary parts [2],

$$(\text{Re}\{\mathbf{A}\} + j\text{Im}\{\mathbf{A}\})(\text{Re}\{\boldsymbol{\varepsilon}_{\text{OUT}}\} + j\text{Im}\{\boldsymbol{\varepsilon}_{\text{OUT}}\}) = (\text{Re}\{\hat{\mathbf{b}}\} + j\text{Im}\{\hat{\mathbf{b}}\}). \quad (3.26)$$

This yields two equations [2]

$$\begin{aligned}\operatorname{Re}\{\mathbf{A}\}\operatorname{Re}\{\boldsymbol{\varepsilon}_{\text{OUT}}\}-\operatorname{Im}\{\mathbf{A}\}\operatorname{Im}\{\boldsymbol{\varepsilon}_{\text{OUT}}\}&=\operatorname{Re}\{\hat{\mathbf{b}}\}, \\ \operatorname{Im}\{\mathbf{A}\}\operatorname{Re}\{\boldsymbol{\varepsilon}_{\text{OUT}}\}+\operatorname{Re}\{\mathbf{A}\}\operatorname{Im}\{\boldsymbol{\varepsilon}_{\text{OUT}}\}&=\operatorname{Im}\{\hat{\mathbf{b}}\}.\end{aligned}\tag{3.27}$$

The result in (3.27) can be formed into a stacked system of equations, $\mathbf{C}\mathbf{x} = \mathbf{d}$, where the stacked matrix \mathbf{C} is [2]

$$\mathbf{C}=\begin{bmatrix}\operatorname{Re}\{\mathbf{A}\} & -\operatorname{Im}\{\mathbf{A}\} \\ \operatorname{Im}\{\mathbf{A}\} & \operatorname{Re}\{\mathbf{A}\}\end{bmatrix},\tag{3.28}$$

the known vector is defined as

$$\mathbf{d}=\begin{bmatrix}\operatorname{Re}\{\hat{\mathbf{b}}\} \\ \operatorname{Im}\{\hat{\mathbf{b}}\}\end{bmatrix},\tag{3.29}$$

and the unknown vector becomes

$$\mathbf{x}=\begin{bmatrix}\operatorname{Re}\{\boldsymbol{\varepsilon}_{\text{OUT}}\} \\ \operatorname{Im}\{\boldsymbol{\varepsilon}_{\text{OUT}}\}\end{bmatrix}.\tag{3.30}$$

The values in the system of equations \mathbf{C} , \mathbf{d} , $\mathbf{x} \in \mathbb{R}$. As a result, the objective function can be defined as [1], [2]

$$\min_{\mathbf{x}}\|\mathbf{C}\mathbf{x}-\mathbf{d}\|_2^2.\tag{3.31}$$

The above relation can be solved by either using the built-in MATLAB function *lsqlin* [7] or using the software package CVX [8] along with the Mosek solver [9].

In order to determine the accuracy of the obtained image, we compute its relative root mean square error (rRMSE) [1], [2]

$$\text{rRMSE} = \sqrt{\frac{1}{N_v} \sum_{p=1}^{N_v} \left| \frac{\varepsilon_{\text{OUT}}(\mathbf{r}_p) - \bar{\varepsilon}_{\text{OUT}}(\mathbf{r}_p)}{\bar{\varepsilon}_{\text{OUT}}(\mathbf{r}_p)} \right|^2}, \quad (3.32)$$

where $\bar{\varepsilon}_{\text{OUT}}(\mathbf{r}_p)$ is the true value of the permittivity of the OUT at voxel p . In all of the quantitative examples presented in this thesis, the rRMSE is calculated.

The runtime and the rRMSE values for the quantitative reconstruction algorithm using the MATLAB solver *lsqlin* is tabulated below [1].

Table 3.1 LS solving time for *lsqlin* MATLAB command [1].

Number of Iterations	Time (minutes)	rRMSE
1662	54	0.0028
500	30	0.0029
200	11.5	0.0029
100	6.9	0.0029
50	5.3	0.0029
10	3.8	0.0029
5	3.7	0.0029

It was found that *lsqlin* was slow, even with a small number of iterations. This prompted us to find a more efficient LS solver.

CVX is a convex optimization interface with MATLAB created by a pair of mathematicians from Stanford University [8]. CVX is only capable of implementing linear constraints. The solver used with the CVX user-interface is Mosek, which uses an interior point method to solve the LS problem [9]. This software was considered to be better for this application due to the fact that it is computationally cheap in comparison. The Mosek solver reaches a solution in 18.17 seconds and in 23 iterations. This

computational saving is due to the fact that the *lsqlin* solver uses a classic optimization technique, which uses Lagrange multipliers [6], whereas the Mosek method uses disciplined convex programming [9].

The steps taken to implement this algorithm can be summarized in the following flowchart.

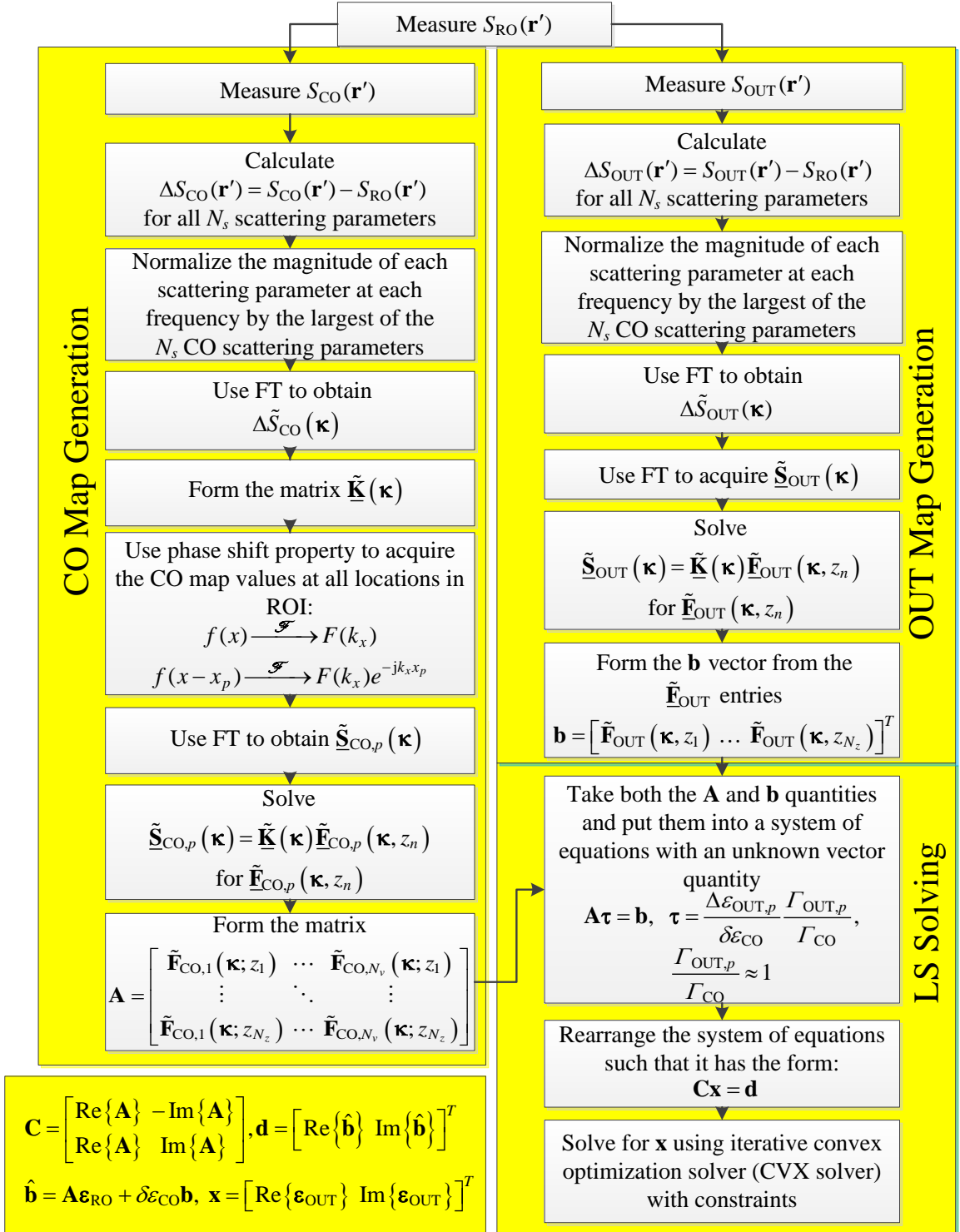


Figure 3.4 Algorithm flowchart of the constrained LS method.

3.6 Results

Since the depth resolution is $\delta_z \approx c_0 / 2B = (2.998 \times 10^8 \text{ m/s}) / 2(13 \text{ GHz}) = 11.5 \text{ mm}$, the images are reconstructed at 10 mm intervals. The target is simulated in FEKO [11] to be in the second of three layers and located 25 mm away from the transmitting antenna.

We begin this section with the qualitative results of an F-shaped target where the CO has a permittivity of $1.1-j0$ and the OUT has a permittivity of $1.2-j0$ with an RO that has a relative permittivity of $1-j0$.

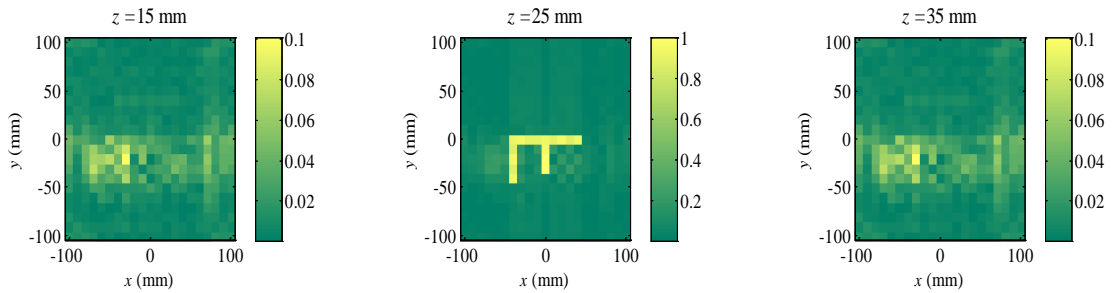


Figure 3.5 The qualitative results of the F-shaped dielectric target [10].

We then compare these results with the ϵ_{OUT} values obtained by solving (3.20) using direct inversion $\boldsymbol{\tau} = \mathbf{A}^{-1}\mathbf{b}$. This is performed in MATLAB with the *inv* command. This technique is known as the unconstrained global spectral inversion (UGSI) method.

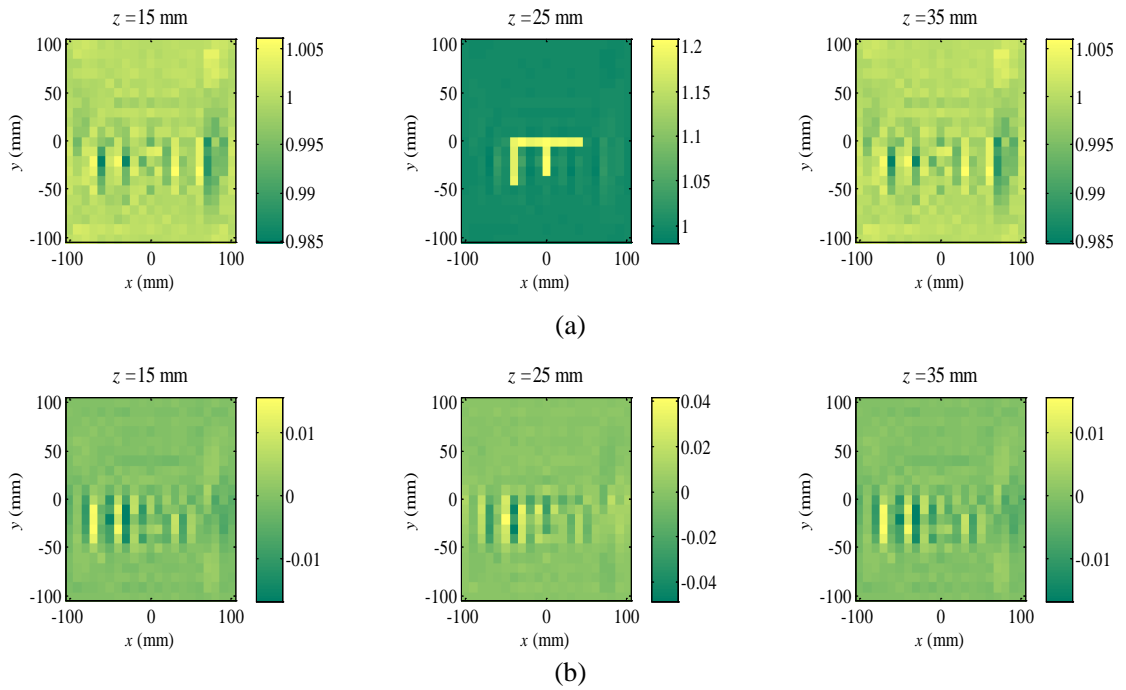


Figure 3.6 Plotting image reconstruction with direct inversion of $\mathbf{A}\boldsymbol{\tau} = \mathbf{b}$: (a) the real part of the permittivity distribution, (b) the imaginary part of the permittivity distribution.

The rRMSE value for the direct inversion is 0.0068676 with a runtime of 396.75 seconds.

It can be seen from these images that although the permittivity distribution for the F-shaped target is correct, the physical constraints are not satisfied. This could be due to the fact that inverse problems tend to be non-unique.

We can apply physically-based constraints to the LS problem to potentially improve the results.

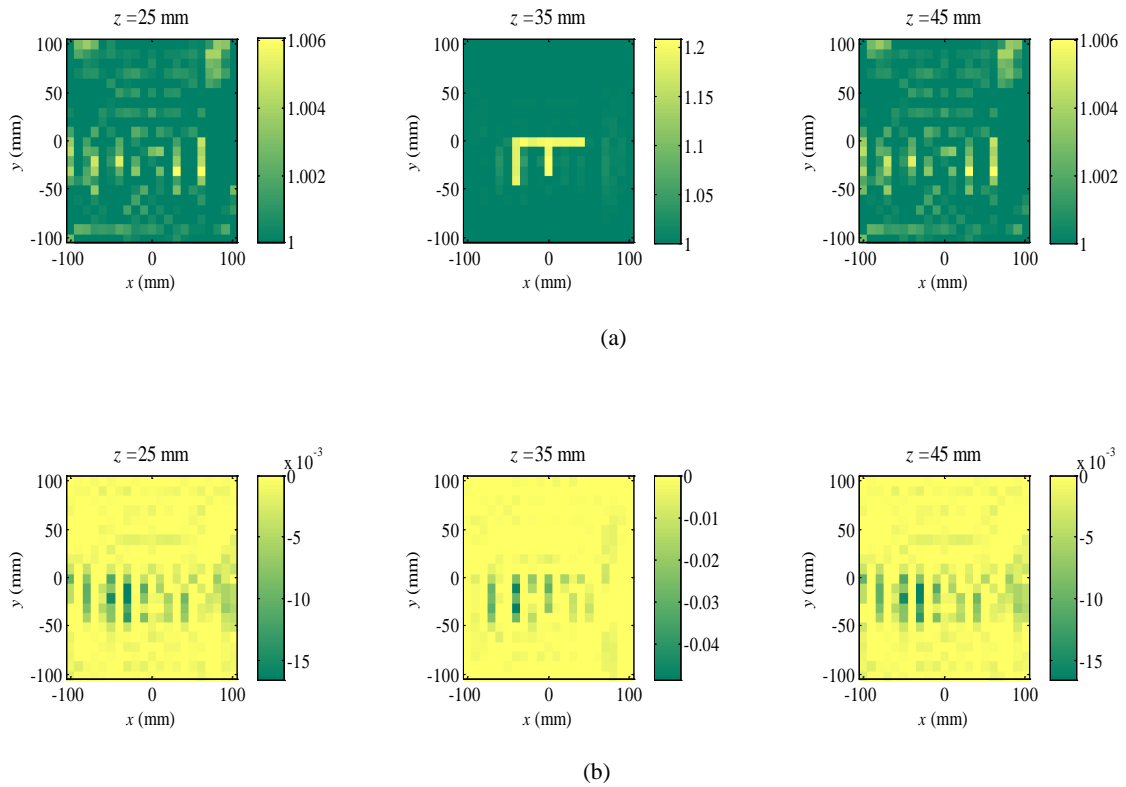


Figure 3.7 These are the results from the CGSI method: (a) the real part of the permittivity distribution, (b) the imaginary part of the permittivity distribution [1].

As can be seen by the results in Figure 3.7, the constrained global spectral inversion (CGSI) method is capable of determining the permittivity distribution of the OUT. The runtime of this algorithm was timed to be 482.8 seconds. For this example, the rRMSE was calculated to be 0.0037902. We then compare these results to the UGSI case.

Table 3.2 A comparison between the unconstrained $\mathbf{A}\boldsymbol{\tau} = \mathbf{b}$ and the constrained $\mathbf{C}\mathbf{x} = \mathbf{d}$.

	Unconstrained Method	Constrained Method
rRMSE	0.0068676	0.0037902
Runtime (in seconds)	396.75	482.8

Although the rRMSE results are comparable, there is nothing preventing UGSI method from producing unrealistic permittivity distributions.

3.7 Conclusions

We have demonstrated that an imaging procedure in Fourier space has the capability of reconstructing the permittivity distribution of an F-shaped target quantitatively. The qualitative holographic results are the foundation for the quantitative method developed here and their quality is critical in solving accurately the quantitative problem.

Constraints can eliminate unrealistic permittivities. Although we must be cognizant of the fact that linear constraints can only be applied if $\Gamma_{\text{OUT}}(\mathbf{r})/\Gamma_{\text{CO}} \approx 1$. The relation (3.5) could be simplified by setting the permittivity of the RO to be very large

$$|\varepsilon_{\text{OUT}}(\mathbf{r})| \ll |\varepsilon_{\text{RO}}|, |\varepsilon_{\text{CO}}| \ll |\varepsilon_{\text{RO}}|. \quad (3.33)$$

However, this is impractical in most cases since the antennas should be well matched to the RO medium as well as the averaged OUT medium.

A disadvantage of the constrained method is that it assumes $\Gamma_{\text{OUT}}(\mathbf{r})/\Gamma_{\text{CO}} \approx 1$. In reality, the OUT's permittivity distribution is unknown, thus making it difficult to evaluate the validity of the imaging results.

Gradient-based optimization approaches that are capable of solving linear systems of equations with non-linear constraints exist, but they tend to be prohibitively slow, which makes the algorithm no longer quasi-real-time.

References

- [1] J.R. Thompson, J.J. McCombe, S. Tu, and N.K. Nikolova, “Quantitative imaging of dielectric objects based on holographic reconstruction,” *Radar Conf. (RadarCon), 2015 IEEE*, pp. 0679-0683, 10–15 May 2015.
- [2] S. Tu, J.J. McCombe, D.S. Shumakov, and N.K. Nikolova, “Fast quantitative microwave imaging with resolvent kernel extracted from measurements,” *Inverse Problems*, vol. 31, no. 4, 045007 (33 pp.), Feb. 2015.
- [3] R.K. Amineh, M. Ravan, J. McCombe, and N.K. Nikolova. “Three-dimensional microwave holographic imaging employing forward-scattered waves only,” *Int. J. of Antennas and Propag.*, vol. 2013, Article ID 897287 (15 pp.), April 2013.
- [4] R.K. Amineh, J.J. McCombe, A. Khalatpour, and N.K. Nikolova, “Microwave holography using point-spread functions measured with calibration objects,” *IEEE Trans. Instrum. & Meas.*, vol. 64, no. 2, pp. 403-417, Feb. 2015.
- [5] R.K. Amineh, J. McCombe, and N.K. Nikolova, “Microwave holographic imaging using the antenna phaseless radiation pattern,” *IEEE Antennas Wireless Propag. Lett.*, vol. 12, pp. 1529-1532, Dec. 2012.
- [6] A.V. Oppenheim and R.W. Schaffer, *Discrete-Time Signal Processing*, 2nd ed. Upper Saddle, NJ: Prentice Hall, 1999.
- [7] The Mathworks, MATLAB, Natick, MA, USA, 2012, <http://www.mathworks.com/>.
- [8] M.C. Grant and S.P. Boyd, CVX Research, Stanford, California: 2012, <http://www.cvxr.com>.
- [9] Mosek ApS, Mosek, Copenhagen, Denmark, 1997, <https://www.mosek.com>.

[10]J.J. McCombe, “Noise reduction in microwave imaging and detection,” M.A.Sc.

Thesis, Dept. Elect. and Comp. Eng., McMaster Univ., 2014.

[11]FEKO suite 6.2, EM Software & System, Inc. USA, <http://www.feko.info>.

Chapter 4

Quantitative Imaging Using Pointwise Spectral Inversion

4.1 Introduction

This chapter looks into a fast but unconstrained least-squares (LS) solution to the quantitative holographic problem. This method is the author's second proposed method to reconstruct the permittivity distribution of a dielectric target using the near-field microwave holography approach. In (2.31), we notice that the permittivity function of the object under test (OUT) is $\tilde{\mathbf{F}}_{\text{OUT}}(\boldsymbol{\kappa})$, which is directly proportional to the permittivity distribution in Fourier space. If the permittivity distribution can be accurately reconstructed by this method, we can eliminate the need to compute the qualitative maps for the calibration object (CO) and avoid solving the large $N_v \times N_v$ linear system of equations.

However, unlike the method presented in chapter 3, we are unable to transfer the electrical constraints of (3.25) to Fourier space. We investigate the impact of the lack of constraints by tabulating the relative root-mean squared error (rRMSE) values and runtimes of this chapter's pointwise spectral inversion method and the constrained global spectral inversion (CGSI) method from the previous chapter.

We also recall that in chapter 3, we set the gamma factor (GF) to be $\Gamma_{\text{OUT}}(\mathbf{r})/\Gamma_{\text{CO}} \approx 1$ in order to linearize the inverse problem and its constraints. The method used in this chapter does not require $\Gamma_{\text{OUT}}(\mathbf{r})/\Gamma_{\text{CO}} \approx 1$, since constraints are not used. Therefore, we can analyze both the case when $\Gamma_{\text{OUT}}(\mathbf{r})/\Gamma_{\text{CO}} \approx 1$ and when $\Gamma_{\text{OUT}}(\mathbf{r})/\Gamma_{\text{CO}} \neq 1$.

4.2 Using Pseudoinverse to Solve the Least-Squares Problem

4.2.1 Reformulating Matrices

As stated in chapter 2, $\tilde{\mathbf{F}}_{\text{OUT}}(\boldsymbol{\kappa}) = (\Delta\varepsilon_{\text{OUT}}(\boldsymbol{\kappa})/\delta\varepsilon_{\text{CO}}) * (\Gamma_{\text{OUT}}(\boldsymbol{\kappa})/\Gamma_{\text{CO}})$, where $*$ is the linear convolution operator and $\delta\varepsilon_{\text{CO}}$ is the permittivity contrast of the small scatterer.

This is of particular interest, since we could theoretically solve [1]-[7]

$$\tilde{\mathbf{K}}(\boldsymbol{\kappa})\tilde{\mathbf{F}}_{\text{OUT}}(\boldsymbol{\kappa}) = \tilde{\mathbf{S}}_{\text{OUT}}(\boldsymbol{\kappa}), \quad (4.1)$$

for $\Delta\varepsilon_{\text{OUT}}(\boldsymbol{\kappa})$ directly and obtain the permittivity distribution by applying an inverse Fourier transform (FT) to obtain the spectral solution. Since (4.1) is overdetermined we use the normal equations [8] to obtain a unique solution [1]-[7]

$$\tilde{\mathbf{K}}^\dagger(\boldsymbol{\kappa})\tilde{\mathbf{K}}(\boldsymbol{\kappa})\tilde{\mathbf{F}}_{\text{OUT}}(\boldsymbol{\kappa}) = \tilde{\mathbf{K}}^\dagger(\boldsymbol{\kappa})\tilde{\mathbf{S}}_{\text{OUT}}(\boldsymbol{\kappa}), \quad (4.2)$$

$$\tilde{\mathbf{F}}_{\text{OUT}}(\boldsymbol{\kappa}) = \tilde{\mathbf{K}}^+(\boldsymbol{\kappa})\tilde{\mathbf{S}}_{\text{OUT}}(\boldsymbol{\kappa}), \quad (4.3)$$

where the $+$ operator is the pseudoinverse operator and the \dagger operator is the Hermitian operator. This result forms the basis of the second quantitative holographic reconstruction

method of dielectric targets, which we refer to as the pointwise spectral inversion (PSI) method.

4.2.2 Fourier Space Constraints

For the method presented in chapter 3, we applied the constraints $\text{Re}\{\boldsymbol{\epsilon}_{\text{OUT}}\} \geq 1$ and $\text{Im}\{\boldsymbol{\epsilon}_{\text{OUT}}\} \leq 0$ in (3.25) to the LS problem in (3.31) to eliminate the occurrence of non-physical permittivities. It could be beneficial to apply constraints in Fourier space; however, we realize that we cannot apply the FTs directly to (3.25) since those regions are not integrable [9]

$$\begin{aligned} \int_{-\infty}^{\infty} \int_{-\infty}^{\infty} |\text{Re}\{\boldsymbol{\epsilon}_{\text{OUT}}\} \geq 1| dx dy &\rightarrow \infty, \\ \int_{-\infty}^{\infty} \int_{-\infty}^{\infty} |\text{Im}\{\boldsymbol{\epsilon}_{\text{OUT}}\} \leq 0| dx dy &\rightarrow \infty. \end{aligned} \tag{4.4}$$

Applying physically-based constraints in Fourier space remains an unsolved problem for now. Thus, we focus on analyzing the unconstrained solution since it could be useful.

4.2.3 Quantitative Results with the Gamma Factor Set to Unity

After solving (4.3) by performing the pseudoinverse at each $\boldsymbol{\kappa}$ pair, we then apply the inverse FT to the solution of (4.3). Assuming that $\Gamma_{\text{OUT}}(\mathbf{r})/\Gamma_{\text{CO}} \approx 1$, the permittivity distribution is obtained as

$$f_{\text{OUT}}(x, y, z_n) = \frac{\Delta \varepsilon_{\text{OUT}}(x, y, z_n)}{\delta \varepsilon_{\text{CO}}} = \frac{\varepsilon_{\text{OUT}}(x, y, z_n) - \varepsilon_{\text{RO}}}{\delta \varepsilon_{\text{CO}}}, \quad (4.5)$$

$$\therefore \varepsilon_{\text{OUT}}(x, y, z_n) = \delta \varepsilon_{\text{CO}} f_{\text{OUT}}(x, y, z_n) + \varepsilon_{\text{RO}}.$$

4.2.4 Quantitative Results with the Quasi-Analytic Gamma Factor

Setting the GF to unity is a crude approximation. A better approximation is offered in chapter 2 by the localized nonlinear (LN) theory [10]. We can modify the result in (4.5) such that it takes into consideration the LN approximation of the GF:

$$\begin{aligned} f_{\text{OUT}}(x, y, z_n) &= \frac{\Delta \varepsilon_{\text{OUT}}(x, y, z_n)}{\delta \varepsilon_{\text{CO}}} \frac{\Gamma_{\text{OUT}}(x, y, z_n)}{\Gamma_{\text{CO}}}, \\ &= \left[\frac{\varepsilon_{\text{OUT}}(x, y, z_n) - \varepsilon_{\text{RO}}}{\delta \varepsilon_{\text{CO}}} \right] \left[\frac{\varepsilon_{\text{CO}} + 2\varepsilon_{\text{RO}}}{\varepsilon_{\text{OUT}}(x, y, z_n) + 2\varepsilon_{\text{RO}}} \right]. \end{aligned} \quad (4.6)$$

By using arranging (4.6) for $\varepsilon_{\text{OUT}}(x, y, z_n)$ and using polynomial division, the permittivity distribution can be expressed as

$$\varepsilon_{\text{OUT}}(x, y, z_n) = \frac{3\varepsilon_{\text{RO}}}{1 - \frac{\delta \varepsilon_{\text{CO}} f_{\text{OUT}}(x, y, z_n)}{\varepsilon_{\text{CO}} + 2\varepsilon_{\text{RO}}}} - 2\varepsilon_{\text{RO}}. \quad (4.7)$$

This solution may have better accuracy than the one where $\Gamma_{\text{OUT}}(\mathbf{r}) / \Gamma_{\text{CO}} \approx 1$. However, we see in the next chapter that it is not necessarily the case, because the quasi-analytic (QA) GF still does not account for multiple scattering. The following flowchart illustrates the procedure of the PSI method.

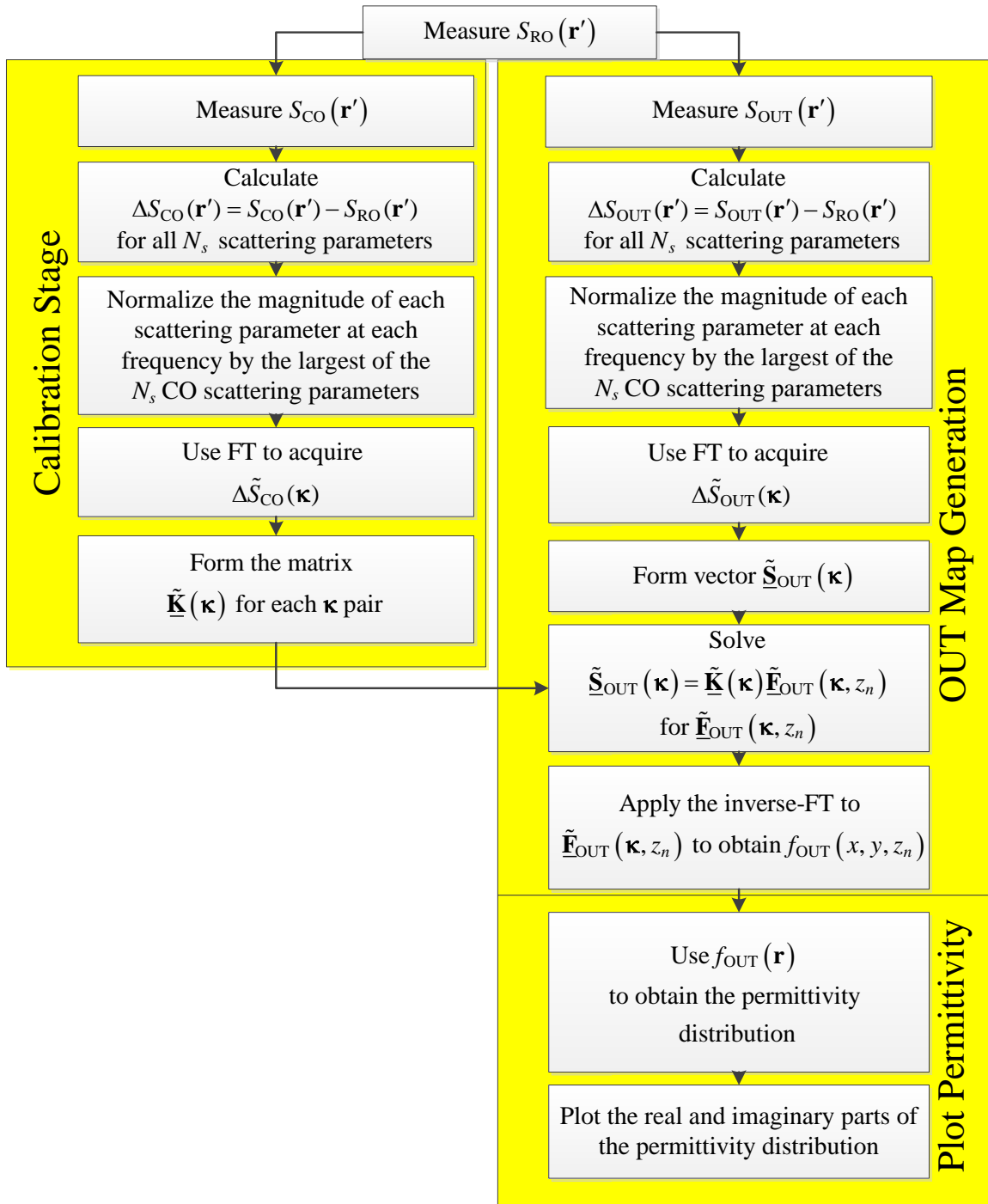


Figure 4.1 Algorithm flowchart of the PSI method.

4.3 Results

We begin by plotting the permittivity distributions of the F-shaped target of permittivity $1.2-j0$ when the CO has permittivity $1.1-j0$. The background medium has permittivity $1-j0$. The results are obtained using the PSI method. Figure 4.2 shows the results of the reconstruction when $\Gamma_{\text{OUT}}(\mathbf{r})/\Gamma_{\text{CO}} \approx 1$. Figure 4.3 shows the results for the case when $\Gamma_{\text{OUT}}(\mathbf{r})/\Gamma_{\text{CO}} \neq 1$. The first and second rows of the images in both figures indicate the real and imaginary parts of the permittivity distributions, respectively.

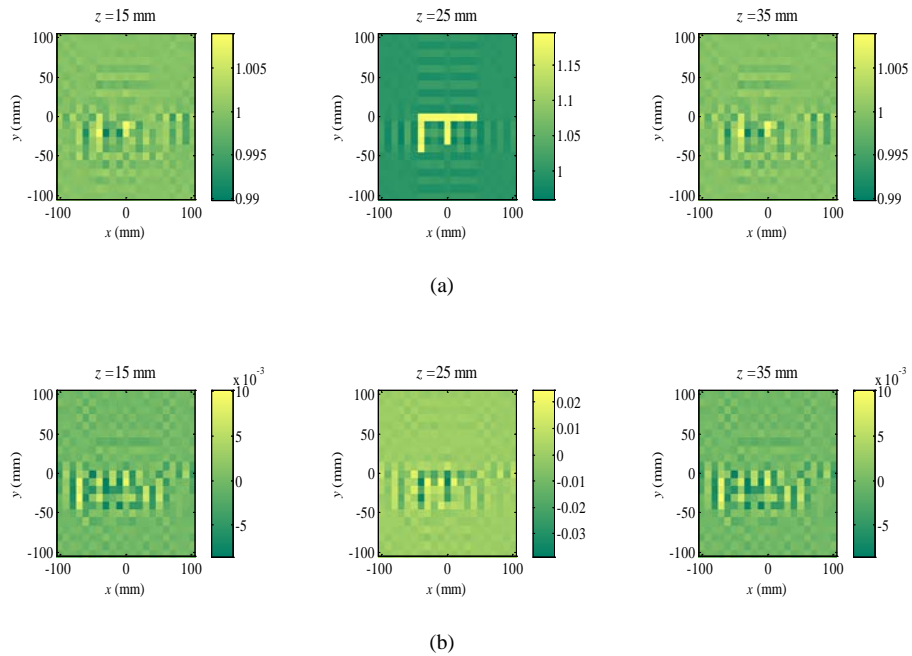


Figure 4.2 Results of the PSI method with $\Gamma_{\text{OUT}}(\mathbf{r})/\Gamma_{\text{CO}} \approx 1$: (a) the real part of the permittivity distribution, (b) the imaginary part of the permittivity distribution.

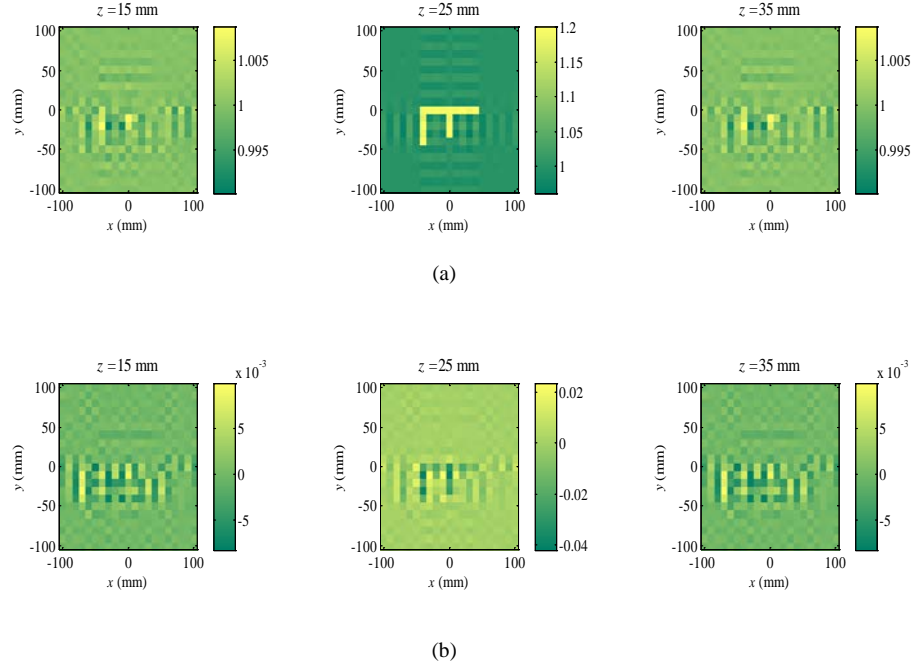


Figure 4.3 Results of the PSI method with $\Gamma_{\text{OUT}}(\mathbf{r})/\Gamma_{\text{CO}} \neq 1$: (a) the real part of the permittivity distribution. (b) the imaginary part of the permittivity distribution.

It can be seen in both Figure 4.2 and Figure 4.3 that the F-shape is accurately reconstructed. If we compare these results with that of Figure 3.7, we notice that they are almost identical in terms of shape. We tabulate the results to compare which of the methods presented thus far performs the best.

Table 4.1 Comparison of the PSI and CGSI methods' runtimes and rRMSE.

	PSI Method $\frac{\Gamma_{\text{OUT}}(\mathbf{r})}{\Gamma_{\text{CO}}} \approx 1$	PSI Method $\frac{\Gamma_{\text{OUT}}(\mathbf{r})}{\Gamma_{\text{CO}}} \neq 1$	CGSI Method
rRMSE	0.0085321	0.0083061	0.0037902
Runtime (in seconds)	2.28	2.26	482.8

After analyzing the three cases, it appears that both of the PSI methods are the better choice for reconstructing the F-shaped target, since they are less expensive and reasonably accurate. Although the CGSI method was able to provide the most accurate results, the improvement in rRMSE is not significant enough to justify the computational burden. The GF played a negligible role in both the runtime and rRMSE, but we must keep in mind that in this example $\varepsilon_{\text{OUT}}(\mathbf{r}) \approx \varepsilon_{\text{CO}}$.

4.4 Conclusions

Although this method considered here is fast and can produce results within seconds, it runs the risk of having non-physical permittivity distributions, as can be seen in Figure 4.2 and Figure 4.3. This demonstrates the importance of the physically-based constraints on the quantitative solution. On the other hand, this pointwise spectral inversion method has an advantage over the spectral domain inversion method because the qualitative maps of the CO do not need to be computed. Also, instead of solving one large system of equations, here we solve a multitude of very small systems of equations (for each κ pair). These two factors lead to a drastic reduction of the computational times so that reconstruction is performed in a matter of seconds.

The model presented in this thesis does not take into account mutual coupling. This prevents the accurate imaging of complex objects and is the drawback of all direct inversion methods. This is the principle motive to explore image reconstruction techniques that use iterative solvers [11]. This leads us into the next chapter, which

discusses the impacts of changing the permittivity distributions of either the CO or the OUT.

References

- [1] R.K. Amineh, M. Ravan, A. Khalatpour, and N.K. Nikolova, “Three-dimensional near-field microwave holography using reflected and transmitted signals,” *IEEE Trans. Antennas Propag.*, vol. 59, no. 12, pp. 4777-4789, Dec. 2012.
- [2] R.K. Amineh, A. Khalatpour, H. Xu, Y. Baskharoun, and Natalia K. Nikolova, “Three-dimensional near-field microwave holography for tissue imaging,” *Int. J. Biomed. Imag.*, vol. 2012, Art. 291494 (11 pp.) , Dec. 2012.
- [3] R.K. Amineh, J. McCombe, and N.K. Nikolova, “Microwave holographic imaging using the antenna phaseless radiation pattern,” *IEEE Antennas Wireless Propag. Lett.*, vol. 12, pp. 1529-1532, Dec. 2012.
- [4] R.K. Amineh, M. Ravan, J. McCombe, and N.K. Nikolova. “Three-dimensional microwave holographic imaging employing forward-scattered waves only,” *Int. J. of Antennas and Propag.*, vol. 2013, Article ID 897287 (15 pp.), April 2013.
- [5] R.K. Amineh, J.J. McCombe, A. Khalatpour, and N.K. Nikolova, “Microwave holography using point-spread functions measured with calibration objects,” *IEEE Trans. Instrum. & Meas.*, vol. 64, no. 2, pp. 403-417, Feb. 2015.
- [6] J.J. McCombe “Noise reduction in microwave imaging and detection,” M.A.Sc. Thesis, Dept. Elect. and Comp. Eng., McMaster Univ., 2014.

- [7] M. Ravan, R.K. Amineh, and N.K. Nikolova, "Two-dimensional near-field microwave holography," *Inverse Problems*, vol. 26, no. 5, 0555011 (21 pp.), May 2010.
- [8] M. Bakr, *Nonlinear Optimization in Electrical Engineering with Applications in MATLAB*, IET, 2013.
- [9] C.H. Edwards and D.E. Penney, *Calculus Early Transcendentals*, 7th ed., 2008.
- [10] T.M. Habashy, R.W. Groom, and B.R. Spies, "Beyond the Born and Rytov approximations: a nonlinear approach to electromagnetic scattering," *J. Geophys. Res.*, vol. 98, no. B2, pp. 1759-1775, Feb. 1993.
- [11] F. Li, Q.H. Liu, and Lin-Ping Song, "Three-dimensional reconstruction of objects buried in layered media using Born and distorted Born iterative methods," *IEEE Geosci. and Remote Sensing Lett.*, vol. 1, no. 2, pp. 107-111, April 2004.

Chapter 5

Comparison of the Constrained Global Spectral Inversion and Pointwise Spectral Inversion Methods

5.1 Introduction

So far we have only reconstructed images for an object under test (OUT) with permittivity $1.2-j0$ and a calibration object (CO) with permittivity $1.1-j0$ both embedded in a reference object (RO) of permittivity $1-j0$. However, if we are to use this reconstruction technique for either tissue imaging or non-destructive testing, we need to increase the permittivity contrast between the scatterers (CO or OUT) and the RO.

Although mutual coupling is not taken into account in the proposed method, the solution obtained from either one of the pointwise spectral inversion (PSI) methods or the constrained global spectral inversion (CGSI) method are intended to be used as an initial value in an iterative solver like the one used in [1]. Thus, we need to determine which method is best suited for our application. As tabulated in Table 4.1, the PSI methods perform better in terms of speed and are almost as accurate as the CGSI method. So, the question remains: Is the CGSI method worth implementing if the computational cost is two orders of magnitude larger than the PSI method? This chapter looks into a variety of

scenarios of permittivity distributions to determine which approach would be the best candidate to use as an initial guess for the iterative solvers.

5.2 Results

5.2.1 F-shaped Target with Permittivity $9-j0$ and a Calibration Object of Permittivity $9-j0$

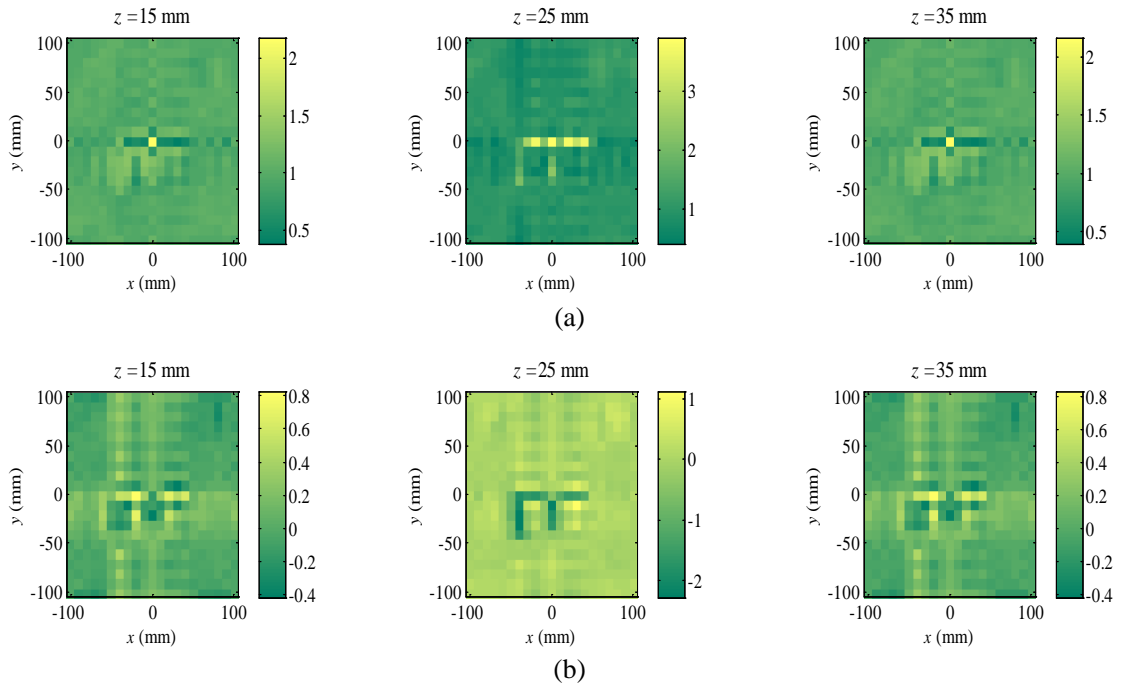


Figure 5.1 The PSI method for an F-shaped target with permittivity $9-j0$ and a CO of permittivity $9-j0$ with $\Gamma_{\text{OUT}}(\mathbf{r})/\Gamma_{\text{CO}} \approx 1$: (a) the real part of the permittivity distribution, (b) the imaginary part of the permittivity distribution.

Consider the case where the F-shaped target has a permittivity of $9-j0$ located 25 mm away from the transmitting (Tx) antenna and a CO of permittivity $9-j0$ and a RO of permittivity $1-j0$. We begin by displaying the images obtained with the PSI method when

$\Gamma_{\text{OUT}}(\mathbf{r})/\Gamma_{\text{CO}} \approx 1$. Notice that the F-shape appears in the imaginary part of the permittivity as well. That is inaccurate and constitutes an image artifact.

We can use the localized nonlinear (LN) and quasi-analytic (QA) approximations by including the gamma factor (GF), where the results of including the GF in the PSI method are shown in Figure 5.2 [2]–[5].

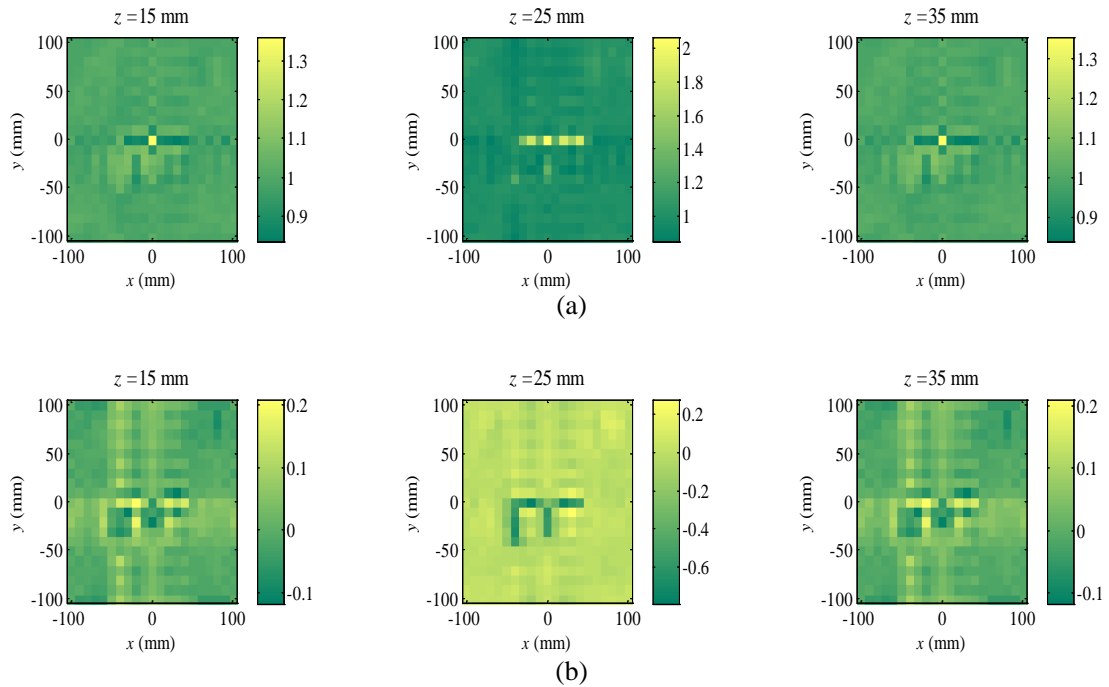


Figure 5.2 The PSI method for an F-shaped target with permittivity $9-j0$ and a CO of permittivity $9-j0$ with $\Gamma_{\text{OUT}}/\Gamma_{\text{CO}} \neq 1$: (a) the real part of the permittivity distribution, (b) the imaginary part of the permittivity distribution.

The result appears to have not changed compared to Figure 5.1. This is likely due to the fact that actually $\Gamma_{\text{OUT}}(\mathbf{r})/\Gamma_{\text{CO}} = 1$. To ensure that the data acquired is not corrupted, the qualitative images are reconstructed as well. They are shown in Figure 5.3.

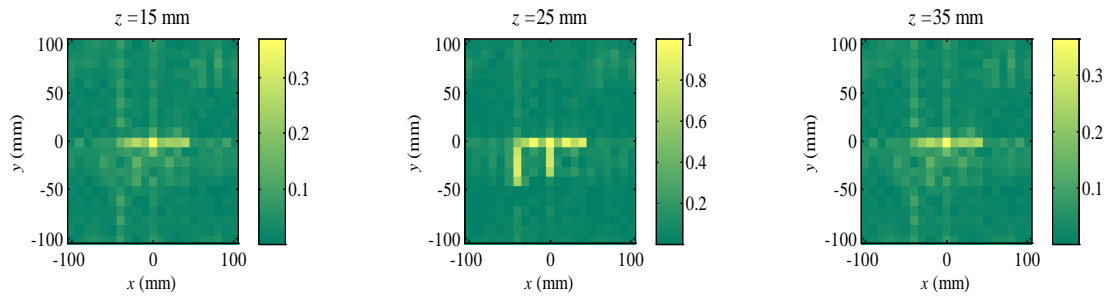


Figure 5.3 Qualitative holographic technique of the F-shaped target of permittivity $9-j0$ using a CO of permittivity $9-j0$.

While the permittivity distributions are not correct, the qualitative results show the F-shape correctly. We can observe the impact of the constraints have by applying the CGSI method in Figure 5.4.

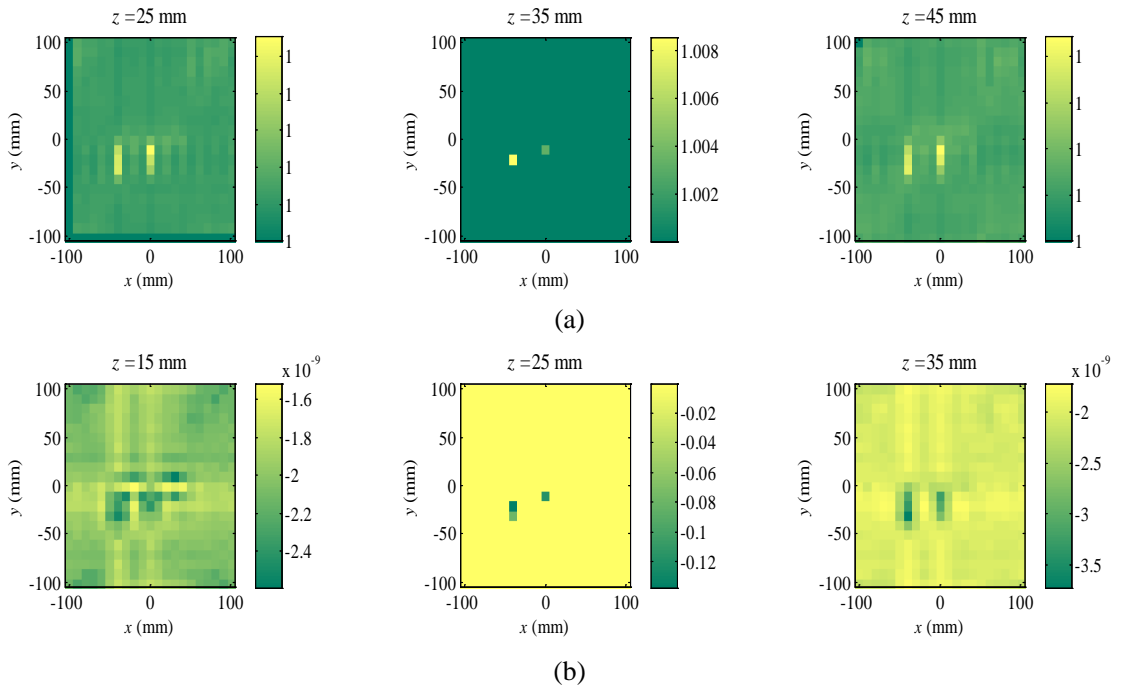


Figure 5.4 The image reconstruction of the F-shape of permittivity $9-j0$ with a CO of permittivity $9-j0$ using the CGSI method: (a) the real part of the permittivity distribution, (b) the imaginary part of the permittivity distribution.

Figure 5.4 shows the real part of the F-shape's permittivity to be not as close to the true value as either of the PSI methods; although, the background is reconstructed accurately.

This could be due to the fact that $\Gamma_{\text{OUT}}(\mathbf{r})/\Gamma_{\text{CO}} = 1$ in the background medium.

To compare the three methods, we tabulate the runtimes and the relative root-mean squared error (rRMSE) values.

Table 5.1 Comparison of the PSI methods and the CGSI method in the example with CO of permittivity 9-j0 and F-shaped target of permittivity 9-j0.

	PSI Method $\frac{\Gamma_{\text{OUT}}(\mathbf{r})}{\Gamma_{\text{CO}}} \approx 1$	PSI Method $\frac{\Gamma_{\text{OUT}}(\mathbf{r})}{\Gamma_{\text{CO}}} \neq 1$	CGSI Method
rRMSE	0.21075	0.1065	0.097519
Runtime (in seconds)	2.14	2.73	409.8

We notice that in this example, the CGSI method had the best rRMSE value, but the improvement over the PSI method with $\Gamma_{\text{OUT}}(\mathbf{r})/\Gamma_{\text{CO}} \neq 1$ is significant. Surprisingly, the PSI method where $\Gamma_{\text{OUT}}(\mathbf{r})/\Gamma_{\text{CO}} \approx 1$ performed poorly despite the fact that $\varepsilon_{\text{OUT}}(\mathbf{r}) \approx \varepsilon_{\text{CO}}$. This may be due to significant multiple scattering or mutual coupling effects, which our model cannot take into account.

5.2.2 Small Scatterer with Permittivity 9-j0 and a Calibration Object with Permittivity 9-j0

To reduce the impact of mutual coupling, we reconstruct the small scatterer as the OUT.

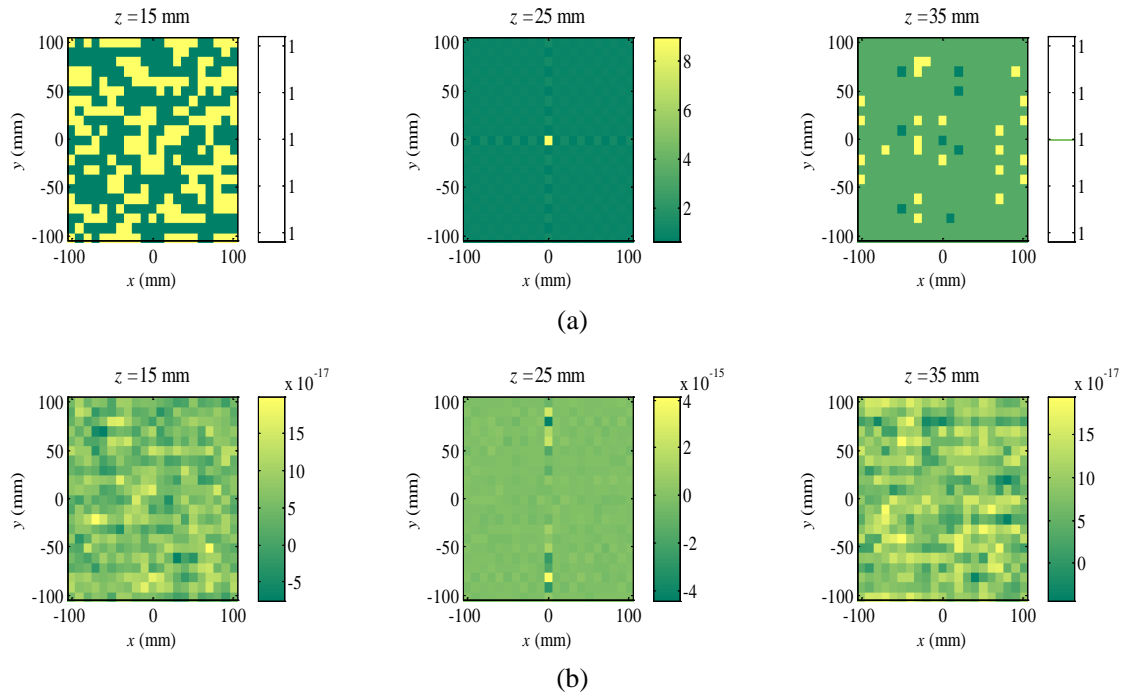


Figure 5.5 The image reconstruction of a small scatterer of permittivity $9-j0$ with a CO of relative permittivity $9-j0$ using the PSI method where $\Gamma_{\text{OUT}} / \Gamma_{\text{CO}} \approx 1$: (a) the real part of the permittivity distribution, (b) the imaginary part of the permittivity distribution.

We notice that we can accurately reconstruct the OUT's permittivity distribution without the GF. However, in order to determine the impact of the GF on the PSI method, we also need to analyze the case when the GF is included. Figure 5.6 shows the results of the PSI technique when the GF is included.

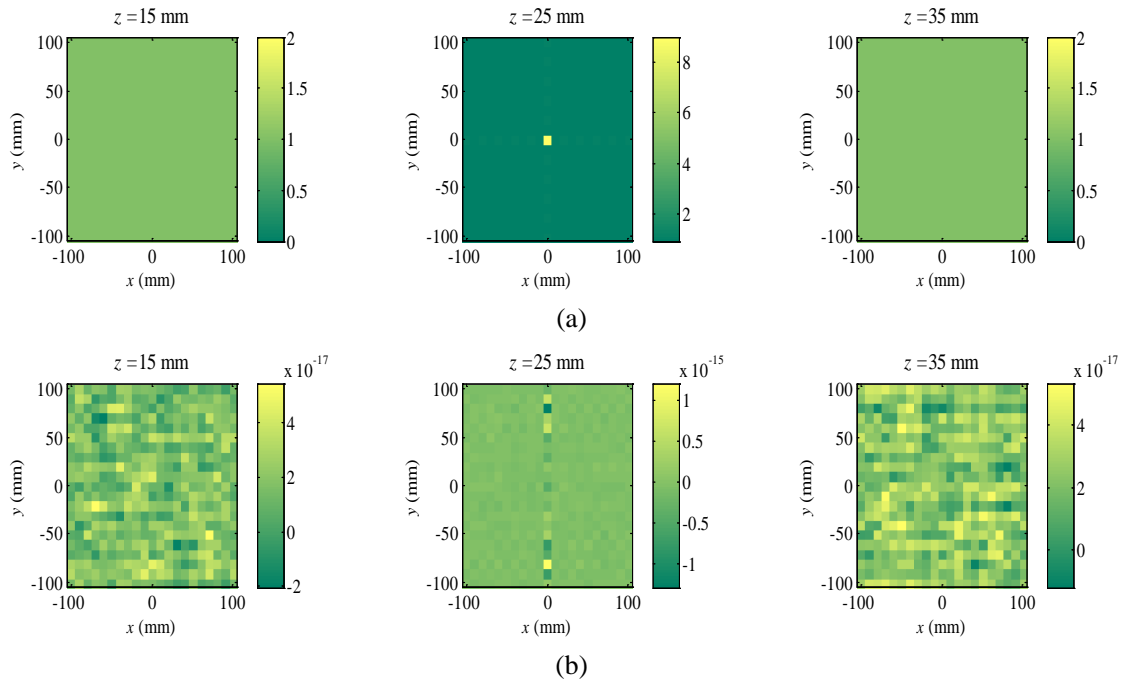


Figure 5.6 The image reconstruction using the PSI method for a small scatterer with permittivity of $9-j0$ and a CO with permittivity of $9-j0$ where $\Gamma_{\text{OUT}}/\Gamma_{\text{CO}} \neq 1$: (a) the real part of the permittivity distribution, (b) the imaginary part of the permittivity distribution.

We observe that the addition of the GF had no impact on the result since $\Gamma_{\text{OUT}}(\mathbf{r})/\Gamma_{\text{CO}} = 1$. To ensure that the data is not corrupted, we analyze the qualitative images of the F-shaped target.

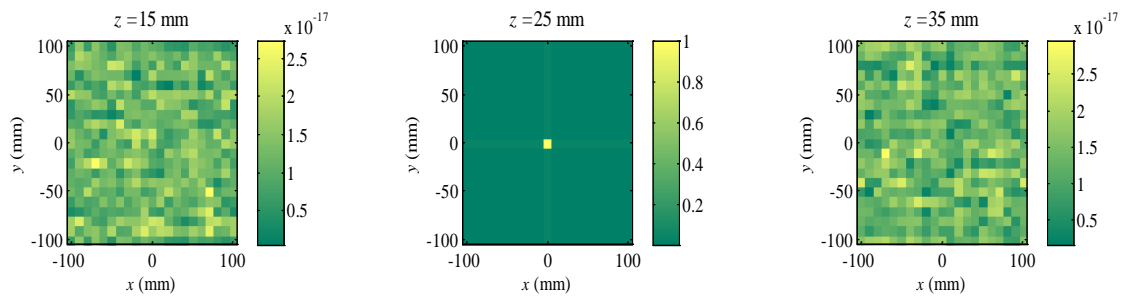


Figure 5.7 Qualitative images of a small scatterer with permittivity $9-j0$ and a CO of permittivity $9-j0$.

The qualitative images show that the small scatterer is in the correct location. We observe the impact of the constraints on the image reconstruction of this problem.

We notice in Figure 5.8 that the CGSI method does not result in significantly improved image reconstruction; although unlike the PSI methods, the CGSI method was not able to correctly display the permittivity of the small scatterer. However, it was able to reconstruct the background medium's permittivity distribution better.

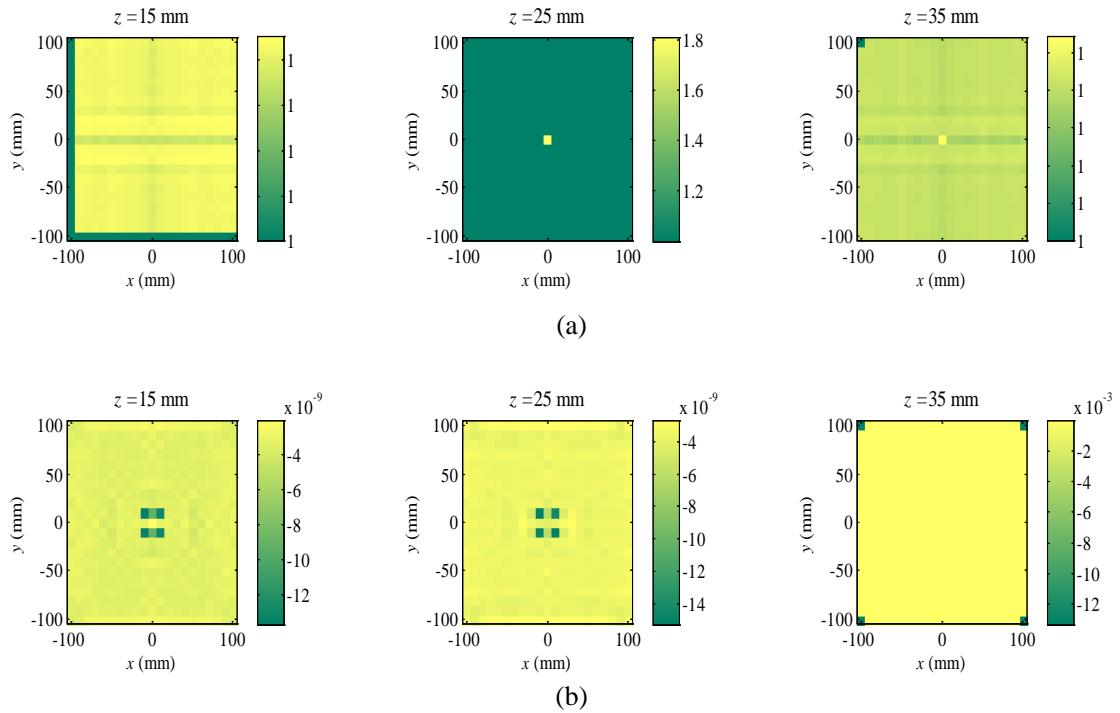


Figure 5.8 The image reconstruction of a small scatterer of permittivity $9-j0$ using a CO with permittivity of $9-j0$ using the CGSI method: (a) the real part of the permittivity distribution, (b) the imaginary part of the permittivity distribution.

Table 5.2 Comparison of the PSI methods and the CGSI method in the example with CO of permittivity $9-j0$ and a small scatterer of permittivity $9-j0$.

	PSI Method $\frac{\Gamma_{\text{OUT}}(\mathbf{r})}{\Gamma_{\text{CO}}} \approx 1$	PSI Method $\frac{\Gamma_{\text{OUT}}(\mathbf{r})}{\Gamma_{\text{CO}}} \neq 1$	CGSI Method
rRMSE	0.066987	0.018301	0.021974
Runtime (in seconds)	2.89	3.69	420.58.

For this case, the differences in rRMSE values are drastic for all three methods, but the computational cost between the PSI methods and the CGSI method is large. For this case,

the PSI method with the GF performed the best since it had a low rRMSE value and low computational cost.

5.2.3 F-shaped Target with Permittivity $9-j0$ and a Calibration Object with Permittivity $1.1-j0$

It is expected that the CGSI method is not going to be accurate since the GF is not approximately one. But for the purpose of comparing the proposed methods, it is crucial to analyze the impact of such a drastic violation.

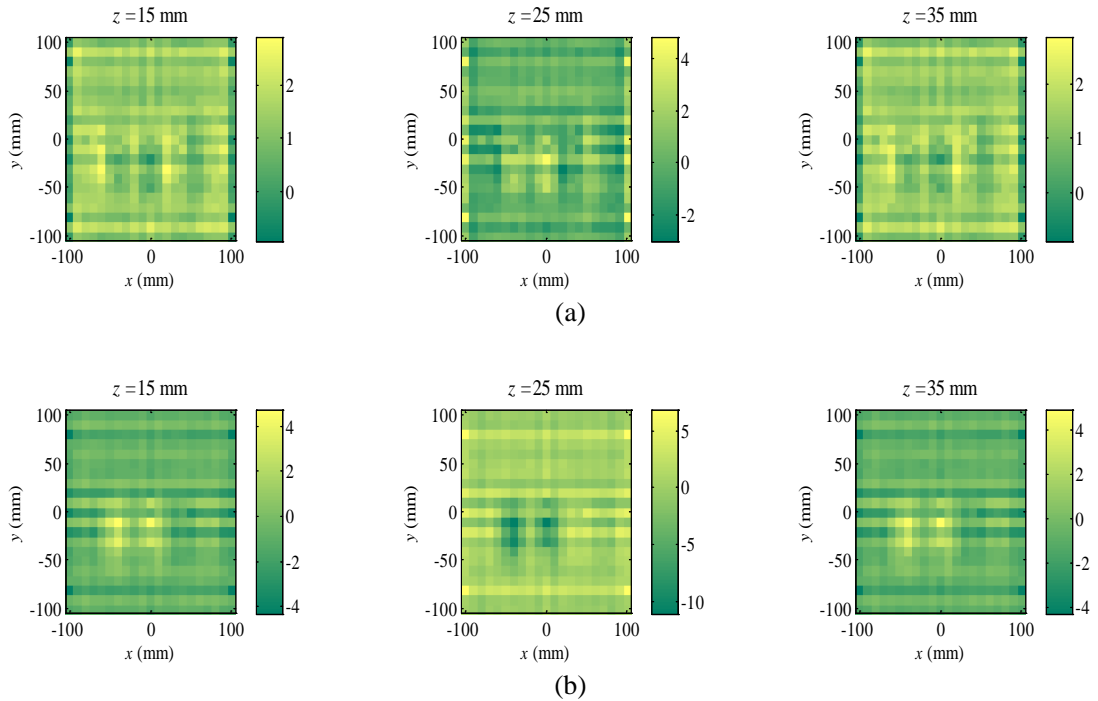


Figure 5.9 The image reconstruction of an F-shape with permittivity $9-j0$ and a CO of permittivity $1.1-j0$ using the PSI method where $\Gamma_{\text{OUT}} / \Gamma_{\text{CO}} \approx 1$: (a) the real part of the permittivity distribution, (b) the imaginary part of the permittivity distribution.

The results of the PSI method without the GF appear to be smeared. The F-shape also appears in all three layers in both the real and imaginary parts of the permittivity.

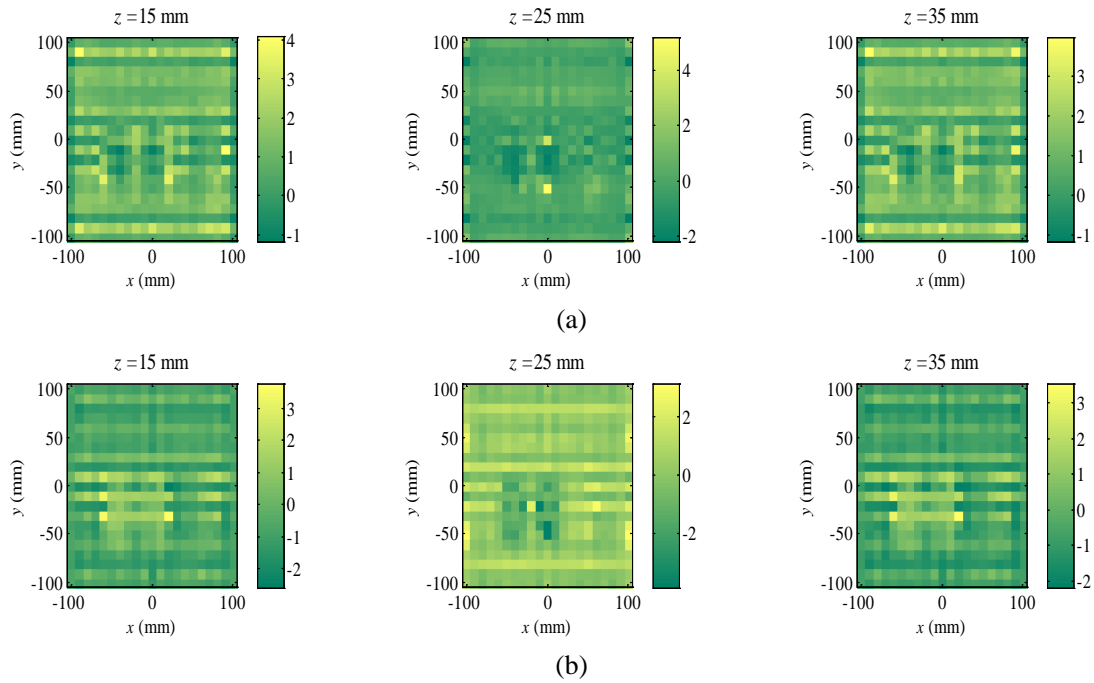


Figure 5.10 The image reconstruction of an F-shape with permittivity $9-j0$ and a CO of permittivity $1.1-j0$ using the PSI method where $\Gamma_{OUT} / \Gamma_{CO} \neq 1$: (a) The real part of the permittivity distribution. (b) The imaginary part of the permittivity distribution.

We notice that the GF did not have a noticeable impact on the results. To ensure that the data has not been corrupted, we display the qualitative images of the F-shape.

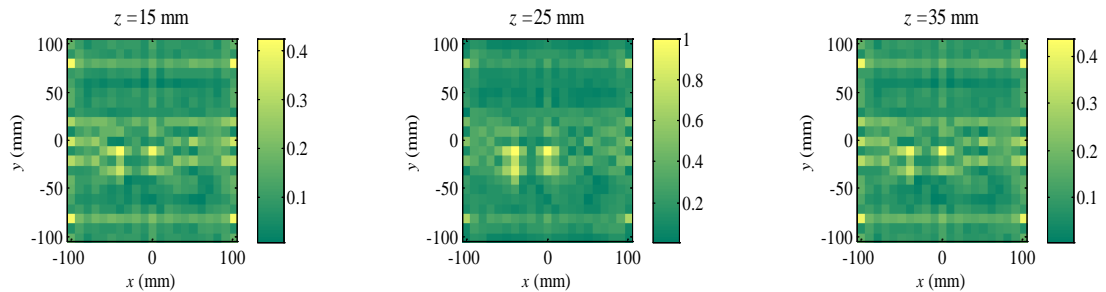


Figure 5.11 Qualitative results of F-shaped target with permittivity $9-j0$ and CO with permittivity $1.1-j0$.

These results show that we are unable to locate the F-shape with a qualitative method.

As mentioned before, if we are unable to obtain a qualitative result, there will be no quantitative result.

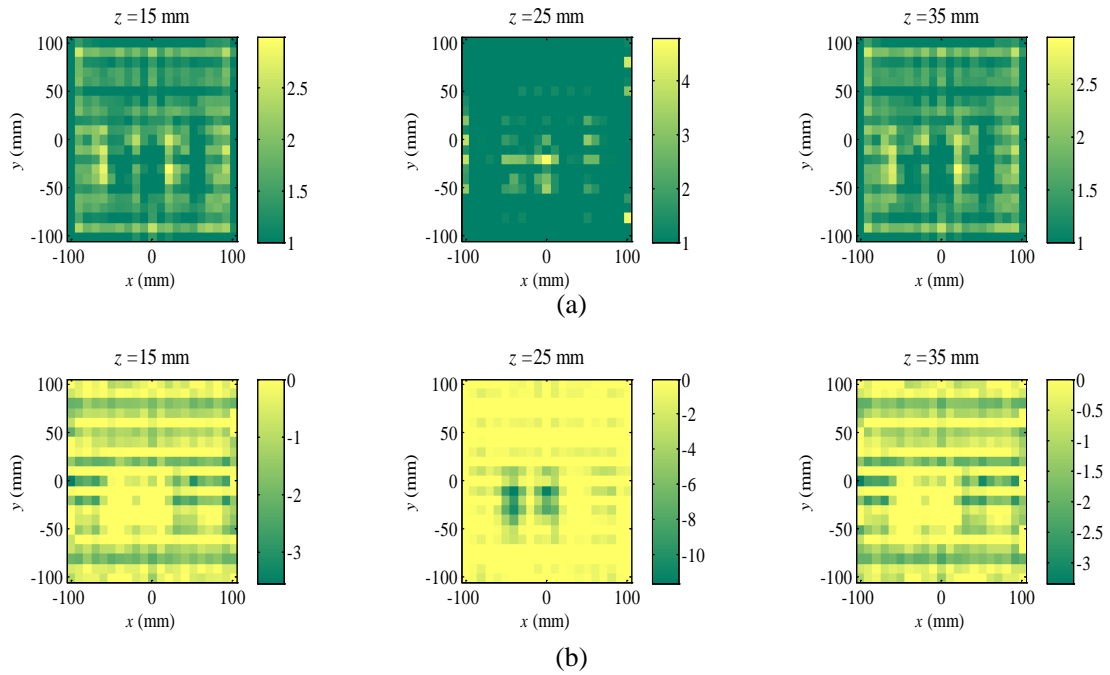


Figure 5.12 The image reconstruction of the F-shape with a permittivity of $9-j0$ and a CO of permittivity of $1.1-j0$ using the CGSI method: (a) the real part of the permittivity distribution, (b) the imaginary part of the permittivity distribution.

We then observe the impact of constraints to see if this method can overcome the poor qualitative results. Although the unrealistic permittivities have been eliminated, the results are still poor. We can compare the three methods in Table 5.3.

Table 5.3 Comparison of the PSI methods and the CGSI method in the example with CO of permittivity 1.1-j0 and an F-shaped target of permittivity 9-j0.

	PSI Method $\frac{\Gamma_{\text{OUT}}(\mathbf{r})}{\Gamma_{\text{CO}}} \approx 1$	PSI Method $\frac{\Gamma_{\text{OUT}}(\mathbf{r})}{\Gamma_{\text{CO}}} \neq 1$	CGSI Method
rRMSE	1.9155	1.444	1.310
Runtime (in seconds)	3.056	2.421856	397.88

The CGSI method outperformed the PSI method with $\Gamma_{\text{OUT}}(\mathbf{r})/\Gamma_{\text{CO}} \neq 1$ method in terms of accuracy by a slight margin. In fact, inserting the GF into the algorithm provided a significant improvement.

5.2.4 F-shaped Target with Permittivity 1.2-j0 and a Calibration Object with Permittivity 9-j0

We now analyze the case where the CO used has a permittivity 9-j0 with an F-shaped target of permittivity 1.2-j0 in a background medium with permittivity 1-j0. We notice that there are echoes in the results, which could be attributed to the limitations imposed by the implementation of the PSF.

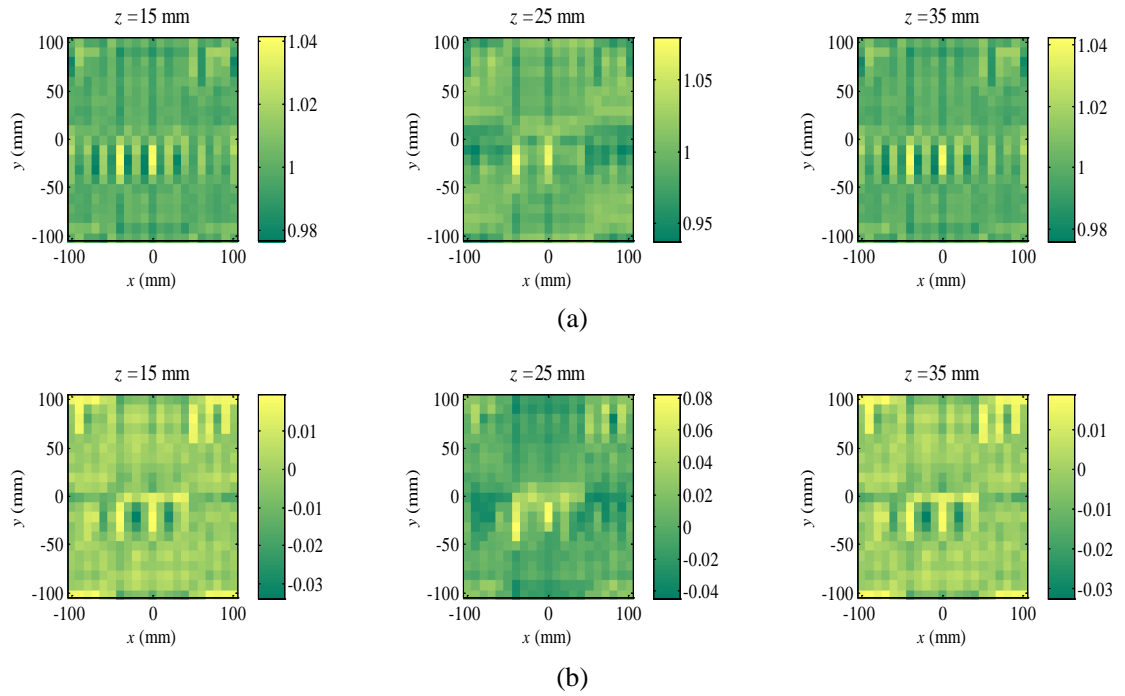


Figure 5.13 The image reconstruction of an F-shaped target with permittivity $1.2-j0$ and CO with permittivity $9-j0$. with the PSI method where $\Gamma_{\text{OUT}} / \Gamma_{\text{CO}} \approx 1$: (a) The real part of the permittivity distribution, (b) The imaginary part of the permittivity distribution.

If we include the GF we notice no significant improvements in the quantitative reconstruction.

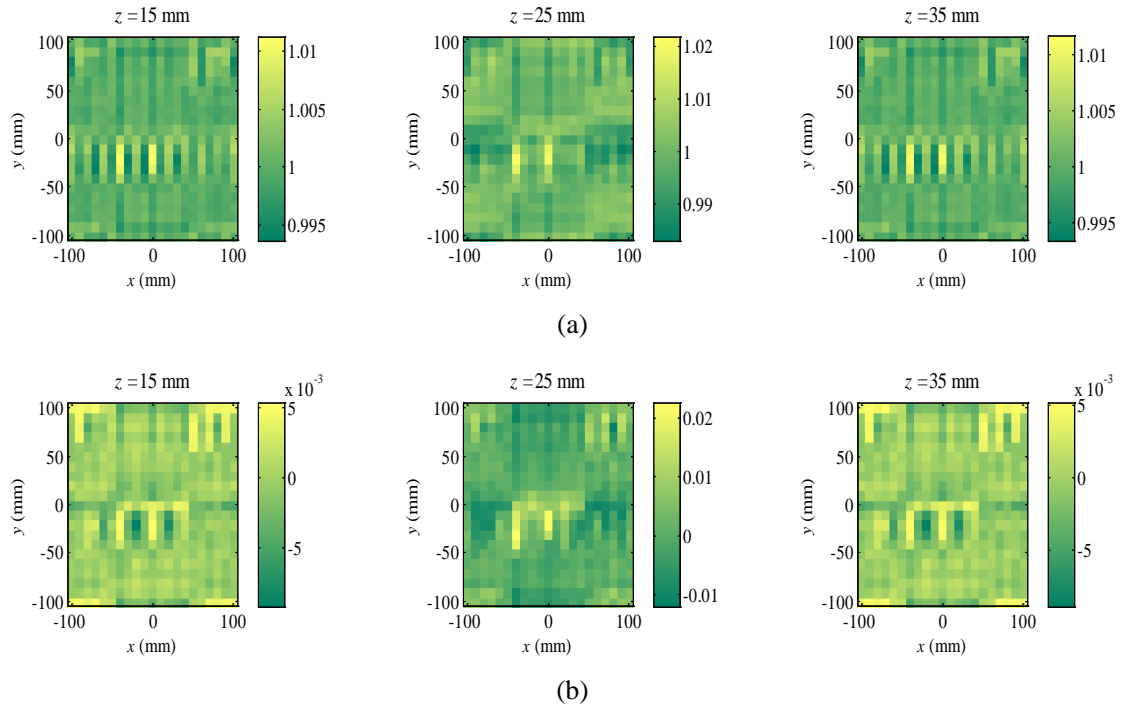


Figure 5.14 The image reconstruction of an F-shaped target with permittivity $1.2-j0$ and CO with permittivity $9-j0$ with the PSI method where $\Gamma_{\text{OUT}} / \Gamma_{\text{CO}} \neq 1$: (a) the real part of the permittivity distribution, (b) the imaginary part of the permittivity distribution.

We, once again, display the qualitative images of the F-shape to determine the quality of the data.

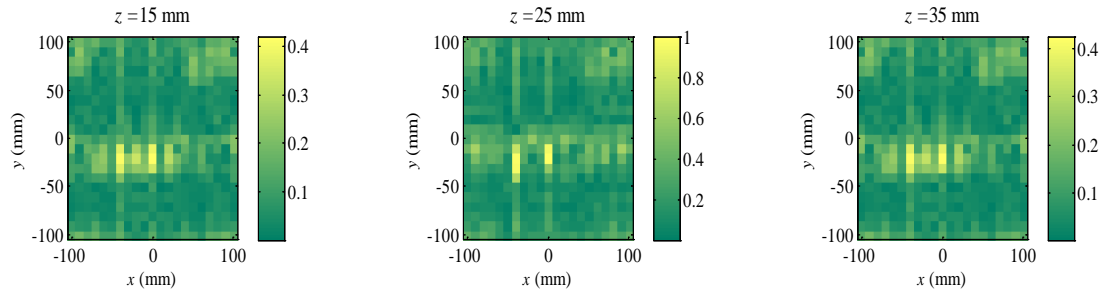


Figure 5.15 Qualitative results of the F-shaped target with permittivity $1.2-j0$ and CO with permittivity $9-j0$.

The results show that we are unable to obtain qualitative results with this set of data and is the reason for the poor quantitative results.

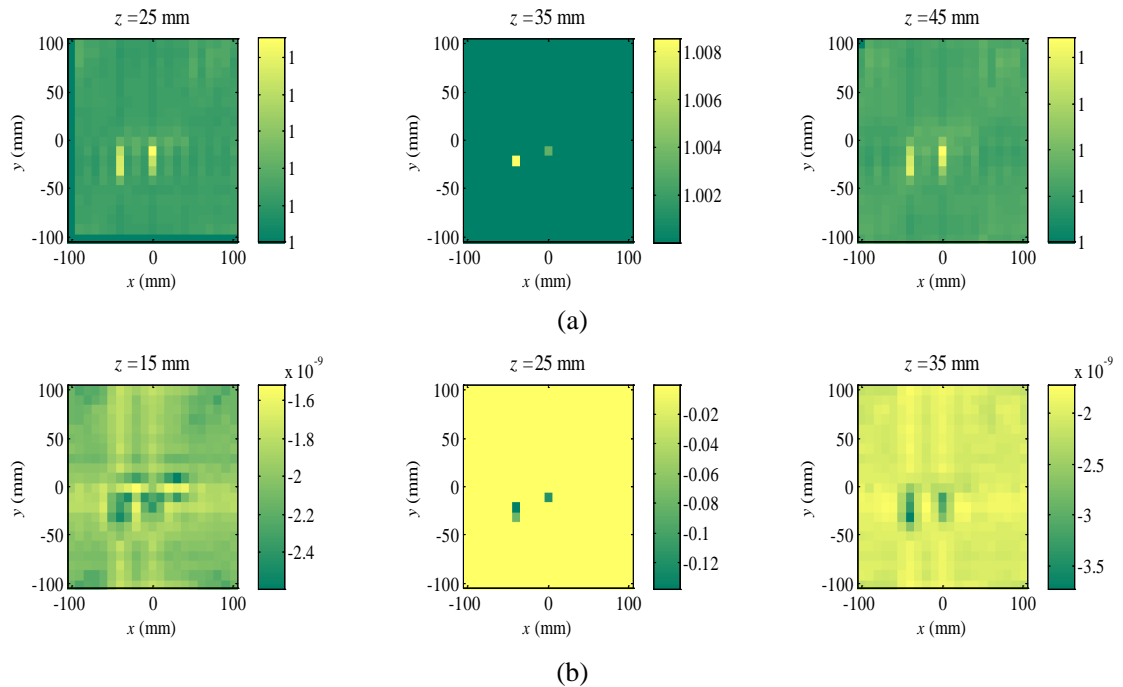


Figure 5.16 Quantitative holography with the CGSI method permittivity $1.2-j0$ and CO with permittivity $9-j0$: (a) the real part of the permittivity distribution, (b) the imaginary part of the permittivity distribution.

As can be seen in Figure 5.16, the addition of constraints worsens the results since the F-shape is no longer visible.

Table 5.4 Comparison of the PSI methods and the CGSI method in the example with CO of permittivity 9-j0 and an F-shaped target of permittivity 1.2-j0.

	PSI Method $\frac{\Gamma_{\text{OUT}}(\mathbf{r})}{\Gamma_{\text{CO}}} \approx 1$	PSI Method $\frac{\Gamma_{\text{OUT}}(\mathbf{r})}{\Gamma_{\text{CO}}} \neq 1$	CGSI Method
rRMSE	0.024161	0.018424	0.097743
Runtime (in seconds)	2.862	2.41	428.975

The F-shape does not appear in any of the quantitative or the qualitative results. The unconstrained case where $\Gamma_{\text{OUT}}(\mathbf{r})/\Gamma_{\text{CO}} \neq 1$ and the constrained method appear to have the same rRMSE. Interestingly, the CGSI method provides the worst results for the rRMSE and runtime.

5.3 Conclusions

This chapter demonstrated the impact of the permittivity of the CO and the permittivity of the OUT on the quantitative results. It also showed that in many cases the results between the CGSI and the PSI methods are comparable in terms of accuracy. However, in some cases there are drastic differences, like the case where the permittivity of the F-shape was 1.2-j0 and the CO had a permittivity of 9-j0. The difference in computational

cost is enormous, with the PSI methods being on the order of 2×10^2 times faster than the CGSI method.

The accuracy of the PSI method is entirely dependent on whether or not the GF is included. This is particularly interesting for the cases where the PSI method with $\Gamma_{\text{OUT}}(\mathbf{r})/\Gamma_{\text{CO}} \neq 1$ outperformed the PSI method with $\Gamma_{\text{OUT}}(\mathbf{r})/\Gamma_{\text{CO}} \approx 1$ even for the cases where $\varepsilon_{\text{OUT}}(\mathbf{r}) \approx \varepsilon_{\text{CO}}$. We conclude that the GF should not be approximated to be one in the PSI method. It improves the accuracy while at the same time it does not increase the computational burden.

We should keep in mind that in practice, the OUT's permittivity distribution is unknown. This makes it difficult to predict the accuracy of the CGSI method since it relies on a relation that assumes that the permittivities of the CO and the OUT are relatively close. This is especially important for iterative solvers, where a proper initial guess could be the difference between obtaining the optimal solution or an incorrect one.

References

- [1] F. Li, Q.H. Liu, and Lin-Ping Song, "Three-dimensional reconstruction of objects buried in layered media using Born and distorted Born iterative methods," *IEEE Geosci. and Remote Sensing Lett.*, vol. 1, no. 2, April 2004.
- [2] T.M. Habashy, R.W. Groom, and B.R. Spies, "Beyond the Born and Rytov approximations: a nonlinear approach to electromagnetic scattering," *J. Geophys. Res.*, vol. 98, no. B2, pp. 1759-1775, Feb. 1993.

- [3] M.S. Zhdanov and S. Fang, "Quasi-linear approximation in 3D EM modelling," *Geophysics*, vol. 61, no. 5, pp. 646-665, Jun. 1996.
- [4] M.S. Zhdanov and S. Fang, "3D quasi-linear EM inversion," *Radio Sci.*, vol. 31, no. 4, pp. 741-754, Jul. 1996.
- [5] M.S. Zhdanov and S. Fang, "3D EM electromagnetic inversion based on quasi-analytical approximation," *Inverse Problems*, vol. 16, no. 5, pp. 1297-1322, Oct. 2000.

Chapter 6

Conclusions and Future Work

6.1 Concluding Thoughts

This thesis has shown three methods to realize the quantitative microwave holographic reconstruction in the near zone.

First, the constrained global spectral inversion (CGSI) method was developed that uses the real and imaginary permittivity values in real space as constraints. This method solves a large system of equations simultaneously to reconstruct the permittivity distribution of the target.

The other two methods use a pointwise spectral inversion (PSI) method, which is capable of incorporating the quasi-analytic (QA) approximation of the total field inside the region of interest (ROI) through the gamma factor (GF) [1]–[4]. The QA approximation was shown to improve the imaged quality in our examples.

After exploring several arrangements with different permittivity distributions, it is clear that the benefits that the GF brings to the PSI method are substantial. Therefore, it should always be included in the PSI method.

The CGSI method occasionally obtains the most accurate results. The drawback of this method is that it is very slow and in many cases the improvement is marginal.

Another potential downfall of the CGSI method is the fact that it is based on the assumption that the permittivity of the calibration object (CO) is close to the permittivity of the object under test (OUT). In practical settings, the OUT's permittivity distribution is unknown.

It should be noted that since the contrast weighting factor $\tau(\mathbf{r})$ is a function of position, the voxels where no scatterers are present were generally reconstructed well for the CGSI method, which could attribute to the reason for the lower relative root-mean squared error (rRMSE).

6.2 Future Work

Direct methods have their limitations. The proposed quantitative reconstruction techniques are direct and are, thus, unable to handle the impact of mutual coupling. This becomes a hurdle when we have large permittivity contrasts and arrangements with scatterers close to other scatterers. As such, the intended purpose of the proposed method is to be used to generate an initial guess for an iterative solver [5].

So far, the quantitative inversion has been tested in simulations only for targets that have contrast in the real part of the permittivity. Further tests are required for targets and calibration objects that also exhibit contrast in the imaginary part of the permittivity (i.e., contrast in conductivity).

The quantitative algorithm needs to be extended to the case of dispersive media where the complex permittivity is a function of the frequency.

The method also needs to be tested in an experimental setting to analyze the impact of noise and other environmental influences.

In addition, since the PSI methods have been employed in Fourier space, it is crucial to determine if constraints in Fourier space can be applied. As seen in the CGSI method, the constraints improve the image reconstruction of the background medium, which is equally important as reconstructing the target.

The MATLAB code for the CGSI method needs to be optimized such that it takes advantage of the Fourier shift property to expedite the generation of the qualitative maps for the CO.

Finally, alternative solvers for the solution of the arising linear systems of equations must be investigated. In particular, minimizing the ℓ_1 norm of the solution error may prove advantageous in preserving the shape edges and converging to a better solution.

References

- [1] T.M. Habashy, R.W. Groom, and B.R. Spies, "Beyond the Born and Rytov approximations: a nonlinear approach to electromagnetic scattering," *J. Geophys. Res.*, vol. 98, no. B2, pp. 1759-1775, Feb. 1993.
- [2] M.S. Zhdanov and S Fang, "Quasi-linear approximation in 3D EM modelling," *Geophysics*, vol. 61, no. 5, pp. 646-665, Jun. 1996.
- [3] M.S. Zhdanov and S Fang, "3D EM quasi-linear EM inversion," *Radio Sci.*, vol. 31, no. 4, pp. 741-754, Jul. 1996.

- [4] M.S. Zhdanov and S Fang, "3D EM electromagnetic inversion based on quasi-analytical approximation," *Inverse Problems*, vol. 16, no. 5, pp. 1297-1322, Oct. 2000.
- [5] F. Li, Q.H. Liu, and Lin-Ping Song, "Three-dimensional reconstruction of objects buried in layered media using Born and distorted Born iterative methods," *IEEE Geosci. and Remote Sensing Lett.*, vol. 1, no. 2, April 2004.

Bibliography

R.K. Amineh, M. Ravan, A. Khalatpour, and N.K. Nikolova, "Three-dimensional near-field microwave holography using reflected and transmitted signals," *IEEE Trans. Antennas Propag.*, vol. 59, no. 12, pp. 4777-4789, Dec. 2012.

R.K. Amineh, A. Khalatpour, H. Xu, Y. Baskharoun, and N.K. Nikolova, "Three-dimensional near-field microwave holography for tissue imaging," *Int. J. Biomed. Imag.*, vol. 2012, Art. 291494 (11 pp.) , Dec. 2012.

R.K. Amineh, J. McCombe, and N.K. Nikolova, "Microwave holographic imaging using the antenna phaseless radiation pattern," *IEEE Antennas Wireless Propag. Lett.*, vol. 12, pp. 1529-1532, Dec. 2012.

R.K. Amineh, M. Ravan, J. McCombe, and N.K. Nikolova. "Three-dimensional microwave holographic imaging employing forward-scattered waves only," *Int. J. of Antennas and Propag.*, vol. 2013, Article ID 897287 (15 pp.), April 2013.

R.K. Amineh, J. McCombe, A. Khalatpour, and N.K. Nikolova, "Microwave holography using point-spread functions measured with calibration objects," *IEEE Trans. Instrum. & Meas.*, vol. 64, no. 2, pp. 403-417, Feb. 2015.

C. Balanis, *Advanced Engineering Electromagnetics*, 2nd ed., Hoboken, NJ: John Wiley and Sons, 2012.

M. Bakr, *Nonlinear Optimization in Electrical Engineering with Applications in MATLAB*, IET, 2013.

W. Chew 1995 *Waves and Fields in Inhomogeneous Media* Piscataway, NJ: IEEE Press.

CVX Research, Stanford, California: 2012, <http://www.cvxr.com>.

EM Software & System, Inc. USA, www.feko.info.

C.H. Edwards and D.E. Penney, *Calculus Early Transcendentals*, 7th ed., 2008.

N.H. Farhat and W.R. Guard, "Millimeter wave holographic imaging of concealed weapons," *Proc. IEEE*, vol. 59, no. 9, pp. 1383-1384, Sept. 1971.

D. Gabor, "A new microscope principle," *Nature*, vol. 161, no. 4098, pp. 777-778, May 1948.

T.M. Habashy, R.W. Groom, and B.R. Spies, 1993, "Beyond the Born and Rytov approximations: a nonlinear approach to electromagnetic scattering," *J. Geophys. Res.* vol. 98, no. B2, pp. 1759-1775, Feb. 1993.

W.F. Hirschfeld, "The invention of radar meteorology," *Bulletin Amer. Meteorological Soc.*, vol. 67, no. 1, pp. 33-37, Jan. 1986.

J.H. Jacobi, L.E. Larsen, and C.T. Hast, "Water-immersed microwave antennas and their application to microwave interrogation of biological targets," *IEEE Trans. Microwave Theory Tech.*, vol. MTT-27, no. 1, pp. 70-78, Jan. 1979.

S.K. Jericho, P. Klages, J. Nadeau, E.M. Dumas, M.H. Jericho, and H.J. Kreuzer, "In-line digital holographic microscopy for terrestrial and exobiological research," *Planetary and Space Sci.*, vol. 58, no. 4, pp. 701-705, Mar. 2010.

M. Jericho, H.J. Kreuzer, M. Kanka, and R. Riesenber, "Quantitative phase and refractive index measurements with point-source digital in-line holographic microscopy," *Appl. Optics*, vol. 51, no. 10, pp. 1503-1515, Mar. 2012.

M. Klemm, D. Gibbins, J. Leendertz, T. Horseman, A.W. Preece, R. Benjamin, and I.J. Craddock, "Development and testing of a 60-element UWB conformal array for breast cancer imaging," in *Proc. 5th European Conf. on Antennas and Propag. (EuCAP)*, Rome, Italy, 2011, pp. 3077-3079.

F. Li, Q.H. Liu, and Lin-Ping Song, "Three-dimensional reconstruction of objects buried in layered media using Born and distorted Born iterative methods," *IEEE Geosci. and Remote Sensing Lett.*, vol. 1, no. 2, pp. 107-111, April 2004.

L. Liu, A. Trehan, and N.K. Nikolova, "Near-field detection at microwave frequencies based on self-adjoint sensitivity analysis," *Inverse Problems*, vol. 26, 105001, 2010.

MATLAB, Natick, MA, USA, 2012, <http://www.mathworks.com/>.

J.J. McCombe "Noise reduction in microwave imaging and detection," M.A.Sc. Thesis, Dept. Elect. and Comp. Eng., McMaster Univ., 2014.

Mosek, Copenhagen, Denmark, 1997, <https://www.mosek.com>.

N.K. Nikolova, private communication.

A.V. Oppenheim and R.W. Schaffer, *Discrete-Time Signal Processing*, 2nd ed. Upper Saddle, NJ: Prentice Hall, 1999.

- N. Osumi, K. Ueno, "Microwave holographic imaging of underground objects," *IEEE Trans. Antenna Propag.*, vol. 33, no. 2, pp. 152-159, Feb. 1985.
- M. Peichl, H. Suss, S. Dill, M. Greiner, M. Jirousek, "Imaging technologies and applications of microwave radiometry," Conf. Proc. 1st European Radar Conf., Wessling, Germany, 2004, pp. 269-273.
- D. Pozar, *Microwave Engineering*, John Wiley & Sons, Inc., 2005.
- M. Ravan, R.K. Amineh, and N.K. Nikolova, "Two-dimensional near-field microwave holography," *Inverse Problems*, vol. 26, no. 5, 0555011 (21 pp.), May 2010.
- M.S. Salazar-Palma, T.K. Sarkar, L. Garica-Castillo, T. Roy, A. Djordjevic, *Iterative and Self-Adaptive Finite-Elements in Electromagnetic Modeling*, Norwood, MA: Artech House, Inc. 1998.
- D.M. Sheen, D.L McMakin, and T.E. Hall, "Near-field three-dimensional radar imaging techniques and applications," *Appl. Optics*, vol. 49, no. 19, pp. E83-E93, July 2010.
- D.M. Sheen, D.L McMackin, and T.E. Hall, "Three-dimensional millimeter-wave imaging for concealed weapon detection," *IEEE Trans. Microwav. Theory Tech.*, vol. 49, no. 9, pp. 1581-1592, Sept.2001.
- G.E. Smith, K. Woodbridge, C.J. Baker, and H. Griffiths, "Multistatic micro-Doppler radar signatures of personnel targets," *IET Signal Proc.*, vol. 4, no. 4, pp. 224-233, Jun. 2010.
- J.M. Thomas, C.J. Baker, and H.D. Griffiths, "HF passive bistatic radar potential and applications for remote sensing," *New Trends for Environmental Monitoring for Passive Syst.*, 2008, pp. 1-5, Oct. 2008.
- J.R. Thompson, J.J. McCombe, S. Tu, and N.K. Nikolova, "Quantitative imaging of dielectric objects based on holographic reconstruction," *Radar Conf. (RadarCon), 2015 IEEE*, pp. 0679-0683, 10-15 May 2015.
- G. Tricoles and N.H. Farhat, "Microwave holography: Applications and techniques," *Proc. IEEE*, vol. 65, no. 1, pp. 108-121, Jan. 1977.
- S. Tu, J.J. McCombe, D.S. Shumakov, and N.K. Nikolova, "Fast quantitative microwave imaging with resolvent kernel extracted from measurements," *Inverse Problems*, vol. 31, 045007 (33 pp.), Feb. 2015.

S. Tu, "Fast quantitative microwave imaging based on calibration measurements," Ph.D. Dissertation, Dept. Elect. and Comp. Eng., McMaster Univ., 2015.

M.S. Zhdanov and S Fang, "Quasi-linear approximation in 3D EM modelling," *Geophysics*, vol. 61, no. 5, pp. 646-665, Jun. 1996.

M.S. Zhdanov and S Fang, "3D quasi-linear EM inversion," *Radio Sci.*, vol. 31, no. 4, pp. 741-754, Jul. 1996.

M.S. Zhdanov and S Fang, "3D EM electromagnetic inversion based on quasi-analytical approximation," *Inverse Problems*, vol. 16, no. 5, pp. 1297-1322, Oct. 2000.